Department of Structural Engineering
Faculty of Engineering Science and Technology
NTNU- Norwegian University of Science and Technology

ACCESSIBILITY

OPEN

MASTER THESIS 2011

SUBJECT AREA:	DATE:	NO. OF PAGES:
Computational Mechanics	June 14, 2011	125

TITLE:

Assessment of the flutter stability limit of the Hålogaland Bridge using a probabilistic approach

Vurdering av flutter stabilitetsgrensen til Hålogalandsbroen med en probabilistisk metode

BY:

Tori Høyland Kvamstad

SUMMARY:
The present work is a study of the aeroelastic stability limit of the Hålogaland Bridge. The state-of-the-art theory concerning determination of flutter stability limits in modern bridge design is presented. The self-excited loads are modeled using aerodynamic derivatives obtained in a free vibration wind tunnel test of a section model.

The bimodal flutter limit of all relevant pairs of still-air vibration modes are evaluated, by considering the frequency separation and mode shape similarity of the respective modes. The findings of the bimodal analysis are used as a starting point in the assessment of the multimodal flutter limit. The governing flutter mechanism of the Hålogaland Bridge is three-mode flutter, where the fundamental symmetric torsion mode couple with the first and second symmetric vertical modes. The critical mean wind velocity is found to 68.1 m/s, which is above the design requirement of 60.2 m/s. The critical oscillation frequency is found to 2.03 rad/s. The total damping in the wind-structure system is evaluated.

Modeling uncertainty in the prediction of flutter limits is discussed. A proposed probabilistic flutter analysis utilizing Monte Carlo simulations is used to evaluate the effect of parameter uncertainty. The sensitivity with respect to parameter uncertainty of flutter derivatives and structural damping is assessed by considering the probability distribution of the flutter limit. Including uncertainties of the flutter derivatives due to different interpretation of scatter in the wind tunnel test series is found to have a significant influence on the flutter limit. Large scatter resulted in wide distributions. Choice of structural damping ratio is seen to have little influence. The distribution of critical flutter velocity may be modeled by an extreme value distribution, where a 99 % confidence interval ranges from 63.5 m/s to 78.6 m/s. The results indicate that the proposed probabilistic flutter analysis provides extended information concerning the accuracy related to prediction of flutter limits.

RESPONSIBLE TEACHER: Anders Rønnquist

SUPERVISOR(S): Ole Andre Øiseth, Anders Rønnquist, Ragnar Sigbjörnsson, Allan Larsen (COWI)

CARRIED OUT AT: Department of Structural Engineering, NTNU

MASTEROPPGAVE 2011

for

Tori Kvamstad

Assessment of the flutter stability limit of the Hålogaland Bridge using a probabilistic approach

Vurdering av flutter stabilitetsgrensen til Hålogalandsbrua med en probabilistisk metode

One of the essential requirements of modern bridge design is to avoid excessive wind induced vibration. A long-span suspension bridge, the Hålogaland Bridge is currently under planning in the northern part of Norway. The main span is 1145m, and since the bridge will only have two traffic lanes and one lane for bicycles and pedestrians, the bridge will become very slender and susceptive to wind induced vibrations.

The student should study the state of the art theory concerning aeroelastic stability of cable supported bridges. The bimodal stability limits for all relevant mode combinations should be assessed and then the bimodal mode combination that provides the lowest stability limit should be used as starting point for a multimode assessment of the aeroelastic stability limit of the suspension bridge. The total damping of the aeroelastic system should be evaluated at varying mean wind velocities.

The student should study the sensitivity of the stability limit with respect to parameter uncertainty. The probability distribution of the flutter stability limit should be obtained taking into account the uncertainties of the flutter derivatives and the still-air damping of the structure.

The aerodynamic and structural properties of the bridge will be provided by COWI

The thesis should be organized according to current guidelines

Advisors: Ole Andre Øiseth, Anders Rønnquist, Ragnar Sigbjörnsson, Allan Larsen (COWI)

The thesis should be submitted to the Department of Structural Engineering not later than June 14, 2011

NTNU,   January 29, 2011

Anders Rönnquist
Supervisor

Preface

This report is prepared as a master thesis for the Department of Structural Engineering at the Norwegian University of Science and Technology (NTNU), the spring semester of 2011. The thesis consists of a work amount corresponding to 30 credits at NTNU.

I have always been impressed by the boundaries of suspension bridge engineering, yet my earlier experience with wind engineering dynamics is limited. In the project assignment (fall 2010) I worked with calculations of the buffeting response of the Hardanger Bridge in the frequency domain. This thesis takes a step further into field of aerodynamics, by entering the world of aeroelasticity of cable-supported bridges.

The problem statement of considering the multimodal flutter limit of the Hålogaland Bridge was initiated by Allan Larsen, at the consultant engineering company COWI. The assignment was developed further by Ole Øiseth at NTNU, to include considerations of the probabilistic nature of flutter.

I would like to thank my supervisor at NTNU, Ole Øiseth, for rewarding discussions and constructive feedback during the process. I would also like to thank my supervisor at COWI, Allan Larsen. His, and Sanne Poulin's, sharing of experience and knowledge have had a great value to my theoretical understanding. Advice and guidance throughout this work provided by the supervisors is highly appreciated.

Tori Kvamstad

Trondheim, June 14, 2011

Abstract

The present work is a study of the aeroelastic stability limit of the Hålogaland Bridge. The state-of-the-art theory concerning determination of flutter stability limits in modern bridge design is presented. The self-excited loads are modeled using aerodynamic derivatives obtained in a free vibration wind tunnel test of a section model.

The bimodal flutter limit of all relevant mode pairs are evaluated, by considering frequency separation and mode shape similarity of the respective modes. The findings of the bimodal analysis are used as a starting point in the assessment of the multimodal flutter limit. The governing flutter mechanism of the Hålogaland Bridge is three-mode flutter, where the fundamental symmetric torsion mode couple with the first and second symmetric vertical modes. The critical mean wind velocity is found to 68.1 m/s, which is above the design requirement of 60.2 m/s. The critical oscillation frequency is found to 2.03 rad/s. The development of the total damping in the system with respect to increasing mean wind velocity is evaluated. Horizontal mode influence is investigated by applying quasi-static theory and aerodynamic derivatives obtained in the discrete vortex shedding software DVMFLOW. The results indicate that horizontal modes do not have influence on the flutter limit.

Modeling uncertainty in the prediction of flutter limits is discussed. A proposed probabilistic flutter analysis utilizing Monte Carlo simulations is used to evaluate the effect of parameter uncertainty. The sensitivity with respect to parameter uncertainty of flutter derivatives and structural damping is assessed by considering the probability distribution of the flutter limit. Including uncertainties of the flutter derivatives due to different interpretation of scatter in the wind tunnel test series is found to have a significant influence on the flutter limit. Large scatter resulted in wide distributions. Choice of structural damping ratio is seen to have little influence. The distribution of critical flutter velocity may be modeled by an extreme value distribution, where a 99 % confidence interval ranges from 63.5 m/s to 78.6 m/s. The results indicate that the proposed probabilistic flutter analysis provides extended information concerning the accuracy in the prediction of flutter limits.

Contents

Chapter 1

Introduction

1.1 Background

The collapse of the original Tacoma Narrows Suspension Bridge in November 1940 is one of the most important incidents in bridge engineering. During a fall storm, the deck of the Tacoma Narrows Bridge was subjected to excessive twisting. The torsional oscillations grew in amplitude until the bridge finally collapsed into the sound. Designers and scientist at the time were astonished. How could a wind storm measuring a mean wind velocity of about 19 m/s cause such a failure?

The period around 1940 was dominated by the construction of bridges with increasing span lengths, slender to save material costs. Prior to its failure, the Tacoma Narrows Bridge was seen as a symbol of modern bridge design, having one of the longest span lengths at the time. Its fatal collapse fundamentally changed the course of suspension bridge engineering. The investigations to determine its cause is seen as the starting point of the study of aerodynamic effects of cable-supported bridges [17].

A photo of the Tacoma Narrows Bridge at the day of its collapse is shown in Figure 1.1. Today, the phenomenon of vibration amplitudes growing in time is known as flutter. At a critical mean wind velocity and critical oscillation frequency, flutter instability occurs due to the interaction of the the wind field and structural motion of a bridge. In recent years, progression in design tools and construction method has again lead to growing span lengths, pushing the boundaries of engineering practice. As a result, flutter stability is again a subject of extensive research.

In Norway, wide fjord-crossings have lead to the construction of several suspension bridges. The Hålogaland Bridge is currently under planning in the northern part of Norway. With a main span of 1145 m, it will join the list among the longest bridge spans in the world. The Hålogaland Bridge is located in a sparsely populated area, and will only have two traffic lanes and one lane for bicycles and pedestrians. The narrow deck combined with the long span will result in a very slender structure, compared to other bridges of its size. One

of the essential requirements in the design is to avoid excessive wind induced vibrations. Special attention must be given to aeroelastic stability.
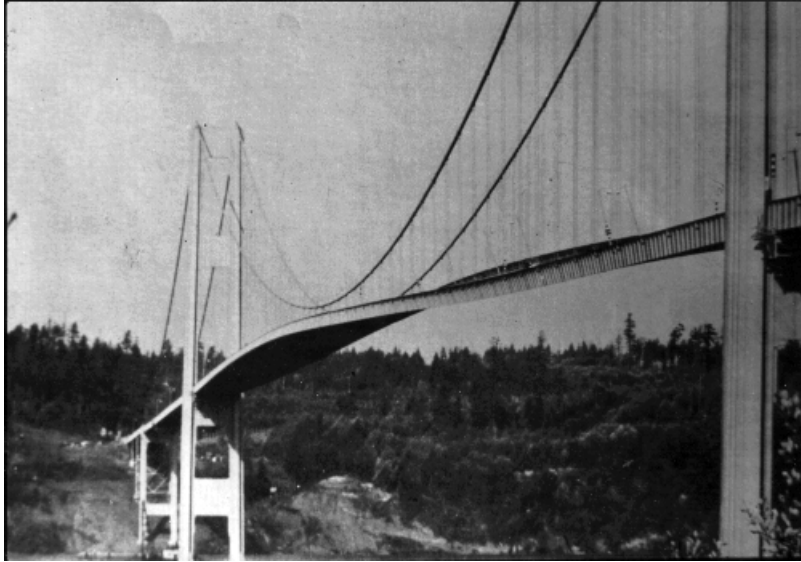

Figure 1.1: Torsional oscillations of the original Tacoma Narrows Suspension Bridge [17]

1.2 Objective of work

This paper presents the basic content of the aeroelastic theory related to wind-induced instability of suspension bridges. Focus is given to understanding the phenomena of coupled flutter and different methods of determining the critical flutter limit in modern bridge design. The present state-of-the-art method is the multimode flutter analysis, based on a combination of still-air structural properties and wind tunnel testing. The development of the load model and formulation of the flutter problem resulting in a critical mean wind velocity is presented. It is chosen to investigate the flutter stability limit of the Hålogaland Bridge as a case study.

The difference between a bimodal and multimodal approach to the stability limit is evaluated. Based on the structural system, is it possible to determine when a multimodal approach should be employed, and when a bimodal analysis is sufficient? The occurrence of multimode coupled flutter is assessed by evaluating the mode shape similarity in combination with the frequency separation of the still-air vibration modes. With reference to the new requirement set out in the bridge design manual of the Norwegian Public Road Administration (Handbook 185), the effect of horizontal modes on the critical wind speed is also discussed [26]. The total damping in the system is evaluated.

In worst case scenario, flutter can result in ultimate bridge failure, as shown by the collapse of the Tacoma Narrows Bridge. Hence, it is vital to ensure a

sufficient safety against flutter. Flutter limit analysis is in general based on deterministic analysis, where all parameters are assumed known. In reality, however, there are a number of uncertainties related to the prediction of flutter. These uncertainties are collected in a safety factor in the design requirement. This factor is specified as 1.6 in Handbook 185 [26]. How accurate is the estimated critical velocity? The flutter limit as a probabilistic variable is discussed.

The bridge designer must base the flutter estimation on a set of input parameters. Of these, many are a subject of interpretation of wind tunnel test results. The still-air damping ratio is an example of an unknown parameter that must be based on wind tunnel tests and past experience. Aerodynamic properties observed in the wind tunnel often provides measurements subjected to large scatter. How does the interpretation of the observed behavior affect the flutter limit? At which accuracy can the critical velocity be determined when the input parameters are subjected to scatter?

The sensitivity of the flutter limit with respect to parameter uncertainty is investigated by establishing a probabilistic method involving Monte Carlo simulations. By assuming normal distributed input parameters of flutter derivatives and still-air damping, the probability distribution of the critical mean wind velocity is obtained.

Chapter 2

Theory

2.1 Wind loads on bridges

Cable-supported bridges are flexible structures susceptive to wind-induced vibrations. The wind field is turbulent due to friction between the flow and the terrain. When a turbulent wind field meets a fixed obstacle, the instantaneous wind velocity pressure acting on the structure is given by Bernoulli's equation:

$$q(t) = \frac{1}{2}\rho \left[U(t)\right]^2 \tag{2.1}$$

where ρ is the air density and $U(t)$ represents the wind flow. The resulting forces acting on the structure may be divided into four parts: (1) static wind forces from the mean wind, (2) time-fluctuating buffeting forces ascribed to wind turbulence, (3) forces generated by vortices shed on the surface and into the wake of the body, (4) self-excited forces induced by the interaction of flow and motion of the body [28]. The focus in this project is on the self-excited forces. Self-excited forces occur due to the aeroelastic characteristics of slender, flexible bridges. Aeroelastic behavior arises when the structural deformation of the bridge induces changes in the aerodynamic forces from the wind field. The additional aerodynamic forces cause an increase in the deformation of the structure, which in terms leads to greater aerodynamic forces in a feedback process. In this way, the motion-induced forces are described as a self-excited phenomenon [7].

The induced structural motion and deformation changes the nature of the structural system. Hence the structural characteristics will depend on the wind field. It is common to distinguish between in-wind and still-air characteristics. This might be described as an introduction of aerodynamic damping and stiffness in the structural system [25].

2.1.1 Motion-induced instability

The flow-structure interaction is stabilizing or destabilizing depending on how the energy is transferred between structure and flow. An instability limit, de-

fined by a critical mean wind velocity V_{cr}, is a fictive limit where either the total damping or stiffness in the structural system is analytically equal to zero, as a reaction to the interaction between the wind field and the static and dynamic response of the structure. When the mean wind velocity increases towards such a limit, the bridge motion will be dominated by large displacements. These may lead to structural damage or, in worst case scenario, construction failure. Literature regarding different instability limits is given in Strømmen [28] and Simiu and Miyata [25]. It is common to distinguish between four such types of instability limits, classified by their nature and the response type of displacements that occurs. These are:

- Static divergence

- Galloping

- Torsional flutter

- Coupled flutter

Static divergence is an instability phenomenon that occurs due to negative aerodynamic stiffness contribution. When the negative modal aerodynamic torsional stiffness reaches the magnitude of the modal structural stiffness in still-air, the total torsional stiffness in the system is zero. The structure will then collapse due to excessive twisting, as the angle of incidence will increase without limit. Static divergence occurs at high wind velocities, at which an adequate safety margin must be secured.

Galloping refers to structural vibrations perpendicular to the oncoming flow. It is a single degree of freedom instability phenomenon caused by negative aerodynamic damping in the cross-wind direction. Galloping occurs for certain cross-sections where the slope of the lift coefficient C_L' is negative. The angle of incident of the relative velocity vector changes as the structure starts to move away from its equilibrium position. For certain cross-sections, this change in relative velocity vector creates asymmetric pressure distributions that enhance the initial motion, resulting in unstable behavior. Galloping typically occurs for square cross-sections.

Flutter refers to structural vibrations that include twisting motion. As for galloping, the main effect is that the interaction between flow and structure creates negative damping. The flutter phenomenon is however more complex in a sense that it involves effects due to vorticity. A special case of flutter is torsional flutter, a single degree of freedom instability that occurs if the torsional aerodynamic damping of a structure becomes negative. Torsional flutter may occur for rectangular cross-sections or H-shaped sections The latter was the configuration of the original Tacoma Narrows Bridge.

While galloping and torsional flutter may be avoided by choosing bridge decks with adequate aerodynamic performance, coupled flutter occurs for flexible bodies with flat in-plane shape, such as air foils and stream-lined box-sections. Coupled flutter is thus the governing type of aeroelastic instability for a great number of modern long span bridges. Of this reason, it is chosen to only focus on coupled flutter stability in this project. A detailed description of coupled

flutter is given in the section 2.2. Coupled flutter is also denoted as "Classical flutter" in literature. For simplicity, coupled flutter will be referred to as "flutter" in the following.

2.1.2 Self-excited wind loads

The forces acting on a bridge deck are divided into drag, lift and moment forces, denoted as q_y, q_z and q_θ, respectively. The definition of the axis system and forces are given in Figure 2.1, where the displacement components r_y, r_z and r_θ are positive in the same direction as the forces. The main source of aerodynamic excitation is assumed to occur due to bridge deck motion, and self-excited forces on other parts of the bridge are ignored [7].
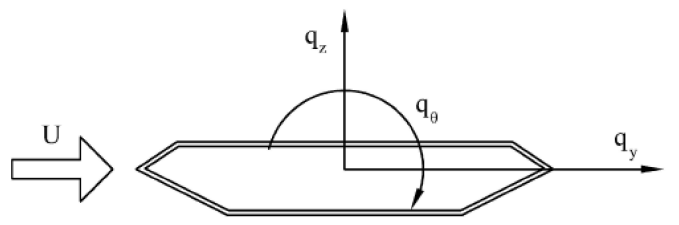

Figure 2.1: Definition of loads and dimensions [11]

The self-excited forces depend on the structural motion and flow in a complex way, and are for this reason impossible to describe analytically. The load model is instead based a combination of the equation of motion and empirical data, where the aerodynamic characteristics of a bridge structure are determined by wind tunnel testing. The load model describes the self-excited forces as linearized functions of the structural response, i.e. the bridge deck motion. The link between structural response and associated forces is expressed in terms of non-dimensional coefficients known as aerodynamic derivatives. The theoretical expressions of the self-excited forces has its origin in the airfoil theory applied in aeronautics, and was first transferred to bridge applications by R.H Scanlan in the 70s, see Scanlan and Tomko [23]. The original formulation was based on bending and twisting motion only, but was later extended to include lateral motion, as given in Eq. 2.2.

$$q_y^{se} = \tfrac{1}{2}\rho V^2 B \left(KP_1^* \tfrac{\dot{r}_y}{V} + KP_2^* \tfrac{B\dot{r}_\theta}{V} + KP_3^* r_\theta + K^2 P_4^* \tfrac{r_y}{B} + KP_5^* \tfrac{\dot{r}_z}{V} + K^2 P_6^* \tfrac{r_z}{B} \right)$$

$$q_z^{se} = \tfrac{1}{2}\rho V^2 B \left(KH_1^* \tfrac{\dot{r}_z}{V} + KH_2^* \tfrac{B\dot{r}_\theta}{V} + KH_3^* r_\theta + K^2 H_4^* \tfrac{r_z}{B} + KH_5^* \tfrac{\dot{r}_y}{V} + K^2 H_6^* \tfrac{r_y}{B} \right)$$

$$q_\theta^{se} = \tfrac{1}{2}\rho V^2 B^2 \left(KA_1^* \tfrac{\dot{r}_z}{V} + KA_2^* \tfrac{B\dot{r}_\theta}{V} + KA_3^* r_\theta + K^2 A_4^* \tfrac{r_z}{B} + KA_5^* \tfrac{\dot{r}_y}{V} + K^2 A_6^* \tfrac{r_y}{B} \right)$$

$$(2.2)$$

where V is the mean wind velocity, ρ is the air density, B is the width of the bridge deck girder and K is the non-dimensional reduced angular frequency

given by

$$K = \frac{\omega B}{V} \tag{2.3}$$

The coefficients P_i^*, H_i^* and A_i^* are the aerodynamic derivatives. It should be noted that the formulation given in Eq. 2.2 yields aerodynamic derivatives with twice the magnitude compared to the original Scanlan notation, which referred to the half-chord of the bridge ($B = B/2$). The original Scanlan sign convention had positive z-axis downwards. It is seen from Figure 2.1 that both the lift force q_z^{se} and vertical displacement component r_z are positive upwards, hence derivatives H_2^*, H_3^*, H_5^*, H_6^*, A_1^*, A_4^*, P_5^* and P_6^* will have opposite sign in the present formulation. The present notation is similar to the notation used in Dyrbye and Hansen [7].

2.1.3 Aerodynamic derivatives

There are in total 18 aerodynamic derivatives P_i^*, H_i^* and A_i^* from 3 load components combined with 3 deflections and 3 velocity terms. They can best be described as a representation of aerodynamic damping and aerodynamic stiffness provided by the interaction of wind field and structure. Reorganizing the self-excited forces in Eq. 2.2, the aerodynamic damping and stiffness matrices may be expressed as

$$
\begin{aligned}
\mathbf{C}_{ae} &= \frac{\rho B^2}{2} \omega \begin{bmatrix} P_1^* & P_5^* & BP_6^* \\ H_5^* & H_1^* & BH_2^* \\ BA_5^* & BA_1^* & B^2 A_2^* \end{bmatrix} \begin{Bmatrix} r_y \\ r_z \\ r_\theta \end{Bmatrix} \\
\mathbf{K}_{ae} &= \frac{\rho B^2}{2} \omega^2 \begin{bmatrix} P_4^* & P_6^* & BP_5^* \\ H_6^* & H_4^* & BH_3^* \\ BA_6^* & BA_4^* & B^2 A_3^* \end{bmatrix} \begin{Bmatrix} r_y \\ r_z \\ r_\theta \end{Bmatrix}
\end{aligned} \tag{2.4}
$$

By considering the aerodynamic matrices in Eq. 2.4, it is for example seen that H_1^* and A_2^* are related to aerodynamic damping of vertical and torsional motion, respectively. The characteristics of the aerodynamic derivatives determine the instability limits [7]. For this reason, they also commonly referred to as flutter derivatives.

The aerodynamic derivatives describe the fluctuating forces on a vibrating bridge deck, and are obtained from wind tunnel tests. Full-scale bridge models are complicated and expensive to build. The aerodynamic performance is instead measured by applying a scaled section model, reflecting the outer shape of the prototype bridge deck. The geometrical scaling of the model is determined by considering geometry, mass and stiffness of the prototype. Typical scales are in the order 1:50 and 1:100 [7]. The scaling of the wind velocity in the wind tunnel is given by

$$\left(\frac{n_\theta B}{V}\right)_{model} = \left(\frac{n_\theta B}{V}\right)_{prototype}$$

where n_θ is the torsional frequency in still-air, B is the deck width and V is the mean wind velocity. The bridge model is suspended in a dynamic test rig, reflecting the bridge vibration characteristics. The wind flow around the model should be similar to the wind around the prototype to obtain aeroelastic equivalent behavior. This is achieved by controlling that inertial forces are modelled in the same mutual ratio as in full-scale, by adjusting a number of non-dimensional scale parameters. In general there are three methods of determining aerodynamic derivatives (ADs) from wind tunnel tests [7]:

1. Free vibration tests. The section model is given an initial displacement, activating a vertical or torsion mode. Measurement and evaluation of the transient behavior of the released bridge deck model is used to identify the aerodynamic behavior.

2. Forced vibration tests. The section model is forced into a certain motion, where aerodynamic behavior is evaluated by placing pressure taps on the cross section surface. Subtracting the forces at zero motion will render the net motion-induced effect.

3. Buffeting vibration tests. The section model is subjected to a turbulent wind field. The ADs are extracted from the buffeting response data, by applying system identification techniques.

It should be noted that the first method traditionally only provides the 8 aerodynamic derivatives related to vertical and torsional motion. As it is difficult and expensive to simulate horizontal along wind motion in wind tunnels, the aerodynamic derivatives associated with the horizontal modes are often disregarded.The measured aerodynamic derivatives will depend on the structural properties of the scaled model, and vary with the applied mean wind velocity. For this reason the aerodynamic derivatives are extracted as functions of a non-dimensional reduced velocity

$$\hat{V} = \frac{1}{K} = \frac{V}{B\omega}$$

Analytical expression of the aerodynamic derivatives of an ideal flat plate is developed, see e.g. the description given in Strømmen [28]. Obviously, the flat plate aerodynamic derivatives are not directly applicable for real life bluff sections. Nevertheless, they serve as an important comparison for the measured derivatives [7]. In recent years, development within computational fluid dynamic (CFD) models has provided new methods of determining aerodynamic behavior.

2.2   Flutter

Flutter is an aeroelastic phenomenon that involves a positive feedback of forces due to flow-structure interaction. The flutter limit is defined as the limit where the energy input from the motion induced wind load is equal to the energy dissipated by structural damping. For wind velocities above this limit, the structure is unstable; a small perturbation may lead to excessive amplitude growth and violent vibrations.

Unlike single degree of freedom torsional flutter, which arises due to negative aerodynamic damping in torsion, coupled flutter may occur even if the aerodynamic damping of torsion and vertical motion is positive (i.e. $H_1^* > 0$, $A_2^* > 0$). It occurs due to aerodynamic interaction of two or more vibration modes, in general the lowest torsion mode in combination with one or more vertical modes [7].

The self-excited forces changes the characteristics of the bridge response as the wind speed increases, and tend to increase vertical bending stiffness and reduce torsional stiffness in the wind-structure system. Due to overturning moment induced by twisting of the bridge deck, the torsional frequency is reduced, resulting in a reduced frequency separation between the torsional frequency ω_θ and the vertical frequency ω_z. Flutter arises when the vertical and torsional motion couple at a frequency ω between ω_θ and ω_z, where the degrees of freedom couple together in flow-driven unstable oscillations. The vertical and torsional vibrations occur together with a phase difference, transferring energy between the two motions and the air flow. There are in general three methods available to determine the flutter limit of a cable bridge [7]:

- Numerical analysis of wind-structure system with flutter derivatives from wind tunnel tests

- Experimental determination by direct measurement in a wind tunnel

- Empirical formulas

The flutter limit is predicted numerically by considering the dynamic equilibrium condition of the still-air structural properties combined with the self-excited forces given in Eq. 2.2. Assuming harmonic damped oscillating motion on the form $e^{(a+ib)t}$, a complex eigenvalue analysis of the coupled wind-structure system may be performed. The resulting eigenvalues and eigenvector contains the in-wind characteristics of the system. An eigenvalue analysis of $n = 1...N$ still-air vibration modes result in $2N$ eigenvalues S_k and corresponding eigenvectors $\mathbf{Z}_k$. The nature of the roots of the characteristic equation reveals the physics of the solution [12]. It is distinguished between

- Real roots

- Complex roots

If the roots are real and positive, this implies a system with exponential divergence. Real and negative roots imply exponential convergence. However, in general, the roots will be complex, resulting in system behavior of oscillatory nature. In addition to a magnitude, a phase is included. These roots come in complex conjugate pairs on the form

$$S_k = a_n + ib_n, \;\; S_{k+1} = a_n - ib_n \tag{2.5}$$

where i is the complex number and $k = 1...2N$. The interpretation of the eigenvalues is easily illustrated by considering the initial assumption of damped harmonic motion on the form

$$e^{St} = e^{(a \pm ib)t} = e^{at}e^{\pm ibt} = e^{at}\left(\cos\left(bt\right) \pm i\sin\left(bt\right)\right) \tag{2.6}$$

The interpretation of Eq. 2.6 is illustrated in Figure 2.2. The harmonic motion may be represented by the complex circle where $\pm b$ is the phase angle and e^{at} is the radius. The oscillating nature is described by the phase, and thus b is a measure of the damped natural frequency of the aeroelastic system. If a is positive, the radius of the circle will increase resulting in a spiral extending outwards, describing divergent oscillations. A negative value of a will decrease the oscillations. Hence, the real part of the eigenvalue describes damping in the system. The limit between divergent and decaying behavior is defined by $a = 0$. The self-excited forces in the eigenvalue analysis are given as functions of the non-dimensional reduced frequency K. The critical flutter velocity is found for the value K of ω where the solution is purely imaginary, i.e. at the limit between divergent and decaying oscillations. Thus, the stability limit is defined as the lowest mean wind velocity resulting in zero damping in one of the in-wind modes.
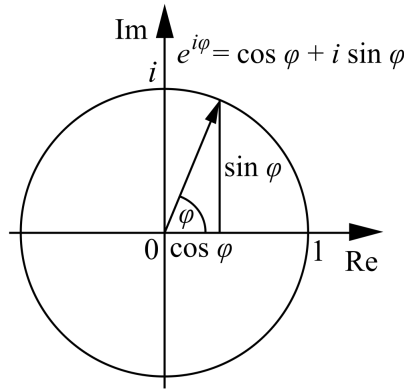

Figure 2.2: Harmonic oscillations

This procedure was first described for a two degree of freedom system by R.H. Scanlan, see Scanlan and Tomko [23]. It was further developed to a bimodal eigenvalue analysis of two fundamental pair of modes; the first symmetric vertical mode and the first torsion mode. The development of the bimodal flutter equations are described in Section 2.2.1. The theory presented are based on the description of bimodal flutter given in Dyrbye and Hansen [7] and Simiu and Miyata [25].

Other modes may also participate in bridge flutter. In particular the second and third symmetric vertical modes may contribute to the development of instability. These modes will often have eigenfrequencies close to the torsional mode, and are thus likely to couple. In addition, horizontal modes were found to contribute to modal coupling for the Akashi-Kaikyo Bridge [15]. The present state-of-the-art method to determine the flutter stability limit is the multimultimodal approach, where aerodynamic coupling among several modes of bridge deck motion is investigated. The generalized flutter equations including multimodal coupling are described in Section 2.2.2. Theory regarding multimodal flutter is found in

the articles presented by Katsuchi et al. [15], Jakobsen and Hjort-Hansen [13] and Øiseth and Sigbjörnsson [12].

Experimental determination of flutter limit in wind tunnel was the governing procedure up to recent years. This procedure is shortly outlined in Section 2.2.3. In addition, some empirical closed-form approximations to the flutter limit are given in Section 2.2.4.

2.2.1 Formulation of the bimodal flutter problem

Flutter instability is in general dominated by a fundamental pair of vertical and torsional modes, with additional contributions from others. The starting point of the flutter analysis is a bimodal assessment, where the two modes are assumed restricted to pure vertical and pure torsional degrees of freedom respectively. This is a valid assumption due to geometric configuration of suspension bridges [7]. If the self-excited forces that arise from horizontal motion are neglected, the total number of flutter derivatives reduces to 8. The self-excited forces are then given by

$$q_z^{se} = \frac{1}{2}\rho V^2 B \left(K H_1^* \frac{\dot{r}_z}{V} + K H_2^* \frac{\dot{r}_\theta}{V} + K^2 H_3^* r_\theta + K^2 H_4^* \frac{r_z}{B} \right)$$

$$q_\theta^{se} = \frac{1}{2}\rho V^2 B^2 \left(K A_1^* \frac{\dot{r}_z}{V} + K A_2^* \frac{\dot{r}_\theta}{V} + K^2 A_3^* r_\theta + K^2 A_4^* \frac{r_z}{B} \right) \qquad (2.7)$$

When deriving the flutter equations it is convenient to apply a modal frequency domain approach. The structural displacement components are represented by generalized degrees of freedom as products of a time invariant mode shape $\phi_n(x)$ and modal coordinate $\eta_n(t)$ as

$$r_z = \phi_z(x)\eta_z(t)$$

$$r_\theta = \phi_\theta(x)\eta_\theta(t) \qquad (2.8)$$

where x is the coordinate along the bridge span. Hence, the full-scale bridge motion is represented by two generalized degrees of freedom. The modal equation of motion of these two degrees of freedom in time domain are given by

$$\tilde{M}_z \ddot{\eta}_z(t) + \tilde{C}_z \dot{\eta}_z(t) + \tilde{K}_z \eta_z(t) = \tilde{Q}_z^{se}$$

$$\tilde{M}_\theta \ddot{\eta}_\theta(t) + \tilde{C}_\theta \dot{\eta}_\theta(t) + \tilde{K}_\theta \eta_\theta(t) = \tilde{Q}_\theta^{se} \qquad (2.9)$$

where $\tilde{M}_n$ represents the modal mass, $\tilde{C}_n$ is modal damping, $\tilde{K}_n$ is modal stiffness, and Q_n^{se} the modal load given by

$$\begin{aligned} \tilde{M}_n &= \int_L \phi_n(x) m_n(x) dx \\ \tilde{C}_n &= \tilde{M}_n 2\zeta_n \omega_n \\ \tilde{K}_n &= \tilde{M}_n \omega_n^2 \\ \tilde{Q}_n^{se} &= \int_{L_{exp}} \phi_n(x) q_n^{se} dx \end{aligned} \qquad (2.10)$$

12

respectively, where ω_n is the natural frequency and ζ_n the damping ratio of still-air mode n where $n \, \epsilon \, \{z, \theta\}$. L is the length of the structure, L_{exp} is the flow exposed part of the structure, $m_z(x)$ is the distributed mass and $m_\theta(x)$ is the cross-sectional mass moment of inertia. Further, the solution to the equation of motion is assumed harmonic on the form $\eta_n(t) = G_n(\omega)e^{(a+bi)t}$, where $G_n(\omega)$ is the Fourier amplitude of mode n and $i = \sqrt{-1}$ represents the imaginary unit. Taking the Fourier transform of the equation of motion will result in the equation of motion in frequency domain. By combining the equation of motion and the aerodynamic forces on one side of the equality sign the equation system represents a complex eigenvalue problem.

$$\left[\tilde{m}_z \left(-\omega + 2\zeta_z\omega_z i\omega + \omega_z^2 \right) - \tfrac{1}{2}\rho V^2 B \left(\tfrac{K}{V} H_1^* i\omega + \tfrac{K^2}{B} H_4^* \right) C_{zz} \right] G_z(\omega)$$
$$- \left[\tfrac{1}{2}\rho V^2 B C_{z\theta} \left(\tfrac{KB}{V} H_2^* i\omega + K^2 H_3^* \right) \right] G_\theta(\omega) = 0$$

$$\left[\tilde{m}_\theta \left(-\omega + 2\zeta_\theta\omega_\theta i\omega + \omega_\theta^2 \right) - \tfrac{1}{2}\rho V^2 B^2 C_{\theta\theta} \left(\tfrac{KB}{V} A_2^* i\omega + K^2 A_3^* \right) \right] G_\theta(\omega)$$
$$- \left[\tfrac{1}{2}\rho V^2 B^2 C_{\theta z} \left(\tfrac{K}{V} A_1^* i\omega + \tfrac{K^2}{B} A_4^* \right) \right] G_z(\omega) = 0$$

$$(2.11)$$

Here, $\tilde{m}_n$ is the equivalent modal mass given by Eq. 2.12 and C_{ij} are non-dimensional coefficients representing the shapewise similarity of the modeshapes, given by Eq. 2.13 .

$$\tilde{m}_n = \frac{\tilde{M}_n}{\int_{L_{exp}} \phi_n^2 dx} \tag{2.12}$$

$$C_{ij} = \frac{\int_{Lexp} \phi_i(x)\phi_j(x)dx}{\int_{Lexp} \phi_i^2(x)dx} \tag{2.13}$$

The stability limit of the aeroelastic system is found by demanding the determinant of the coefficient matrix in Eq. 2.11 equal to zero. The eigenvalue problem depends on both ω and V in a complicated way. By subdividing with the vertical frequency, terms containing frequency may be represented by $X = \omega/\omega_z$ and the frequency ratio $\gamma = \omega_\theta/\omega_z$ between the vertical and torsional frequency. In addition the follwing coefficients are introduced to simplify the expressions.

$$\chi_z = \frac{\tilde{m}_z}{\rho B^2} \quad \chi_\theta = \frac{\rho B^4}{\tilde{m}_\theta} \tag{2.14}$$

The resulting characteristic equation of the determinant of the equations in Eq. 2.11 may be written as a function of X. The forth order characteristic equation will have both real and imaginary terms, connected to structural displacement and velocity, respectively. Separating the real and imaginary parts gives the two characteristic equations of the system

$$\begin{aligned} RX^4 + R_3X^3 + R_2X^2 + R_0 &= 0 \\ I_3X^3 + I_2X^2 + I_1X + I_0 &= 0 \end{aligned} \tag{2.15}$$

If it assumed that $L \simeq L_{exp}$, the mode shape coefficients given in C_{ij} attains unity when $i = j$ and the coefficients of the real and imaginary parts are given by

$$R_4 = 1 + \frac{1}{2\chi_\theta}A_3^* + \frac{1}{2\chi_z}H_4^* + \frac{1}{4\chi_\theta\chi_z}\left(-H_1^*A_2^* + H_4^*A_3^* - \psi_{z\theta}H_3^*A_4^* + \psi_{z\theta}H_2^*A_1^*\right)$$

$$R_3 = \frac{1}{\chi_z}\zeta_\theta\gamma H_1^* + \frac{1}{\chi_\theta}\zeta_z A_2^*$$

$$R_2 = -\gamma^2 - 4\zeta_\theta\zeta_z\gamma - 1 - \frac{1}{2\chi_\theta}A_3^* - \frac{1}{2\chi_z}\gamma^2 H_4^*$$

$$R_0 = \gamma^2$$

$$I_3 = \frac{1}{2\chi_\theta}A_2^* + \frac{1}{2\chi_z}H_1^* + \frac{1}{4\chi_\theta\chi_z}\left(H_4^*A_1^* + H_2^*A_4^* - \psi_{z\theta}H_3^*A_1^* - \psi_{z\theta}H_2^*A_4^*\right)$$

$$I_2 = -\frac{1}{\chi_z}\zeta_\theta\gamma H_4^* - \frac{1}{\chi_\theta}\zeta_z A_3^* - 2\zeta_z - 2\zeta_\theta\gamma$$

$$I_1 = -\frac{1}{2\chi_\theta}A_2^* - \frac{1}{2\chi_z}\gamma^2 H_1^*$$

$$I_0 = 2\zeta_\theta\gamma + 2\zeta_z\gamma^2$$

$$(2.16)$$

where the mode shape similarity coefficient $\psi_{z\theta}$ is introduced as $\psi_{z\theta} = C_{zz}C_{\theta\theta}$. Modal coupling depends on the magnitude $\psi_{z\theta}$ given in Eq. 2.17. Modes are not likely to couple if the value of $\psi_{z\theta}$ is close to zero, i.e. an asymmetrical vertical mode does not couple with a symmetric torsion mode. If the modes are shapewise dissimilar, the off-diagonal contribution will become zero, which implies that coupled flutter will not occur.

$$\psi_{z\theta} = \frac{\int_L \phi_z(x)\phi_\theta(x)dx}{\int_L \phi_z^2(x)dx}\frac{\int_L \phi_z(x)\phi_\theta(x)dx}{\int_L \phi_\theta^2(x)dx} \qquad (2.17)$$

The solution of the characteristic equations in Eq. 2.15 is found for the root $X_{cr} = \omega_{cr}/\omega_z$ where both the real and imaginary equation is zero. The complex eigenvalue problem represents a two dimensional problem, as in addition to X the flutter derivatives depend on the reduced velocity $\hat{V} = V/\omega B$. The solution is found by plotting curves corresponding to the roots of the real and imaginary characteristic equations in Eq. 2.15 as a function of the reduced velocity $\hat{V}$. This procedure is commonly known as the Theodorsen method. see e.g. Fung [9]. A forth order real equation result in 4 roots and the third order imaginary equation in 3 roots. To sort out the solution corresponding to the flutter limit, an initial guess may be evaluated from solving the characteristic equations with zero structural damping. The real and imaginary characteristic equation then reduces to

$$\begin{aligned} r_4X^4 + r_2X^2 + r_0 &= 0 \\ i_3X^3 + i_1X &= 0 \end{aligned} \qquad (2.18)$$

where the equation coefficients corresponds to the coefficients in Eq. 2.16 by setting $\zeta_z = \zeta_\theta = 0$. Choosing the roots of Eq. 2.15 closest to the initial guesses from Eq. 2.18, the flutter limit may be determined graphically as illustrated in Figure 2.3.
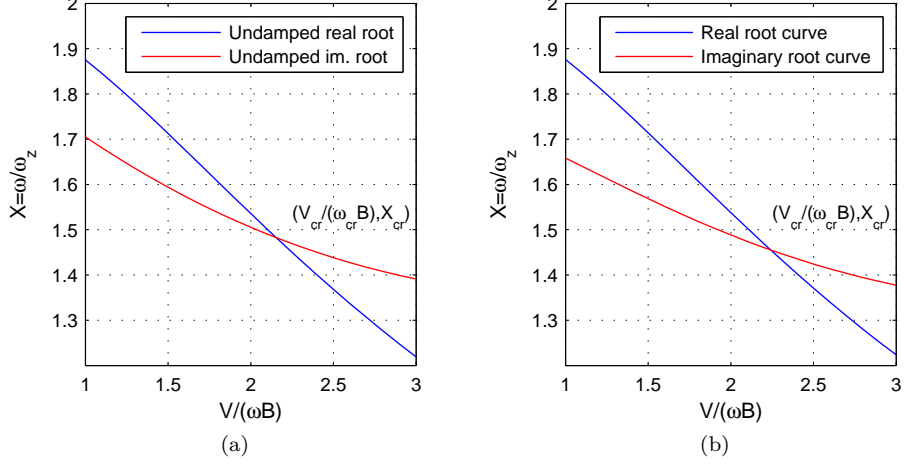
Figure 2.3: Determination of critical flutter from intersection of root curves where structural damping of still-air modes is a) excluded b) included

The intersection point $((V_{cr}/\omega_{cr}B), X)$ of the curves corresponds to the root where both the imaginary and real part of the equation is zero, and defines the reduced critical flutter velocity and reduced critical frequency. The critical frequency and critical mean wind velocity defining flutter is then given by

$$
\begin{aligned}
\omega_{cr} &= \omega_z X \\
V_{cr} &= \hat{V}_{cr} \omega_{cr} B
\end{aligned}
$$

Solving the flutter problem with zero structural damping predicts the actual flutter limit with reasonable accuracy as structural damping in general is low. In the example shown in Figure 2.3, the undamped and damped root curves are seen to provide nearly the same intersection point.

2.2.2 Formulation of the multimodal flutter problem

Investigations of several suspension bridges indicates that multimode flutter is the governing instability, see e.g. Katsuchi et al. [15]. It is widely recognized that coupled flutter where several vibration modes interact may occur. The additional modes may be stabilizing or destabilizing, depending on their generation of coupling forces. Nevertheless, a multimodal approach more accurately predicts the flutter limit, as an increased number of vibration modes better represent the actual bridge motion.

A multimodal flutter problem including N still-air vibration modes will result in coefficient matrices of $N \times N$ dimension. It is convenient to write system parameters in matrix notation, as the terms in the flutter equations are severely expanded due to the complicated coupling between the modes. The bridge motion represented by generalized degrees of freedom is given by

$$\boldsymbol{r}(x,t) = \boldsymbol{\Phi}(x)\boldsymbol{\eta}(t)$$

where $\boldsymbol{r}(x,t)$ represents the displacement and rotation vector along the span given by the mode shape matrix $\boldsymbol{\Phi}(x)$ and the generalized degrees of freedom vector $\boldsymbol{\eta}(t)$. Each of the still-air vibration modes $\boldsymbol{\phi}_n(x)$ in $\boldsymbol{\Phi}(x)$ are given by three component $\phi_y(x)$, $\phi_z(x)$ and $\phi_\theta(x)$, describing the horizontal, vertical and torsional component of the mode shape, respectively. The components of the bridge motion are given by

$$
\begin{aligned}
\boldsymbol{r} &= \begin{bmatrix} r_y & r_z & r_\theta \end{bmatrix}^T \\
\boldsymbol{\Phi} &= \begin{bmatrix} \boldsymbol{\phi}_1 & ... & \boldsymbol{\phi}_n & ... & \boldsymbol{\phi}_N \end{bmatrix} \\
\boldsymbol{\eta} &= \begin{bmatrix} \eta_1 & ..... & \eta_n & ..... & \eta_N \end{bmatrix} \\
\boldsymbol{\phi}_n &= \begin{bmatrix} \phi_y & \phi_z & \phi_\theta \end{bmatrix}^T
\end{aligned}
$$

where $n = 1...N$. The multimode wind-structure eigenvalue problem is developed analogous to the bimodal case, by considering the modal equation of motion and motion dependent forces. All other loads are assumed to zero. By expanding the determinant on the left hand side, the stability limit of the aeroelastic system where N still-air vibration modes are included can be predicted by considering the following quadratic eigenvalue problem.

$$\left(S_k^2\tilde{\mathbf{M}}_0 + S_k\left(\tilde{\mathbf{C}}_0 - \tilde{\mathbf{C}}_{ae}\left(V,\omega\right)\right) + \left(\tilde{\mathbf{K}}_0 - \tilde{\mathbf{K}}_{ae}\left(V,\omega\right)\right)\right)\boldsymbol{Z}_k = 0 \qquad (2.19)$$

where S_k are the eigenvalues with corresponding eigenvectors $\boldsymbol{Z}_k$ and index $k = 1, 2, \ldots, 2N$. $\tilde{\mathbf{M}}_0$ represents the modal mass matrix, $\tilde{\mathbf{C}}_0$ is the modal damping matrix and $\tilde{\mathbf{K}}_0$ is the modal stiffness matrix, where index 0 refers to still-air structural parameters. The function matrix $\tilde{\mathbf{C}}_{ae}\left(V,\omega\right)$ and $\tilde{\mathbf{K}}_{ae}\left(V,\omega\right)$ represent the self-excited forces proportional to structural velocity and displacement respectively. The still-air structural properties of the bridge should be obtained by using expected mean load conditions, to properly represent the geometric stiffness. The mass matrix containing the cross-sectional mass properties is given by

$$\mathbf{M}_0 = \begin{bmatrix} m_y(x) & & \\ & m_z(x) & \\ & & m_\theta(x) \end{bmatrix} \qquad (2.20)$$

where $m_y(x)$ and $m_z(x)$ represents distributed mass and $m_\theta(x)$ is the mass moment of inertia of the cross-section. Further, the modal mass of mode n is defined as

$$\tilde{M}_{0,n} = \int_L \boldsymbol{\phi}_n^T \boldsymbol{M}_0 \boldsymbol{\phi}_n dx \qquad (2.21)$$

where $n = 1...N$. The modal mass may also conveniently be extracted directly from the FE model, by the lumped mass model in the free-vibration analysis.

When the modal mass of mode n is established, the still-air system matrices of dimension $N \times N$ are given by

$$
\begin{array}{rcl}
\tilde{\mathbf{M}}_0 & = & diag\left(\tilde{M}_{0,n}\right) \\
\tilde{\mathbf{K}}_0 & = & diag\left(\omega_{0,n}^2 \tilde{M}_{0,n}\right) \\
\tilde{\mathbf{C}}_0 & = & diag\left(2\zeta_{0,n}\omega_{0,n}\tilde{M}_{0,n}\right)
\end{array}
\tag{2.22}
$$

Where $\omega_{0,n}$ is eigenfrequency and $\zeta_{0,n}$ corresponding damping ratio associated with still-air vibration mode n. The matrices are diagonal due to the orthogonality of the mode shapes. The term $diag$ in Eq. 2.22 denotes diagonal matrix. Obviously, the in-wind modal matrices $\tilde{\mathbf{C}}_{ae}(V,\omega)$ and $\tilde{\mathbf{K}}_{ae}(V,\omega)$ are not diagonal, as it is the off-diagonal terms that generate flow-induced coupling. The $N \times N$ in-wind matrices are given by

$$
\tilde{\mathbf{C}}_{ae} = \begin{bmatrix} \ddots & & \\ & \tilde{C}_{ae,ij} & \\ & & \ddots \end{bmatrix}
$$

$$
\tilde{\mathbf{K}}_{ae} = \begin{bmatrix} \ddots & & \\ & \tilde{K}_{ae,ij} & \\ & & \ddots \end{bmatrix}
\tag{2.23}
$$

Where the element on row i and column j are given by

$$
\begin{array}{rcl}
\tilde{C}_{ae,ij} & = & \displaystyle\int_L \boldsymbol{\phi}_i^T \mathbf{C}_{ae} \boldsymbol{\phi}_j dx \\
\tilde{K}_{ae,ij} & = & \displaystyle\int_L \boldsymbol{\phi}_i^T \mathbf{K}_{ae} \boldsymbol{\phi}_j dx
\end{array}
\tag{2.24}
$$

Where $\boldsymbol{C}_{ae}$ and $\boldsymbol{K}_{ae}$ are the 3×3 motion dependent cross-sectional load coefficient matrices given by

$$
\begin{array}{rcl}
\mathbf{C}_{ae} & = & \dfrac{\rho B^2}{2}\omega \begin{bmatrix} P_1^* & P_5^* & BP_6^* \\ H_5^* & H_1^* & BH_2^* \\ BA_5^* & BA_1^* & B^2 A_2^* \end{bmatrix} \\[20pt]
\mathbf{K}_{ae} & = & \dfrac{\rho B^2}{2}\omega^2 \begin{bmatrix} P_4^* & P_6^* & BP_5^* \\ H_6^* & H_4^* & BH_3^* \\ BA_6^* & BA_4^* & B^2 A_3^* \end{bmatrix}
\end{array}
\tag{2.25}
$$

In the bimodal analysis, modal coupling is represented by a single factor, given by $\psi_{z\theta}$ in Eq. 2.17. This factor corresponds to the product of two mode shape integrals. The more complex modal coupling in the multimodal problem is

illustrated by considering the expanded term of $\tilde{K}_{ae,ij}$ of Eq. 2.24. As each mode shape is assumed to have three components, the fully expanded vector format is a scalar sum of 9 products as

$$
\begin{aligned}
\tilde{K}_{ae,ij} \quad = \quad & \frac{\rho B^2}{2}\omega^2 \int_L (P_4^* \phi_{y,i}^T \phi_{y,j}^T + H_6^* \phi_{z,i}^T \phi_{y,j}^T + BA_6^* \phi_{\theta,i}^T \phi_{y,j}^T + P_6^* \phi_{y,i}^T \phi_{z,j}^T \\
& + H_4^* \phi_{z,i}^T \phi_{\theta,j}^T + BA_4^* \phi_{\theta,i}^T \phi_{\theta,j}^T + BP_5^* \phi_{y,i}^T \phi_{\theta,j}^T + BH_3^* \phi_{z,i}^T \phi_{\theta,j}^T \\
& + B^2 A_4^* \phi_{\theta,i}^T \phi_{\theta,j}^T)dx
\end{aligned}
$$

Once the system matrices are established, the solution of the eigenvalue problem may be evaluated. The eigenvalues problem has to be solved by an iterative procedure as the functions $\mathbf{C}_{ae}$ and $\mathbf{K}_{ae}$ depend on the flutter derivatives which are functions of both frequency of motion and wind velocity. A schematic description of a possible calculation routine is suggested in the process diagram in Figure 2.4.

As seen in Figure 2.4, the multimode flutter calculation consists of two iteration loops, in terms iterating on the velocity and the frequencies. The calculation starts by establishing the still-air system modal matrices $\tilde{\mathbf{M}}_0$, $\tilde{\mathbf{C}}_0$ and $\tilde{\mathbf{K}}_0$, for the considered still-air vibration modes $n = 1...N$. Secondly, the in-wind system at mean wind velocity V is considered. An initial guess for the target in-wind frequency of mode n is given by the corresponding still-air frequency, by $\omega_{guess,n} = \omega_{0,n}$. Based on this, the in-wind matrices are established and the complex eigenvalue problem is solved. The eigenvalue solutions of mode n, a_n and b_n, represents the in-wind damping and in-wind eigenfrequency, respectively. Since the unsteady aerodynamic derivatives are functions of reduced velocity, the solution associated to each mode needs an iterative calculation until the assumed frequency $\omega_{guess,n}$ coincides with that of the target mode. Hence, if the frequency solution b_n of mode n differs from the initial guess $\omega_{guess,n}$, the eigenvalue analysis is repeated. The solution b_n is used as a guess for the target frequency in the next frequency iteration by setting $\omega_{guess,n} = b_n$.

This procedure is repeated until the in-wind frequency $b_n(V)$ is constant. The corresponding in-wind damping $a_n(V)$ is found, and the solutions are plotted against the considered velocity step V. Further, the next still-air vibration frequency is chosen as an initial guess for the second in-wind frequency, by starting the next iteration at $\omega_{0,n+1}$, until all in-wind modes are evaluated at velocity step V. The procedure is then repeated at the next velocity step $V = V + dV$. Flutter is reached when the real part of the solution, $a_n(V)$ of one of the in-wind modes becomes negative. The stability limit is determined graphically by the intersection point of the corresponding in-wind damping curve and the x-axis. It should however be noted that the flow chart presented in Figure 2.4 represents an unstable system, as the code presented does not necessarily converge towards a solution. Flutter does not occur for all wind-structure systems.

The solution of the multimodal eigenvalue problem for a system of three still-air vibration modes is shown in Figure 2.5. The circles mark the in-wind solutions for each of the three frequency branches at velocity step V. Note that as the eigenvalues come in complex conjugate pairs, each frequency branch will have
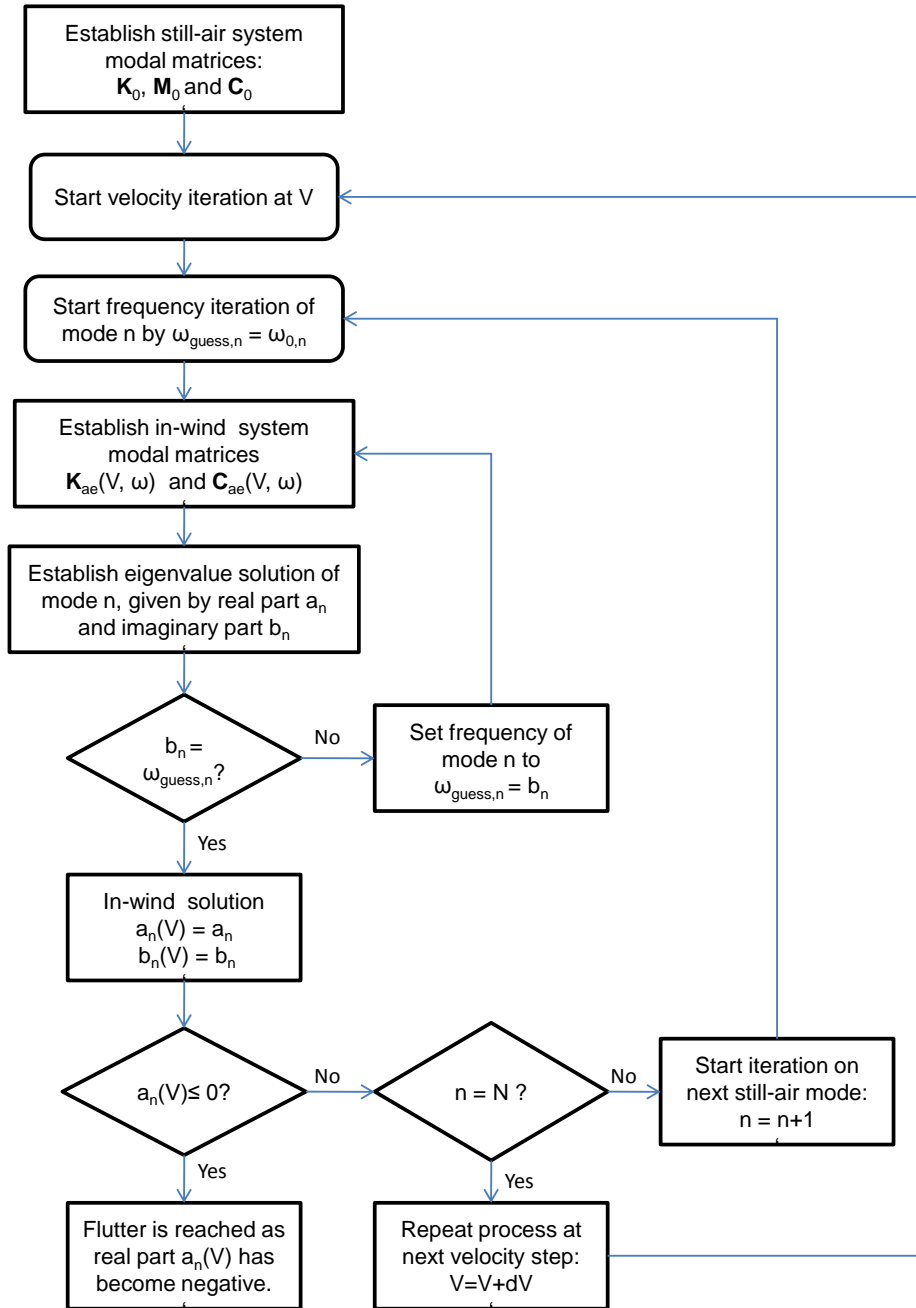
Figure 2.4: Float chart illustrating a possible implementation of the multimodal flutter equation. The critical mean wind velocity is determined at the intersection point of the imaginary root curve and the x-axis. Note that the system is unstable, as flutter does not necessarily occur..

two curves, one positive and one negative, that mirrors each other. This is indicated in the plot of the imaginary solution in Figure 2.5.
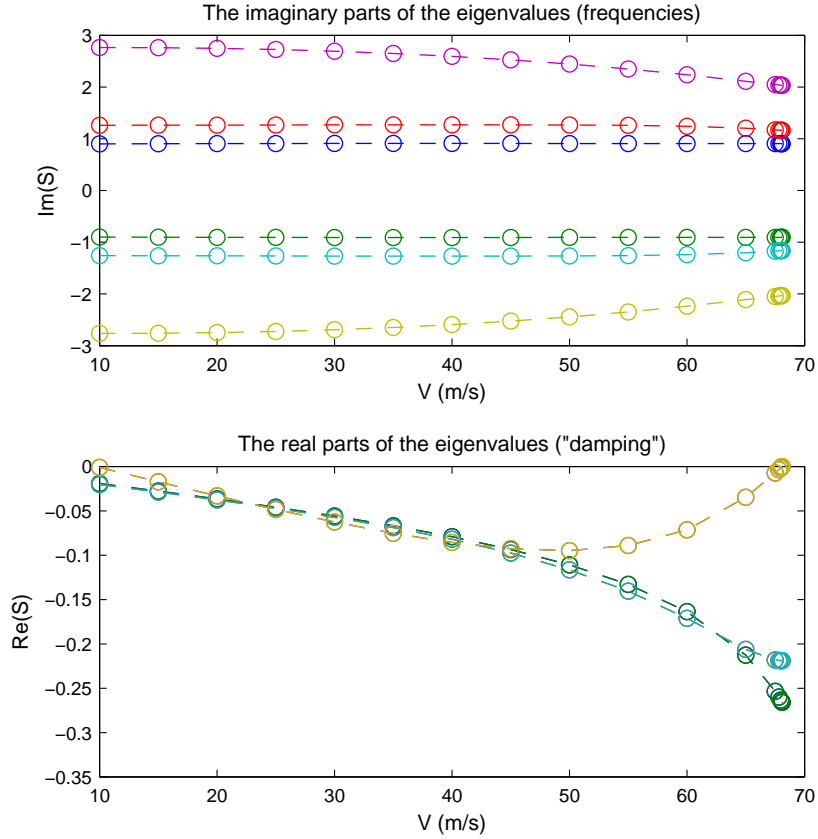

Figure 2.5: Multimodal graphical solution

An additional step-wise iteration should be included in the flow chart in Figure 2.4 to determine the numerical value of the mean wind velocity V at the intersection point. This is indicated in Figure 2.5, where the velocity increments dV is reduced when approaching the stability limit.

In-wind frequency and damping ratio

The roots of the multimode complex eigenvalue problem in Eq. 2.19 are given on the form $S_k = a_n + ib_n$, where the real part a and imaginary part b of the root are indacted as a measure of damping and frequency respectively. The direct physical interpretation of the real and imaginary part of the root is found by comparing with the solution of a 1DOF system as given in Eq. 2.26. If the solution is assumed on the form $x(t) = ze^{\lambda t}$, the characteristic equation of the

system is

$$\ddot{x}(t) + 2\zeta\omega\dot{x}(t) + \omega^2 x(t) = 0$$
$$\lambda^2 + 2\zeta\omega\lambda + \omega^2 = 0 \tag{2.26}$$

where λ is the eigenvalue and ζ and ω is the damping ratio and natural frequency of the 1DOF system. This will result in two eigenvalues which may either be complex or real, on the form

$$\lambda_1 = -\zeta\omega + i\omega\sqrt{1-\zeta^2}$$
$$\lambda_2 = -\zeta\omega - i\omega\sqrt{1-\zeta^2} \tag{2.27}$$

where i is the imaginary number. Comparing Eq. 2.27 with the general solution, $S_k = a_n + ib_n$ and $S_{k+1} = a_n - ib_n$, the coefficient a_n and b_n of mode n may be identified. If a complex eigenvalue analysis of N still-air vibration modes is considered, the coefficients of the conjugate pair of the solution of mode n is given by

$$a_n = -\zeta_n\omega_n$$
$$b_n = \omega_n\sqrt{1-\zeta_n^2} \tag{2.28}$$

where ζ_n and ω_n is the in-wind damping ratio and in-wind "undamped" frequency of mode n respectively. Reorganizing the expressions in 2.28, it is seen that ζ_n and ω_n may be expressed as functions of the real and negative part of the eigenvalue of mode n by

$$\omega_n = \sqrt{a_n^2 + b_n^2}$$
$$\zeta_n = \frac{-a_k}{\sqrt{a_n^2 + b_n^2}} \tag{2.29}$$

Knowing the coefficient a_n and b_n of mode n for each reduced velocity, the change of in-wind eigenfrequency and damping ratio may be plotted as a function of increasing mean wind velocity. The development of the in-wind characteristics describe the nature of the system. By considering the curve of the torsional in-wind damping, the instability is characterized as hard-type or soft-type flutter. Hard-type flutter refers to flutter where the torsional curve drop rapidly close to the flutter limit, corresponding to a sudden change around flutter onset. Soft-type flutter is characterized by a smooth torsional curve, decreasing slowly towards zero damping and instability.

Flutter mode shapes

Flutter occurs when one of the in-wind modes has zero damping. The in-wind vibration modes will fold down to one distinctive flutter mode, as all other in-wind modes are damped out during free vibration. The unstable bridge motion will thus be dominated by a single distinct motion, represented by the flutter mode shape [11].

The absolute critical flutter vibration amplitude increases towards infinite. However, the ratio between the degrees of freedom, and the phase angle between vertical and torsional deflection are described by the flutter eigenvectors, the flutter mode shapes. As for the eigenvalues, the flutter mode shapes also appear in complex conjugate pairs.

The still-air vibration modes are obtained by assuming an undamped system, in a free vibration analysis. The resulting mode shape vectors are real and indicate the relative position between the masses at any given instant of time at a specific frequency. The damped eigenvalue problem results in complex mode shapes, containing a phase lag. In addition to displacement, the mode shapes describe a velocity term. The relative position of the masses may be out of phase, meaning that the position of its poles will change in time. The magnitude of the phase is decided by the complex part of the mode shape. However, the time dependency is in many cases not dominating, hence the displacement at the poles gives a good indication of the appearance of the flutter vibrations. The flutter mode shape may be visualized by calculating the free vibration response of the whole system. A multimode flutter mode shape are in general found to have a simpler vibration form, compared with a bimodal flutter mode shape. This is because a larger part of the bridge deck moves, providing a lower curvature [11].

The focus in this thesis is on establishing the flutter limit with respect to the critical mean wind velocity and critical oscillation frequency. The flutter mode shapes are not considered further in the following flutter analysis of the Hålogaland Bridge. The flutter mode shapes can however be expected to be similar to those of the Hardanger Bridge, presented in e.g. Øiseth et al. [11]..

Effect of lateral flutter derivatives

In the recent years, multimodal flutter analysis has been widely recognized. It is however still common practice to base the multimodal analysis on two degree of freedom experimental flutter derivatives by the eight coefficients H_i^* and A_i^* where $i = 1..4$. This is supported by the assumption that aerodynamic derivatives related to horizontal motion will have stabilizing effect on flutter; it is conservative to exclude them in the flutter calculation [7].

In connection to the new requirement in Handbook 185, it is stated that effect of lateral modes is to be included in the multimode flutter analysis [26]. It may be assumed that this demand is based on the results of the Akashi-Kaikyo Bridge in Japan, where inclusion of horizontal modes were found to have a destabilizing effect. Coupling of the six fundamental modes, including the first and second symmetric horizontal modes, gave the lowest stability limit. Hence, lateral flutter derivatives played a significant and destabilizing role [15].

Measurement of the self-excited lateral loads simulated in the wind tunnel will to a great extent be interfered by buffeting response. Due to difficulties of identification in the wind tunnel tests, the lateral aerodynamic derivatives are in general omitted. Instead, a common approach has been to describe these by employing quasi-static theory. The quasi-static coefficients corresponding to the aerodynamic derivatives are given as

$$
\begin{bmatrix}
P_1^* & H_1^* & A_1^* \\
P_2^* & H_2^* & A_2^* \\
P_3^* & H_3^* & A_3^* \\
P_4^* & H_4^* & A_4^* \\
P_5^* & H_5^* & A_5^* \\
P_6^* & H_6^* & A_6^*
\end{bmatrix}
=
\begin{bmatrix}
-2C_D\frac{H}{B}\hat{V} & -(C_L' + C_D\frac{H}{B})\hat{V} & -C_M'\hat{V} \\
0 & 0 & 0 \\
C_D'\frac{H}{B}\hat{V}^2 & C_L'\hat{V}^2 & C_M'\hat{V}^2 \\
0 & 0 & 0 \\
(C_L - C_D'\frac{H}{B})\hat{V} & -2C_L\hat{V} & -2C_M\hat{V} \\
0 & 0 & 0
\end{bmatrix}
$$
$$(2.30)$$

where C_D, C_L, C_M is the quasi-static drag, lift and moment load coefficients, C'_D, C'_L and C'_M are the corresponding coefficient describing the rate of change by angle of attack, H is the height of the cross-section girder and $\hat{V} = V/B\omega$ is the reduced velocity. The quasi-static load coefficients describe forces acting on a static body with a certain angle of incident to the wind field. They do not take into account interaction of structural motion and wind flow, and several of the terms are zero. It is however argued that the quasi-static theory is a reasonable approximation for horizontal load components as the horizontal motion is relatively slow compared to the along wind speed component. Quasi-static derivatives where applied in the multimodal flutter calculations of the Akashi Bridge [15].

Nevertheless, whether horizontal modes should be included or not is a question that should be addressed. Each mode will to some extent include movement in all directions. One could imagine that a horizontal mode with a small rotation component could generate coupling forces and contribute to the unstable motion in flutter. In the case where the bridge deck has an inclination of +3 degrees, this coupling effect could increase. The 3D flutter analysis should be given focus, as including more modes better represents the actual bridge behavior.

2.2.3 Experimental determination of the flutter limit

Experimental determination of the flutter limit where the critical mean wind velocity is found by observing the oscillation pattern of a scaled model is widely practiced. This was the most trusted method after the Tacoma Narrows incident [7]. The test is often performed in the same dynamic test rig as used to determine the aerodynamic derivatives. In general, the section model rig is tuned to reproduce the fundamental pair of vertical and torsional modes.

The flutter limit is determined by gradually increasing the mean wind velocity in the wind tunnel until self-excited motion is observed. The occurrence of instability is recognized when the nature of the response changes from a random type of motion to a more narrow-banded sinusoidal motion. The highest wind speed where the test model is stable defines the critical wind speed [7].

Instability tests on a section model will never reflect the precise behavior of the actual bridge. In contrast to the prototype bridge, the reproduced vertical and torsional modes of the stiff section model will have constant and identical mode shapes. The actual flutter limit must thus be assumed to be higher, as shape-wise dissimilar modes will limit the coupling effects. More accurate aeroelastic behavior may be simulated by applying full-scale bridge models. A full-scale

model is typically able to reproduce the two first torsion frequencies and 4-5 vertical modes and thus better represent the actual bridge motion. However, these models are complicated and expensive to build. In addition, section models are often preferred due to the size limitation in wind tunnels.

2.2.4 Closed-form approximations to the flutter limit

Although great progress has been made in the field of flutter limit predictions in the recent years, the analytical closed-form approximations are still widely used. Due to their simplicity, they are especially important in preliminary design of long-span bridges. Selberg's formula is widely applied and referred to in several design codes, among others in Handbook 185 [26]. Alternative closed-form approaches which include effects of mode shape similarity and measured aerodynamic derivatives are presented in literature, see e.g. the formula presented in Øiseth and Sigbjörnsson [12]. Empirical formulas are useful tools as they lead to improved understanding of the nature of flutter. Studying closed-form solutions can easily reveal the control parameters that influence the inter-modal coupling and aerodynamic damping. The simplified approaches to the flutter limit are in general based on two fundamental still-air modes. They are not recommended in cases where the frequencies are closely spaced on the frequency axis, due to the possibility of multimodal effects.

Selberg's formula

The closed-form flutter limit formula developed by Arne Selberg in the 1960s describes the aerodynamic interaction of two shape-wise identical still-air modes, see Selberg [24]. It is based on Theodorsens air foil theory, assuming bridge decks with aerodynamic properties similar to those of an ideal flat plate. By the notation given in Section 2.2.1, Selberg's formula is given by

$$V = 3.7 B n_\theta \sqrt{\frac{m_z R_g}{\rho B^3} \left[1 - \left(\frac{n_z}{n_\theta} \right)^2 \right]} \tag{2.31}$$

where R_g is the radius of gyration given by $R_g = \sqrt{m_\theta/m_z}$. The Selberg formula gives a conservative approximation to the flutter limit of the first torsional and first vertical mode. As can bee seen in Eq. 2.31, the outcome of the formula is to a great extent dominated by the magnitude of the torsional eigenfrequency and the frequency ratio. For this reason, the Selberg formula does not give correct approximations for other mode pairs than the fundamental. The Selberg formula is considered a conservative approach to the flutter limit if the deck aerodynamics are like those of a flat plate, as mode shape dissimilarity in general will lead to higher critical wind speed [13].

Chapter 3

Case Study: The Hålogaland Bridge

A long-span suspension bridge, the Hålogaland Bridge, is currently being planned in the northern part of Norway. With a main span of 1145 meters, the Hålogaland Bridge will be the second longest suspension bridge in Norway, only surpassed by the Hardanger Bridge of 1310 meters. As both the Hardanger and Hålogaland Bridge is constructed in sparsely populated areas, narrow decks make these bridges extremely slender compared to others of their kind. This implies that wind-induced vibrations are a major concern in the design.

An adequate safety against flutter failure of the Hålogaland Bridge must be secured. The 10-min design mean wind velocity V_{ref} at the construction site is 37.6 m/s. This corresponds to the characteristic extreme wind velocity with a return period of 500 years. According to Handbook 185, the safety requirement with respect to the critical mean wind velocity is $V_{cr} \geq 1.6V_{ref}$ [26]. This yields a design wind velocity of 60.2 m/s.

All structural, modal and aerodynamic properties of the Hålogaland Bridge are provided by COWI.

3.1 Main geometry

The Hålogaland Bridge is to be included in the new high-way route E6 Narvik-Bjervik crossing Rombaksfjorden in the northern part of Norway. By connecting Karistranda and Øyjord, the travel distance Narvik-Bjervik is shortened with 17 km, see Figure 3.1. At the construction site, Rombaksfjorden has depth of about 350 meters. The fjord is approximately 1350 meters wide. In the preliminary design in early 2007 the bridge was intended to span the whole width. However, in a revised design in late 2007 the towers were instead founded on the sea bed, reducing the main span to 1145 meters. The main cables are anchored in solid rock on both shores.
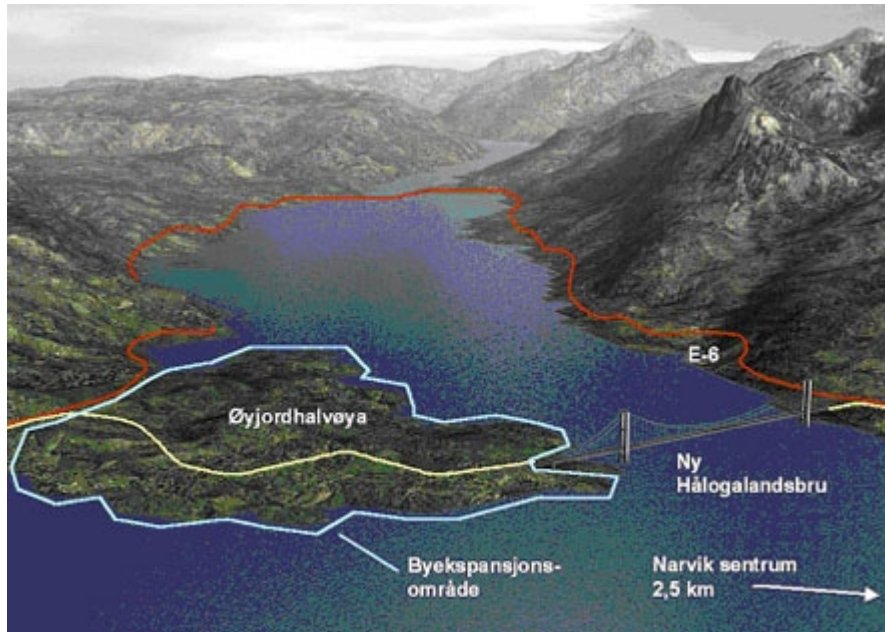
Figure 3.1: General map [27]

The main elevation of the Hålogaland Bridge is shown in Figure 3.2. The clearance under the girder is 40 meters and the towers have a height of about 180 meters above sea level. A-shaped pylons and inclined cable-planes were chosen due to their slender aesthetic appearance and good aerodynamic performance. The steel main girder carries two traffic lanes, and one bicycle lane. The towers and side spans are constructed in concrete.
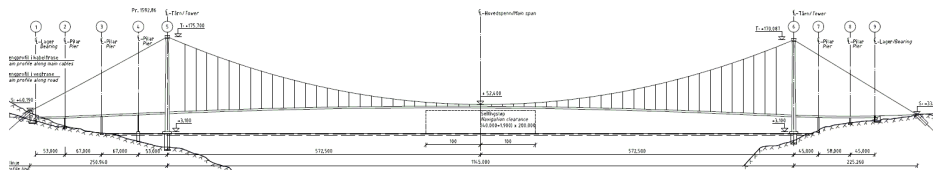

Figure 3.2: Main elevation of the Hålogaland Bridge

The bridge cross-section is shown in Figure 3.3. The bridge is designed with a wedged-shaped box girder with a width of 18.6 meters. The distance between the cable planes are 15.2 meters. Good aerodynamic design of the bridge deck is vital for the in-wind performance. The stream-lined shape was optimized to attain optimal aeroelastic behavior and eliminate vibration response due to vortex shedding.
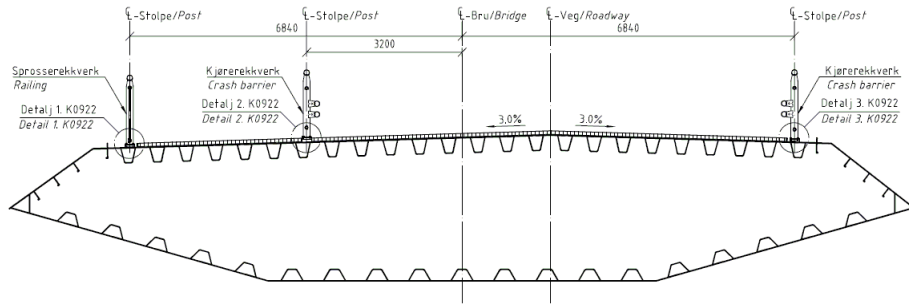
26

Figure 3.3: Cross-section of the Hålogaland Bridge

3.2 Modal analysis

The free vibration modal analysis is performed in IBDAS, COWI's in-house FE program. The FE model included bridge decks, towers, cables and hanger cables. The finite element model and coordinate system is shown in Figure 3.4. It should be noted that IBDAS applies a left hand coordinate system, with rotations defined in opposite direction of the more custom right hand systems.
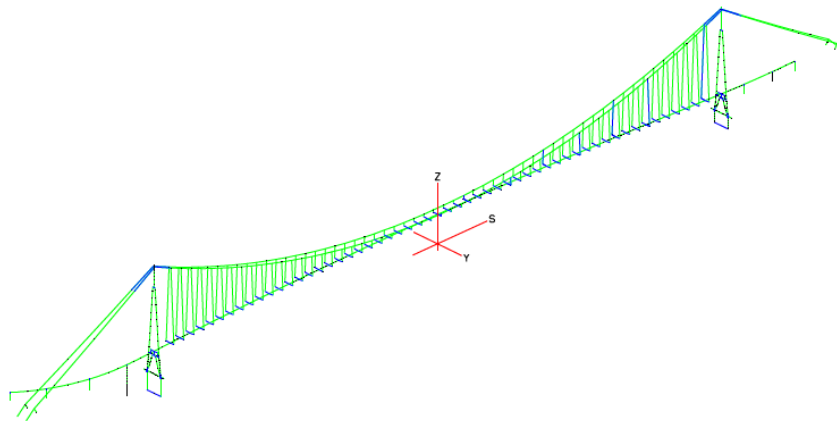

Figure 3.4: FEM model of the Hålaogaland Bridge

A total of 35 vibration modes and corresponding undamped natural frequencies were extracted. Of these the 4 first horizontal, 8 first vertical and 2 first torsional modes were chosen. The remaining modes were dominated by cable or tower motion and are not considered further as they are not suspected to contribute to the flutter stability of the bridge. A total of 70 modes had to be extracted to include the fourth torsion mode, as the relatively high torsional stiffness of

the girder lead to high torsional frequencies. The resulting eigenfrequencies, mode shapes and equivalent modal masses and mass moment of inertia of the 20 chosen modes are presented in Table 3.1. The corresponding mode shapes are plotted in Figure 3.5.
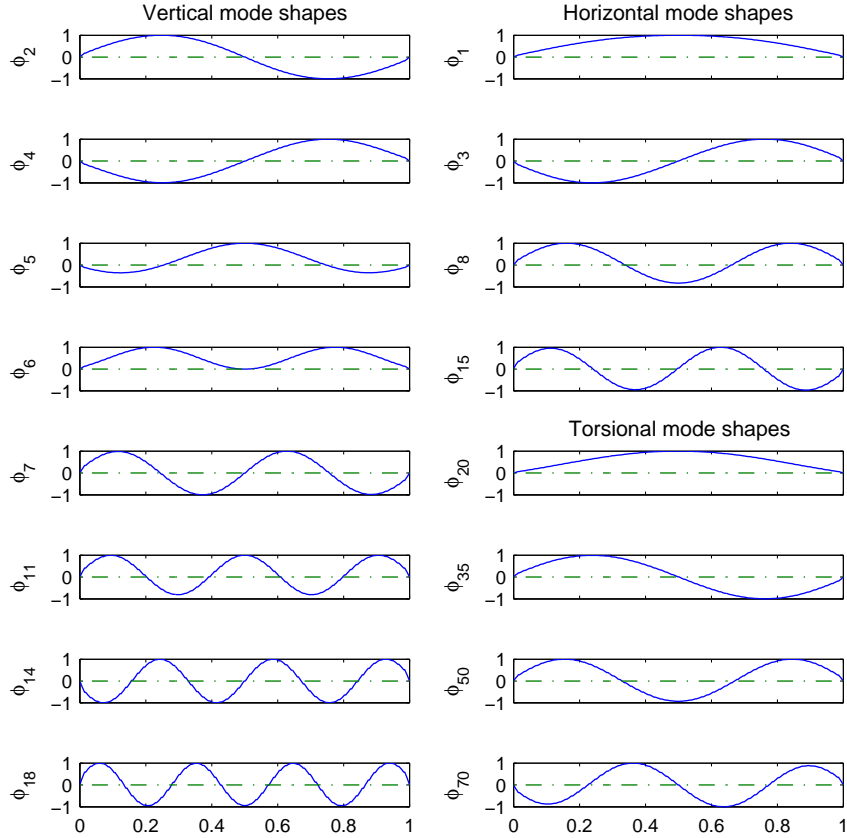

Figure 3.5: The first 8 vertical and and first 4 horizontal and torsional mode shapes

The right column in Table 3.1 contains equivalent modal mass and mass moment of inertia. The denomination is thus kg/m for the vertical and horizontal modes in row 1 to 12, and kgm^2/m for the torsional modes in row 13 to 16. The modal damping ratio is assumed to 0.5 % of critical for all modes.

Mode no. i	Mode type	Natural frequency ω_i (rad/s)	Damping ratio ζ_i (-)	Equivalent modal mass $\tilde{m}_i$ (kg/m - kgm^2/m)
1	1st S. horizontal	0.333	0.005	10 730
2	1st AS. vertical	0.530	0.005	24 323
3	1st AS. horizontal	0.732	0.005	9 524
4	1st AS. vertical	0.837	0.005	22 204
5	1st S. vertical	0.900	0.005	11 318
6	2nd S.vertical	1.259	0.005	11 398
7	2nd AS. vertical	1.362	0.005	11 448
8	2nd S. horizontal	1.393	0.005	9 859
11	3rd S. vertical	1.772	0.005	11 397
14	3rd AS. vertical	2.167	0.005	11 352
15	2nd. AS. horizontal	2.409	0.005	12 257
18	4th S. vertical	2.624	0.005	11 314
20	1st S. torsion	2.771	0.005	361 361
35	1st AS. torsion	3.617	0.005	571 159
50	2nd S. torsion	5.474	0.005	457 120
70	2nd AS. torsion	7.062	0.005	450 959

Table 3.1: Dynamic properties of the Hålogaland Bridge

3.3   Wind tunnel test

The aerodynamic performance of the Hålogaland Bridge is measured by wind tunnel testing of a scaled section model. The tests were performed in FORCE Technology's 2.6 meter wide Boundary-Layer Wind Tunnel 2, in Lyngby Denmark, September 2010. Only test results in relation to the aeroelastic characteristics are presented here. For further details it is referred to the wind tunnel report in [8].

3.3.1   Section model, flow conditions and dynamic test rig

By considering geometry, mass and stiffness of the prototype, a wind tunnel section model of 1:50 geometrical scale was chosen for the Hålogaland Bridge. To reflect the real bridge behavior, the section model is built with crash-barriers and railings scaled to ensure correct dimension, drag force and Reynolds number. The section model is shown in Figure 3.6.
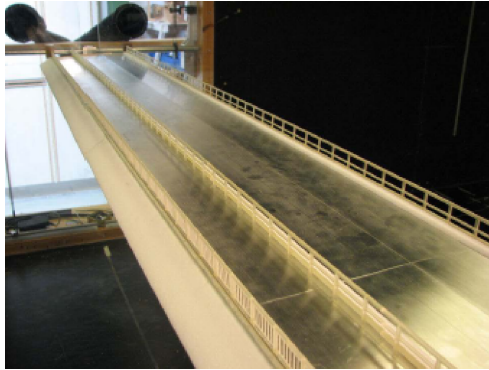
Figure 3.6: Section model of the Hålogaland Bridge [8]

The deck of the Hålogaland Bridge is asymmetric; hence all tests were performed with wind from both westerly and easterly wind direction. For the sake of simplicity, only results from western direction is reported in this project, as this proved to be the direction with the lowest critical wind speed for onset of aeroelastic instability [8]. The section model subjected to western wind is shown in Figure 3.7. It should be noted that all test results presented in this project are for tests without the illustrated traffic configuration.
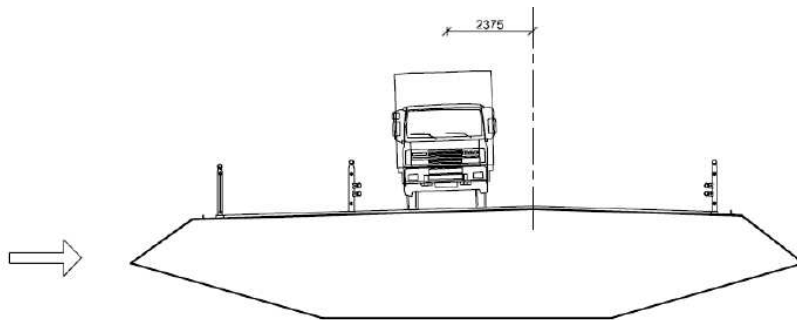

Figure 3.7: Section model with wind from west [8]

The wind tunnel is 2.6 m wide, 1.8 m high and 21 m long. The model was placed 14.5 m downstream of the inlet at mid height of the wind tunnel. Stability tests were performed in both smooth and turbulent wind, while flutter derivatives were measured in smooth flow, using the free vibration technique. For the smooth flow condition, corresponding to an empty wind tunnel, the turbulence intensity was measured to approximately 5 %. The air density ρ was measured to 1.17 kg/m^3.

A dynamic test rig was constructed by suspending the model in elastic springs, with stiffness adjusted to reproduce the frequency ratio between the first symmetric torsional mode and first symmetric vertical mode. The model was restrained in the horizontal direction. The dynamic properties of structure in

vacuum and still-air, and corresponding scaled properties of the section model are given in Table 3.2.

	Prototype		Section model	
	"Vacuum"	"In-air"	Target	Obtained
f_v (Hz)	0.145	0.143	1.24	1.24
f_t (Hz)	0.453	0.451	3.93	3.90
f_t/f_v	3.12	3.15	3.17	3.15
m (kg/m)	11600	11940	4.776	4.78
I (kgm2/m)	351600	355272	0.0568	0.057

Table 3.2: Dynamic properties of prototype structure and section model

The resulting velocity scaling was approximately 1:5.8, where 1.0 m/s in the wind tunnel corresponds to 5.8 m/s in full-scale

3.3.2 Measured critical velocity

The stability test was performed by gradually increasing the wind tunnel speed until self-excited motion was observed. The wind tunnel test results for smooth wind from western direction at different angles of attack are given in Table 3.3. The results are for a section model test without traffic or snow.

Flow	Direction	Angle	$\hat{V}_{cr}$	V_{cr}
			$[(V/\omega_\theta B)$	(m/s)
		-3°	1.15	61
Smooth	West	0°	1.43	76
		3°	1.53	81

Table 3.3: Measured aerodynamic stability limits

3.3.3 Measured aerodynamic derivatives

The method for extracting aerodynamic derivatives employed for the Hålogaland Bridge refers to the first of the three methods mentioned in Section 2.1.3, the free vibration technique. The bridge deck subjected to smooth flow is given an initial displacement consisting of coupled heave and torsion. The decay in amplitude with time is measured and used to identify the flutter derivatives.

Each test series was repeated 10 times for a given wind speed. A system identification algorithm was averaged over these 10 test results. As the model was restrained in the horizontal direction, only aerodynamic derivatives connected to vertical and torsion motion were extracted. The method used to subtract aerodynamic derivatives is based on the original Scanlan notation, i.e. with positive vertical axis downwards. The measurements are adjusted to the notation shown in Figure 2.1 in Section 2.1.2. The test results are shown in 3.8.

The numerical values are presented in Appendix A, where derivatives related to vertical motion are given in Table A.1 and derivatives related to torsional motion are given in Table A.2.

The aerodynamic derivatives are extracted as function of the reduced velocity. Vertical derivatives (H_1^*, H_4^*, A_1^*, A_4^*) are functions of $\hat{V} = V/B\omega_z$, while derivatives related to torsional motion (H_2^*, H_3^*, A_2^*, A_3^*) of $\hat{V} = V/B\omega_\theta$. As a result, the wind tunnel test covers different reduced velocity regimes for the two groups. Aerodynamic derivatives to the left in Figure 3.8 are measured for $\hat{V}$ up to approximately 5, while the right column up to 2.

Interpretation of measured flutter derivatives

To calculate the flutter limit based on the measured flutter derivatives, it is necessary to develop a model describing the development of the aerodynamic derivatives with increased mean wind velocity. There are in general two methods of interpreting the experimental data from the wind tunnel test

- Direct interpretation of experimental results
- Curve fitting of experimental results by statistic regression

In the first method the test results are accepted as actual predictions of the bridge behavior. The experimental data is used directly, by calculating the eigenvalues of the flutter equations at the reduced velocities where the flutter derivatives are measured. However, the experimental data is measured at discrete points and does not yield information about the development between each observation. One must assume that the measurements are realizations of an accepted physical model. By applying the experimental data directly, one does not acknowledge the fact that there are uncertainties in the measurements relative to the underlying model.

Analysis of experimental data should instead be based on curve fitting by statistical regression. A regression analysis determines the mathematical model that provides the statistical best fit of the relationship between an observed variable (the flutter derivative) and the independent variable (the reduced mean wind velocity). This may be expressed as curve fitting by adding a polynomial trend line to a scatter plot on the form

$$y = a_1 + a_2 x + a_3 x^2 + ... + a_m x^{(m-1)} \tag{3.1}$$

where y is the observed variable, x is the independent variable, and a_m is the regression parameters. Eq. 3.1 represents a linear regression model as the model function is linear in the parameters a_m. Linear regression based on least square fits is performed by the function LINEST in Microsoft Excel. The degree of the polynomial is chosen based on the nature of the scatter in the experimental results.

The aerodynamic derivatives are measured for increasing reduced velocities until the stability limit of the two simulated modes in the wind tunnel is reached. It is assumed that the actual flutter limit is found at higher reduced velocities, as the
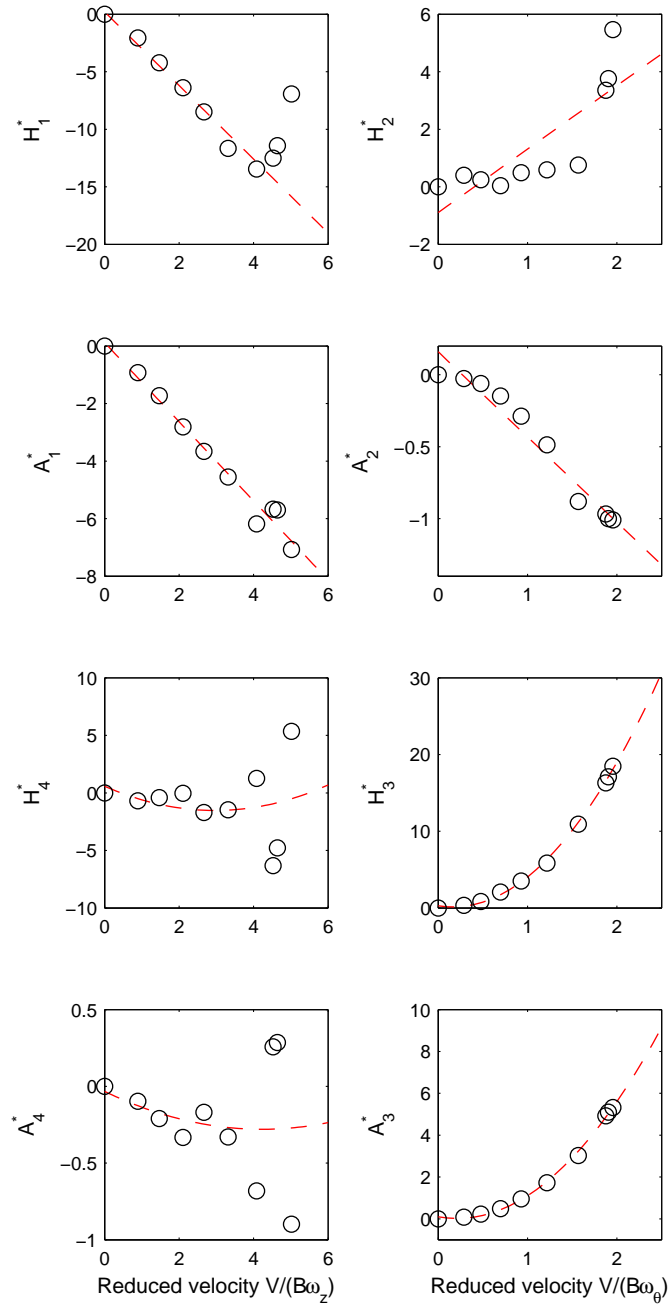
Figure 3.8: The aerodynamic derivatives for the cross section of the Hålogaland Bridge. Open circles mark observation in the wind tunnel and dashed red line indicate the constraint curve fitted to the data.

modes of the actual bridge are dissimilar. For this reason, the continuation of the trend line function for wind speeds exceeding the test regime should also be taken into consideration when choosing a representative polynomial. Incorrect high-velocity behavior could introduce false instability limits. Aerodynamic derivatives in relation to velocity terms (H_i^*,A_i^*, $i = 1, 2$) were approximated with linear models, while the aerodynamic derivatives connected to structural displacement (H_i^*,A_i^*, $i = 3, 4$) were approximated by 2.order polynomials. The chosen trend lines are indicated as continuous lines in Figure 3.8. The numerical values of the coefficients in the regression model are given in Appendix B, Table B.1.

The free vibration method of extracting flutter derivatives was found to work well for tests where the initial excitation was clearly defined. At high wind speeds, the model decayed rapidly, and the useful part of the response history was short [8]. This reduced the accuracy of the estimated flutter derivatives, and is reflected in the increased amount of scatter in the high reduced velocity regime in Figure 3.8 According to the observation, the development of H_1^* indicates a function attaining positive values at high reduced velocities, which is unreasonable. For this reason it is chosen to disregard the 3 last observations in the regression analysis of H_1^*.

The value of the critical mean wind velocity depends on the choice of curve fitting. It is, however, only the approximation of the aerodynamic derivatives at the actual critical reduced velocity that will influence the result. Improved behavior may be achieved by securing good approximations in the velocity regime around the instability limit. Uncertainties related to curve fitting and statistical analysis of the regression models are further discussed in Chapter 5.

3.4 Discrete vortex method simulation

The aerodynamic derivatives of the Hålogaland Bridge are also evaluated by applying a discrete vortex method, implemented in the existing code DVMFLOW. DVMFLOW is COWI's in-house computer code for two dimensional analysis of bluff cross-sections subjected to a free stream. The code is developed in collaboration with the Technical University of Denmark (DTU).

DVMFLOW provides a fast and easy computation of flow around stationary or moving bodies. Hence, it is a useful tool in early design phases before wind tunnel tests are performed, or when wind tunnel tests are evaluated. The aerodynamic derivatives derived from DVMFLOW are used to control aerodynamic derivatives extracted from the wind tunnel. As DVMFLOW also provides aerodynamic derivatives related to horizontal motion and forces, it is useful tool for evaluating the influence of horizontal modes on the stability limit of the Hålogaland Bridge. Some main features of DVMFLOW are presented. For further information it is referred to Larsen and Walther [18].

DVMFLOW is a grid free two dimensional Navier-Stokes solver for bluff body flow. The method is Lagrangian, and the dependent variable is the vorticity and corresponding position of vortices. The laminar diffusion is modeled by random walks of vortices. A Runge-Kutta integration scheme is utilized to derive the response. Each time step is set to 2.5 times a vibration periods.

The flow around the body is specified by a number of flow parameters related to the vortices generated at each time step. Values of these exist in DVMFLOW, based on several previous studies and verifications by COWI. The influence of these parameters on the simulations will not be investigated in the present work.

The geometry of the Hålogaland Bridge is specified in a panel file. The panels discretize the outer geometry of the bridge girder. The size of the panels determines the vortex sizes. A typical number of panels used to resolve the boundary geometry is 200-400, hence a number of 240 is chosen. Detail geometry susceptive to influencing the flow pattern should be included in the model. Railings are modeled by considering their respective area density. The panel size of the detail geometry is chosen to render approximately similar panel sizes as for the bridge girder. The implemented section model of the Hålogaland Bridge is shown in Figure 3.9.
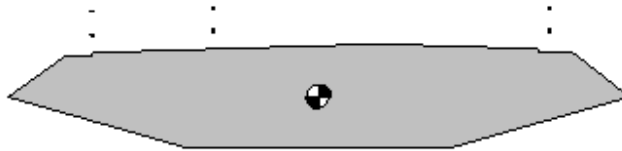

Figure 3.9: Section model of the Hålogaland Bridge implemented in DVMFLOW

Aerodynamic derivatives are extracted from dynamic DVMFLOW simulations using forced harmonic motion in vertical, lateral or angular twist. The extraction is performed by the utility program `aero`. The discrete vortex simulation for heave motion is illustrated in Figure 3.10. The resulting aerodynamic derivatives are given in Appendix A, where coefficients of the constraint curves fitted to the data are indicated in Table A.13 to A.15.

To rely on the results provided by DVMFLOW simulations, model verification tests and convergence studies must be conducted. Factors that influence the accuracy of the obtained flutter derivatives are the integration scheme used for time stepping, the size of the time steps, the number of panels, and the modeling of the flow. In addition, it is questionable how good a 2D model can provide information of 3D load coefficients. These aspects will not be considered further here. The modeling is instead based on past experience at COWI. Hence, it is emphasized that the results provided by DVMFLOW are considered preliminary. Caution should be exercised when drawing conclusions based on the output results.
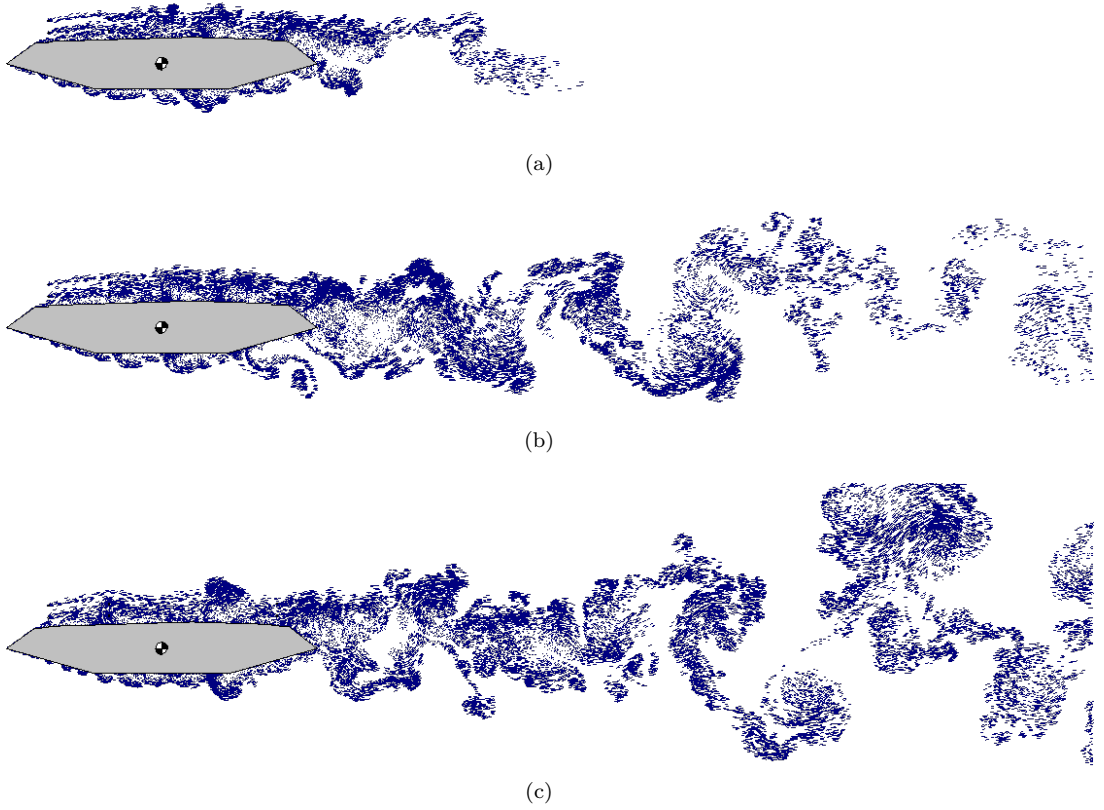
(a)

(b)

(c)

Figure 3.10: DVMFLOW simulation of the cross section of the Hålogaland Bridge subjected to forced harmonic motion in heave, with generated flow pattern after a) 1 time step b) 3 time steps c) 16 time steps.

Chapter 4

Flutter analysis

The flutter limit is assessed by implementing the theory presented in Chapter 2 in MatLab. A bimodal flutter routine based on the flutter equations presented in Section 2.2.1 is implemented in the Matlab script `bimodalflutter.m`. This routine is used to calculate the flutter limit of the section model in Section 4.1.

The generalized multimodal flutter equations are implemented in the MatLab routine `aerostab.m`, developed at NTNU. The routine calculates the roots of the quadratic eigenvalue problem in equation 2.19 in Section 2.2.2, by building the system matrices and utilizing the build-in function `polyeig` in MatLab [19]. The iteration procedure is similar to the one illustrated in Figure 2.4. The input data to the function is specified in the MatLab script named `FlutterHalogaland.m`. This script is used to calculate the flutter limit in both the bimodal and multimodal flutter analysis in the following sections, by specifying the number of investigated modes.

The modal input data and mode shapes of the Hålogaland Bridge, presented in Section 3.2 are summarized in text files. The Matlab files and text files utilized are only submitted electronically.

4.1 Verification of flutter derivatives

A verification of the extracted aerodynamic derivatives is performed by calculating the flutter limit of the section model, and comparing the result with the measured critical velocity in the wind tunnel test. A flutter analysis is conducted by applying the structural properties of the section model together with simulated torsional and vertical frequencies as described in Table 3.2 in Section 3.3. The constant modes of the section model is constructed by setting the value of $\psi_{z\theta}$ to unity. The resulting flutter limit is presented in Table 4.1.

Table 4.1 shows that the flutter limit of the section model calculated with measured aerodynamic derivatives corresponds well with the measured critical wind speed. Both flutter limits are well above the design requirement of 60.2 m/s.The flutter speed of the scaled model is found by applying the scaling ratio 1:5.8, resulting in 74.2 m/s. The measured stability limit is in general expect to be

lower than the limit calculated by aerodynamic derivatives, as the wind tunnel experiment is ended before the actual onset of flutter. However, the measurement may be sensitive to several parameters, among others the accuracy of the applied wind speed in the wind tunnel. As the deviation is small, it can be assumed that the measured flutter derivatives correctly describe the aerodynamic behavior of the section model.

Method of analysis	Critical velocity V_{cr} (m/s)	Critical frequency ω_{cr} (rad/s)	Reduced critical velocity $V_{cr}/(B\omega_{cr})$
Calculated (scaled model)	12.8	17.04	2.02
Calculated (prototype)	73.6	1.99	1.99
Measured in wind tunnel	76.0	2.20	1.43

Table 4.1: Flutter limit of a section model of the Hålogaland Bridge

To futher validate the experimental results, the flutter limit of the section model is calculated with flutter derivatives measured for similar bridges. In addition, flutter derivatives obtained using DVMflow and flat-plate approximations is evaluated. The resulting flutter limit of the section model of the Hålogaland Bridge is shown in Table 4.2.

Aerodynamic derivatives	Critical velocity V_{cr} (m/s)	Critical frequency ω_{cr} (rad/s)	Reduced critical velocity $V_{cr}/(B\omega_{cr})$
Hålogaland	73.6	1.99	1.99
Hardanger	105.0	1.75	3.22
Great Belt	87.8	2.07	2.28
Flat Plate	85.7	1.76	2.61
DVMFLOW	88.7	2.06	2.31

Table 4.2: Predicted flutter limit of a section model of the Hålogaland Bridge

Table 4.2 shows that the applying alternative aerodynamic derivatives yields higher flutter limits than with the flutter derivatives from the Hålogaland wind tunnel test. Especially the critical velocity obtained with aerodynamic properties of the Hardanger Bridge is severely increased. The curve approximation to the aerodynamic derivatives for the bridges in Table 4.2 are plotted in Figure 4.1. The coefficients of the trend lines and their respective experimental data series are given in Appendix A. The flat plate derivatives are described in [28].

The flat plate derivatives serve as an upper reference value of the aerodynamic performance. According to Dyrbye and Hansen [7], closed box-girder sections have critical flutter wind velocities that is approximately 10 % lower than for velocities based on flat-plate aerodynamics. This statement is seen to fit well with the results of the Hålogaland Bridge. Applying the Great Belt Bridge aerodynamics, the flutter calculation of the Hålogaland Bridge yields similar

results to the flat-plate case. The bluffness measured by the B/H ratio of the Hålogaland section is 6.2, while corresponding ratio of the Great Belt Bridge is 7.75. As a result, the aerodynamic properties of the Great Belt Bridge more resemble a flat plate. This is seen in the plot of aerodynamic derivatives in Figure 4.1.

The aerodynamic derivatives extracted from DVMFLOW indicate the same values of the flutter limit as with the Flat plate and Great Belt Bridge derivatives. However, the DVMFLOW output showed severe scatter in some of the data series, which might indicate that the iteration time and time-step of the simulation should be adjusted. Analysis based on DVMFLOW aerodynamic derivatives should be regarded as preliminary, as convergence studies and model verifications should be performed to validate the results. The comparison with the Hardanger Bridge is further investigated in the multimodal analysis in Section 4.3.

In the wind tunnel experiment, the air density is measured to 1.17 kg/m^3. According to Handbook 185, the air density should be set to 1.25 kg/m^3 [26]. This value is chosen in the proceeding flutter analysis.
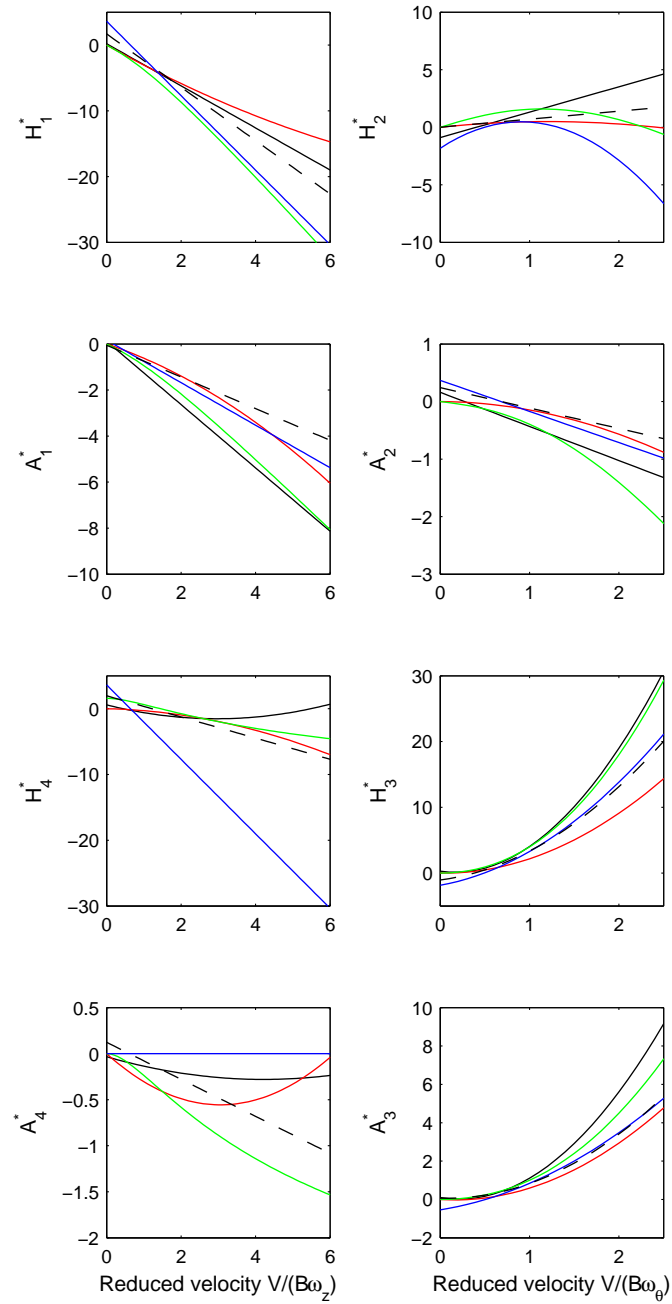
Figure 4.1: Constraint curves fitted to observed aerodynamic data of a section model of the Hålogaland (black), Hardanger (red) and Great Belt Bridge (green). Analytical flat plate (blue) and DVMFLOW model (dashed black) derivatives are also included.

40

4.2 Bimodal flutter analysis

The bimodal stability limits are assessed by considering relevant pairs of still-air vibration modes. Each mode pair consist of a torsional mode and vertical mode.

Two governing factors influence whether modes are likely to couple, namely (1) the degree of shape-wise similarity and (2) the frequency separation between the two modes. The mode shape similarity factor $\psi_{z\theta}$ is given in Eq. 2.17, where values of $\psi_{z\theta}$ close to unity indicate mode coupling. As a starting point to the investigation of possible mode contributions to flutter, a "mode shape similarity matrix" containing $\psi_{z\theta}$ for the combinations of the four first torsional modes and eight vertical modes are given in Table 4.3.

Modes	20	35	50	70
2	0.000	0.999	0.000	0.026
4	0.000	0.998	0.000	0.030
5	0.462	0.000	0.562	0.000
6	0.529	0.000	0.422	0.000
7	0.000	0.000	0.000	0.973
11	0.015	0.000	0.008	0.000
14	0.000	0.000	0.000	0.003
18	0.001	0.000	0.000	0.000

Table 4.3: Mode shape similarity matrix containing $\psi_{z\theta}$ for combinations of torsional and vertical modes, given in columns and rows of the matrix, respectively.

The highest mode shape similarities are found between the asymmetric torsion modes and corresponding asymmetric vertical modes. The mode shape similarities of the symmetric modes in general attain lower values. The reason for this is the vertical bending restraint provided by the cable stiffness, as symmetric modes requires cable elongation. Hence, the asymmetric mode shapes will attain simpler forms, while symmetric modes are more resrained. This is seen in the plot of the mode shapes in Figure 3.5.

Based on the mode shape similarity in Table 4.3, a set mode pairs susceptible to bimodal flutter are chosen. Two-mode flutter limits for various mode combinations are presented in Table 4.4. The purpose of Table 4.4 is not only to find the lowest bimodal combination, but rather to investigate which other mode pairs that might contribute in multimodal coupled flutter.

Mode combination	Critical velocity V_{cr} (m/s)	Critical frequency ω_{cr} (rad/s)	Reduced critical velocity $V_{cr}/(B\omega_{cr})$
5+20	77.9	1.60	2.61
6+20	73.8	1.83	2.17
2+35	122.1	2.17	3.02
4+35	118.9	2.30	2.78
5+50	167.8	3.29	2.74
6+50	172.7	3.07	3.02
7+70	196.2	5.01	2.11

Table 4.4: Bimodal flutter analysis of selected modes

Table 4.4 shows that all investigated mode pairs yields flutter limits above the design requirement of 60.2 m/s. If the fundamental torsional mode is symmetric, it is coupling with the fundamental symmetric vertical mode (mode 5) that traditionally is expected to provide the lowest bimodal flutter limit. For this reason, this is usually the mode pair simulated in the wind tunnel. However, Table 4.4 shows that modes 6 and 20 provide the lowest flutter limit, where mode 6 is the second symmetric vertical mode. These two modes have higher shape-wise similarity and are more closely spaced in terms of natural frequencies, and thus provides a lower flutter limit. The frequency ratios and shape-wise similarity together with the estimated flutter limit are presented in Table 4.5 for the considered combinations of still-air vibration modes. For comparison, the flutter limit computed by Selberg's formula, and for mode shape similarity $\psi_{z\theta} = 1$ is also included.

Modes	Frequency ratio γ	Mode shape similarity $\psi_{z\theta}$	Selberg's Formula V_{cr} (m/s)	Flutter speed $\psi_{z\theta} = 1$ V_{cr} (m/s)	Flutter speed $\psi_{z\theta} \neq 1$ V_{cr} (m/s)
5+20	0.325	0.462	80.9	69.7	77.9
6+20	0.454	0.529	76.4	66.7	73.4
2+35	0.147	0.999	150.0	122.1	122.1
4+35	0.210	0.998	144.2	118.9	118.9
5+50	0.164	0.562	176.8	151.6	167.8
6+50	0.230	0.649	174.8	150.2	172.7
7+70	0.193	0.986	226.9	194.5	196.2

Table 4.5: Bimodal flutter limits for various mode combinations

Obviously, considering mode pairs with $\psi_{z\theta} = 1$ yields a considerable reduction of the flutter limit. Setting the mode shape similarity $\psi_{z\theta} = 1$ correspond to approximating the bridge structure as a rigid section model with constant mode shapes along the span. It underestimates the flutter limit, as modal coupling will be "perfect", and generate large coupling forces.

Estimation of flutter limits by Selberg's formula is considered a conservative approach, as mode shape similarity is assumed to unity. However, Table 4.5

shows that the critical velocity found by Selberg's formula to 80.9 m/s (mode 5+20) overestimates the flutter limit. Selberg's formula assumes bridge sections with aerodynamic derivatives corresponding to a flat plate. Due to its narrow width, the box-section of the Hålogaland Bridge is relatively bluff, and thus the assumption of aerodynamic performance corresponding to a flat plate is questionable. As a result, Selberg's formula provides a poor estimation of the flutter limit.

The results of the bimodal analysis clearly indicate that the instability will be dominated by the first torsion mode. The coupling matrix in Table 4.3 shows that the second torsion mode does not couple with any of the vertical modes that the fundamental torsion couple with. The two coupling processes can be considered as two independent multimodal sub-systems. Hence, the second torsion mode is not suspected to contribute to the governing flutter instability. Mode combinations including the 3rd and 4th torsional frequency (mode 50 and 70) yields very high flutter limits, and is not suspected to contribute in multimodal flutter. This is due to the low frequency ratios, as shown in Table 4.5. The formula for static divergence as stated in Handbook 185, yields a critical static divergence velocity of 101.0 m/s [26]. Several of the bimodal flutter limits given in Table 4.5 are above the static instability limit.

The results in Table 4.4 and 4.5 indicate that instability phenomenon of the Hålogaland Bridge is multimodal coupled flutter, since more than one mode pair provide low critical mean wind velocities. As these are restricted to the fundamental torsion mode, it can be assumed that multimodal interaction will occur with symmetric modes.

4.3   Multimodal flutter analysis

With today's calculation capacity, a multimode analysis including all extracted modes of the Hålogaland Bridge would demand only a little more computer effort than considering specific mode combinations. However, to better understand the underlying physics of the problem, an adequate set of vertical and torsional modes are included based on the results from the bimodal analysis presented above. The results of the multimode flutter analysis are given in Table 4.6.

Mode combination	Critical velocity V_{cr} (m/s)	Critical frequency ω_{cr} (rad/s)	Reduced critical velocity $V_{cr}/(B\omega_{cr})$
5 + 20	77.9	1.60	2.61
6 + 20	73.8	1.83	2.17
5 + 6 + 20	68.1	2.03	1.80
5 + 6 + 11 + 20	67.7	2.05	1.78
8 vert. + 20	67.7	2.05	1.78
2 + 4 + 35	106.1	2.71	2.11
8 vert. + 35	106.1	2.71	2.11
8 vert. + 4 tors.	67.7	2.05	1.78

Table 4.6: Multimodal flutter limit for different mode combinations

The critical flutter velocity drops severely from the bimodal case when the three modes 5+6+20 are considered. Mode 5 and 6, corresponding to the first and second symmetric vertical modes, have natural frequencies about 1/3 and 1/2 of the fundamental symmetric torsion mode. In addition, the mode shape similarities are high; hence both modes are likely to couple with the torsional mode. Mode shapes 5, 6 and 20 are plotted in Figure 4.2. Only a minor reduction of V_{cr} is obtained when the third symmetric vertical mode (mode 11) is included. Further inclusion of additional modes does not affect the flutter limit.

Table 4.6 also includes multimode coupling of asymmetric torsion and asymmetric vertical modes to illustrate the assumption of independent sub-systems. When the sub-system of asymmetric modes is included, the flutter limit does not change. The governing flutter limit of the symmetric mode sub-system is thus independent of the asymmetric sub-system.

Since the critical mean wind velocity converges for the combination of mode 5, 6 and 20, the instability of the Hålogaland Bridge can be characterized as three mode flutter, with a critical mean wind velocity of 68.1 m/s. The critical oscillation frequency ω_{cr} is found to 2.03 rad/s, corresponding to about 3/4 of the still-air torsional frequency. It is also worth noting that the reduced velocity $\hat{V}$ at the flutter limit is 1.80, which is within the reduced velocity regime of the wind tunnel experiment. This strengthens the reliability of the result, as the aerodynamic derivatives at the flutter limit are based on actual measurements and not extrapolated values. In the following analysis, the three mode flutter case is referred to as the reference case.
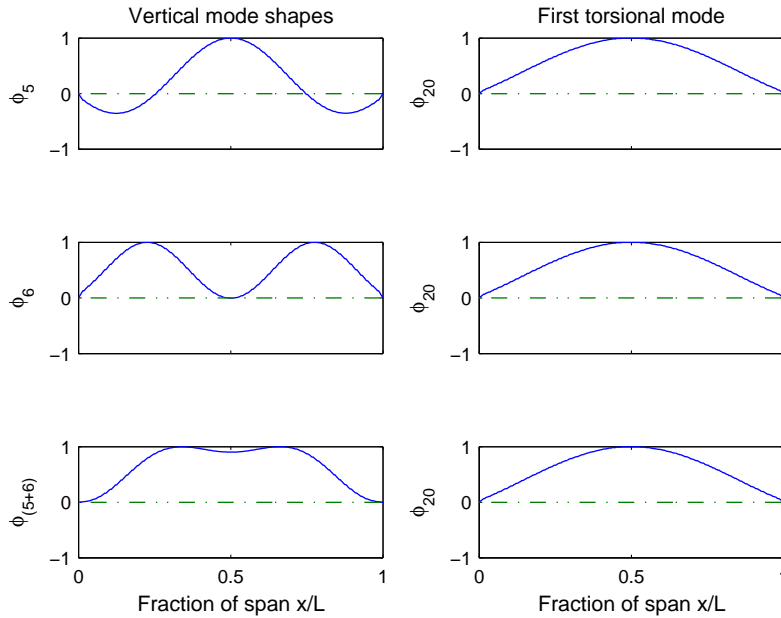

Figure 4.2: Still-air vibration modes 5, 6, (5+6) and 20.

It is noticeable that a sum of still-air vibration modes 5 and 6 is more shape-wise similar to the symmetric torsion mode, than the similarity of the modes regarded individually. This is illustrated in the bottom of Figure 4.2, where mode 5 and 6 is added and normalized to attain a maximum value of 1. The mode shape similarity factor of modes 5+6 summarized and mode 20 in Eq. 4.1 is notably higher than the values of the individual modes presented in Table 4.3.

$$\psi_{(5+6),20} = \frac{\int \phi_{(5+6)}(x)\phi_{20}(x)dx}{\int \phi_{(5+6)}^2(x)dx} \frac{\int \phi_{(5+6)}(x)\phi_{20}(x)dx}{\int \phi_{20}^2(x)dx} = 0.9798 \qquad (4.1)$$

Modal damping ratio and in-wind frequencies of still-air vibration modes 5, 6 and 20 are given in Figure 4.3. VB refers to the vertical branch of the frequencies, while TB refers to the torsional branch. The figure illustrates the development of the coupling effect of the three modes with increasing mean wind velocity. The plot clearly indicates that the torsional mode is the driving mode in the coupling process, as it drops to zero at the flutter limit.
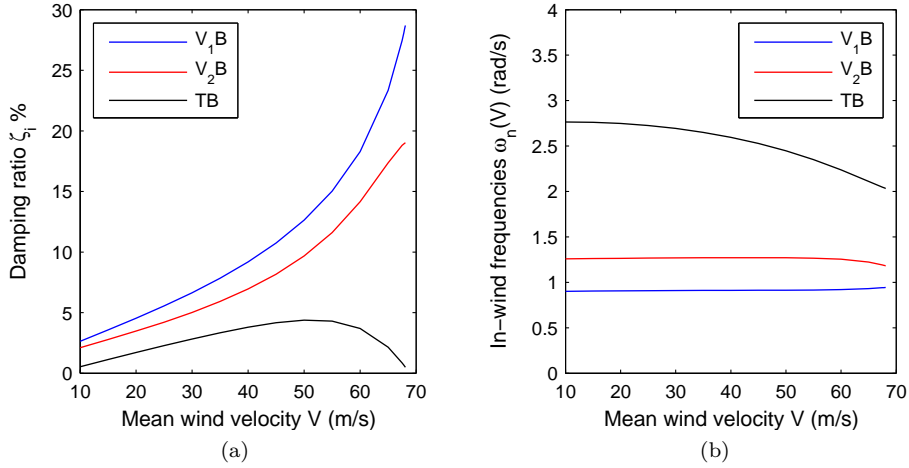

Figure 4.3: a) In-wind total damping ratio and b) In-wind damping ratio

The three-mode flutter limit of 68.1 m/s is above the design requirement of 60.2 m/s. It is, however, worth noting that the critical velocity of 68.1 m/s is considerably lower than the measured critical wind speed in the wind tunnel of 76 m/s. A wind tunnel test is in general considered a conservative estimate of the flutter limit, as mode shape dissimilarity is disregarded. Due to the changes during preliminary design, the torsional frequency of 2.85 rad/s simulated in the wind tunnel was found to 2.77 rad/s in the FEM analysis. As a result, the calculated flutter speed of the wind tunnel model was found to 74 m/s, while a corresponding section model with properties of modes 5+20 in Table 3.1 yields 69.7 m/s. Small differences between properties of the wind tunnel model and final bridge design is difficult to avoid, as wind tunnel tests in general are performed in early design stages.

A calculated section model limit of 69.7 m/s is still not conservative with regards to the reference three-mode limit of 68.1 m/s. The results in Table 4.6 shows that the combination of mode 6 and 20 yields the lowest bimodal flutter limit. As seen in Section 3.3, the wind tunnel test rig of the Hålogaland Bridge was scaled to resemble the fundamental symmetric mode pair, modes 5 and 20. The fundamental mode pair is also the basis of Selberg's formula, and is commonly accepted to provide the lowest flutter limit. Figure 4.2 shows that these modes both have their maximum deflection at mid-span, while the second symmetric vertical mode has its maximum located in the 1/3 fraction of the span length. Hence, there is reluctance towards simulating mode 6 instead of mode 5, as vibrations in general are assumed to occur at mid-span. This is the position where the bridge is most likely to deform. However, a wind tunnel test with a dynamic rig scaled instead to resemble mode pair 6 and 20 could provide a more conservative flutter limit.

Multimodal flutter analysis including horizontal modes

It is investigated whether additional lateral modes have a stabilizing or destabilizing effect of the flutter limit. To perform a three dimensional flutter analysis, it is vital to describe the aerodynamic derivatives connected to horizontal self-excited forces (P_i^*, $i = 1..6$) and aerodynamic derivatives connected horizontal motion (H_5^*, H_6^*, A_5^*, A_6^*). This group is for simplicity referred to as horizontal aerodynamic derivatives (ADs). As only vertical and torsional ADs were extracted in the wind tunnel test of the Hålogaland Bridge, other methods must be applied to describe the horizontal ADs. In the present case, two options have been available.

- Horizontal ADs from DVMFLOW simulations
- Horizontal ADs from quasi-static theory

The ADs extracted from the DVMFLOW simulations should be regarded as approximations, as a 3D analysis is performed on a 2D model. Table 4.2 shows that the flutter derivatives obtained in DVMFLOW overestimates the flutter limit of the section model with about 10 % compared to the flutter limit with ADs measured in the wind tunnel. As emphasized in Section 4.1, results from a flutter analysis with aerodynamic derivatives from DVMFLOW should be considered as preliminary. Nevertheless, the results could indicate possible effects of horizontal modes on the flutter limit.

Horizontal ADs may also be taken from quasi-static theory, as given in Section 2.2.2, by including these in addition to the measured ADs in the wind tunnel test. However, compared to the horizontal ADs from the DVMFLOW simulation, several of the terms in the quasi-static approximation is zero. Hence, the quasi-static approach to horizontal flutter derivatives does not reflect the full coupling behavior of the modes, as several of the self-excited loads are zero. The flutter derivatives including quasi-static horizontal ADs are given in Appendix A, where the static load coefficients obtained in the wind tunnel test are presented in Table A.8 and resulting constraint curves of the horizontal derivatives are given in Table A.9.

Analogues to the mode shape similarity matrix with vertical modes in Table 4.7, the mode shape similarity could indicate whether coupling with horizontal modes is likely to occur. The mode shape similarity of the fundamental torsion mode combined with the first and second symmetric lateral mode (mode 1 and 8) are found to

$$
\begin{aligned}
\psi_{1,20} &= \frac{\int \phi_1(x)\phi_{20}(x)dx}{\int \phi_1^2(x)dx} \frac{\int \phi_1(x)\phi_{20}(x)dx}{\int \phi_{20}^2(x)dx} = 0.9949 \\
\psi_{8,20} &= \frac{\int \phi_8(x)\phi_{20}(x)dx}{\int \phi_8^2(x)dx} \frac{\int \phi_8(x)\phi_{20}(x)dx}{\int \phi_{20}^2(x)dx} = 0.0039
\end{aligned}
$$

The result of the flutter calculation including symmetric horizontal modes is shown in Table 4.7. Both the reference case of three-mode flutter (mode 5, 6 and 20) and a case of bimodal flutter (mode 6 and 20) is used as a basis when adding horizontal modes in the multimode flutter equations. The results indicate that horizontal modes do not affect the flutter stability of the Hålogaland Bridge. Neither inclusion of horizontal aerodynamic derivatives from quasi-static theory or DVMFLOW simulations changes the critical flutter velocity. Similar results were found by applying quasi-static horizontal derivatives of the Hardanger Bridge, see e.g. Øiseth et al. [11].

Mode combination	Critical velocity V_{cr} (m/s)	Critical frequency ω_{cr} (rad/s)	Reduced critical velocity $V_{cr}/(B\omega_{cr})$
6 + 20	91.2	1.87	2.62
1 + 6 + 20	91.2	1.87	2.62
1 + 3 + 6 + 20	91.2	1.87	2.62
5 + 6 + 20	80.2	2.10	2.05
1 + 5 + 6 + 20	80.2	2.11	2.04
1 + 3 + 5 + 5 + 20	80.2	2.11	2.04

Table 4.7: Multimode flutter analysis including horizontal modes with aerodynamic derivatives obtained by DVMFLOW

Mode combination	Critical velocity V_{cr} (m/s)	Critical frequency ω_{cr} (rad/s)	Reduced critical velocity $V_{cr}/(B\omega_{cr})$
6 + 20	73.8	1.83	2.17
1 + 6 + 20	73.7	1.83	2.17
1 + 3 + 6 + 20	73.7	1.83	2.17
5 + 6 + 20	68.1	2.03	1.80
1 + 5 + 6 + 20	68.1	2.03	1.80
1 + 3 + 5 + 5 + 20	68.1	2.03	1.80

Table 4.8: Multimode flutter analysis including horizontal modes with quasi-static aerodynamic derivatives

Regarding the plot of damping in Figure 4.3, the curve of the torsional branch is seen to increase and suddenly drop close to the flutter limit. The damping curve clearly indicates that flutter of the Hålogaland Bridge may be classified as hard-type flutter, dominated by the torsional mode. In a soft-type flutter, the slope of the damping curve is less steep. Hence, the damping genereally is lower. Damping induced by horizontal modes could affect the flutter limit of soft-type flutter bridges [3], as a lower damping curve could be more sensitive to changes in the overall damping.

It is, to the author's knowledge, no other examples than the Akashi-Kaikyo Bridge in Japan where horizontal modes are found to severely influence the flutter limit. Obviously, the aeroelastic behavior of the Akashi-Kaikyo Bridge is not directly comparable to the one of the Hålogaland Bridge studied in this paper. The Akashi-Kaikyo Bridge is currently the world's longest suspension bridge with a center span of 1991 m. The special feature of its truss deck section must be taken into consideration in the comparison. Wind tunnel tests of the Akashi-Kaikyo Bridge revealed high values of static drag C_D, and small values of C'_L and C'_M, compared to a stream-lined section. This resulted in high values of P_3^*, indicating that the Akashi Bridge might be subjected to soft-type flutter [3].

Comparison with the Hardanger Bridge

The Hardanger Bridge and Hålogaland Bridge have several similarities in terms of structural and modal properties. The length and width of the Hålogaland Bridge is 1145 m and 18.6 meters, while corresponding values of the Hardanger Bridge is 1310 m and 18.3 m, respectively. The governing stability limit of the Hardanger Bridge is also classified by three-mode flutter, constituting of the first torsional mode and two first symmetric vertical modes, see e.g. Øiseth et al. [11]. As a consequence, the Hardanger Bridge serves as an important reference to verify the estimated calculations of the Hålogaland Bridge. Some main modal properties of the Hardanger and Hålogaland Bridge are summarized in Table 4.9, where $S1$ and $S2$ refers to the first and second symmetric still-air vibration mode.

Bridge	$\omega_{z,S1}$ (rad/s)	$\omega_{z,S2}$ (rad/s)	$\omega_{\theta,S1}$ (rad/s)	$\tilde{m}_{z,S1}$ (kg/m)	$\tilde{m}_{z,S2}$ (kg/m)	$\tilde{m}_{\theta,S1}$ (kgm^2/m)
Hålogaland	0.90	1.26	2.77	11 318	11 398	361 361
Hardanger	0.89	1.27	2.23	12 820	12 820	426 000

Table 4.9: Structural and modal properties

The first symmetric torsion frequency is higher for the Hålogaland Bridge. The section of the Hålogaland Bridge was initially designed for a main span of 1345 m, which may explain the high torsional stiffness. The A-shaped towers may also be suspected to contribute to the increased torsional stiffness, compared to H-shaped towers of the Hardanger Bridge. It can however be shown that the mode shape configuration of the two bridges is similar. The main flutter

characteristics of the Hardanger and Hålogaland Bridge are summarized in Table 4.10 [11].

Bridge	Modes	Critical velocity V_{cr} (m/s)	Critical frequency ω_{cr} (rad/s)	Reduced critical velocity $V_{cr}/(B\omega_{cr})$
Hålogaland	5,6,20	68	2.0	1.8
Hardanger	4,6,13	78	1.6	2.6

Table 4.10: Flutter limit of Hardanger and Hålogaland Bridge

Table 4.10 shows that the critical mean wind velocity of the Hardanger Bridge is considerably higher than for the Hålogaland Bridge. In general, enhanced torsional stiffness increases V_{cr}. Hence, the Hålogaland Bridge should be expected to provide a higher flutter limit than the Hardanger Bridge. To illustrate this, the reference case flutter limit of the Hålogaland Bridge is recalculated with a reduced still-air torsional frequency corresponding to the one of the Hardanger Bridge. The resulting critical mean wind velocity is 52.4 m/s, a decrease of 23 % of the initial limit of 68 m/s.

It is emphasized that although the bridges are similar in configuration, their aerodynamic properties are measured in two different wind tunnel tests. The flutter limits in Table 4.10 are thus not directly comparable, as the measured aerodynamic derivatives depend on wind tunnel practice, extraction method e.g. For the Hardanger bridge, aerodynamic derivatives were extracted based on the buffeting vibration method, by system identification of response time series [29]. This method differs from the free vibration method described in Section 3.3, as it involves a turbulent wind field. In addition to depending on the wind tunnel test itself, how the measurements are interpreted should also be evaluated. The measured stability limit in smooth flow is given in Table 4.11.

Section model	Flow	Angle	Bicycle lane	V_{cr} (m/s)
Hålogaland	Smooth	0°	Upstream	76.0
Hardanger	Smooth	0°	Upstream	79.5

Table 4.11: Measured critical velocity

Compared to the estimated limit in Table 4.10, the measured flutter limit in Table 4.11 only indicates a small deviation in critical velocity of the two bridges. It should however be remembered that a decrease in torsional frequency from wind tunnel model to final bridge design resulted in a reduction from about about 74 m/s to 70 m/s in the calculated flutter limit of the section model of the Hålogaland Bridge. Possible similar effects of the Hardanger section model vs. bridge are not investigated here.

Based on the results of the measured stability and aerodynamic derivatives, one could draw the conclusion that the aerodynamic properties of the two sections

are somewhat different. The cross-sections of the Hardanger and Hålogaland Bridge are shown in Figure 4.4. Good performance with respect to vortex shedding phenomena was a vital aspect in the design of the Hålogaland Bridge. This is achieved by reducing the inclination angle between the bottom plate and lower inclined plate of the cross section corner to less than 16 degrees [8]. The emphasize on good vortex shedding performance was chosen based on among others the experience with the Osterøy Bridge, a 500 m long span suspension bridges in Norway subjected to severe vortex shedding induced vibrations.

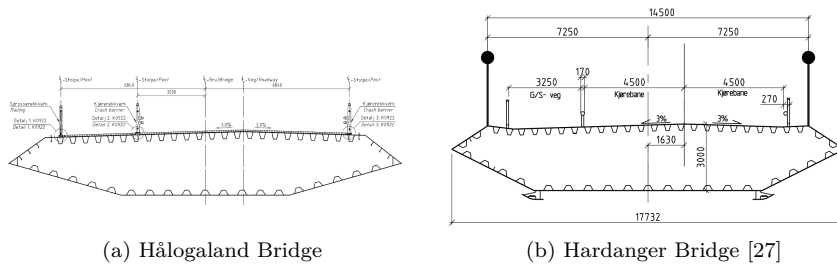(a) Hålogaland Bridge (b) Hardanger Bridge [27]

Figure 4.4: Comparison of deck configuration. Note that the scale of the decks relative to each other are not adjusted

The Hardanger Bridge is constructed with guide vanes to reduce possible vortex shedding vibrations. The wind tunnel test of the Hardanger Bridge indicated that vortex mitigation devices increased the critical flutter velocity in the buffeting response slightly [29]. However, as it is difficult to simulate flow around small details in model scale, conclusions on the effect of the guide vanes with respect to critical flutter velocity should be drawn with caution.

It is not the purpose of this project to conclude which qualities of the two bridges that are good or not, merely to discuss the difference of their respective flutter limits. It is a question whether the design securing good vortex shedding performance of the Hålogaland Bridge might have had an negative effect on its flutter behavior. As vortex shedding vibrations is not a topic of this project, further analysis of guide-vanes, angle inclination and vortex shedding performance is not considered.

Chapter 5

Modeling uncertainty in the prediction of flutter

5.1 Uncertainties in determination of flutter

During the last decades, flutter analysis of cable bridges has been a subject of extensive research. These studies have in general been based on deterministic structural parameters. Estimation of bridge response due to wind-structure interaction is however associated with a number of uncertainties. Hence, flutter analysis could instead be based on a probabilistic analysis, where the critical mean wind velocity is represented as a stochastic variable.

According to Jakobsen and Tanaka [14], the uncertainties related to prediction of aeroelastic response can be descried in three levels: "Fundamentally, the uncertainties stem from the random nature of wind, its inborn variability. Secondly, the lack of understanding of this variability, as well as all the details of wind load generation mechanisms, including wind-structure interaction, increases the uncertainty. Also, simplifications introduced in the mathematical models for wind forces and structural response, streamlined for the design purpose, introduce additional uncertainty."

Obviously, the nature of the wind field as a random process is impossible to describe deterministically. While buffeting response calculation of bridges is based on stochastic modeling, aeroelastic stability calculations are not. In the design requirements for aeroelastic stability, all uncertainties are usually collected in a single safety factor. This factor is specified as 1.6 in Handbook 185 [26].

In addition to handling the random nature of wind, the main difficulty is describing the self-excited loads in the load model. The crucial input in the eigenvalue analysis is the modeling of the self-excited forces in terms of aerodynamic derivatives. Some uncertainties related to the modeling of self-excited forces are presented in Figure 5.1. The purpose of the figure is not to describe all uncertainties, but rather to illustrate how some of the uncertainties arise at different levels in the load model.
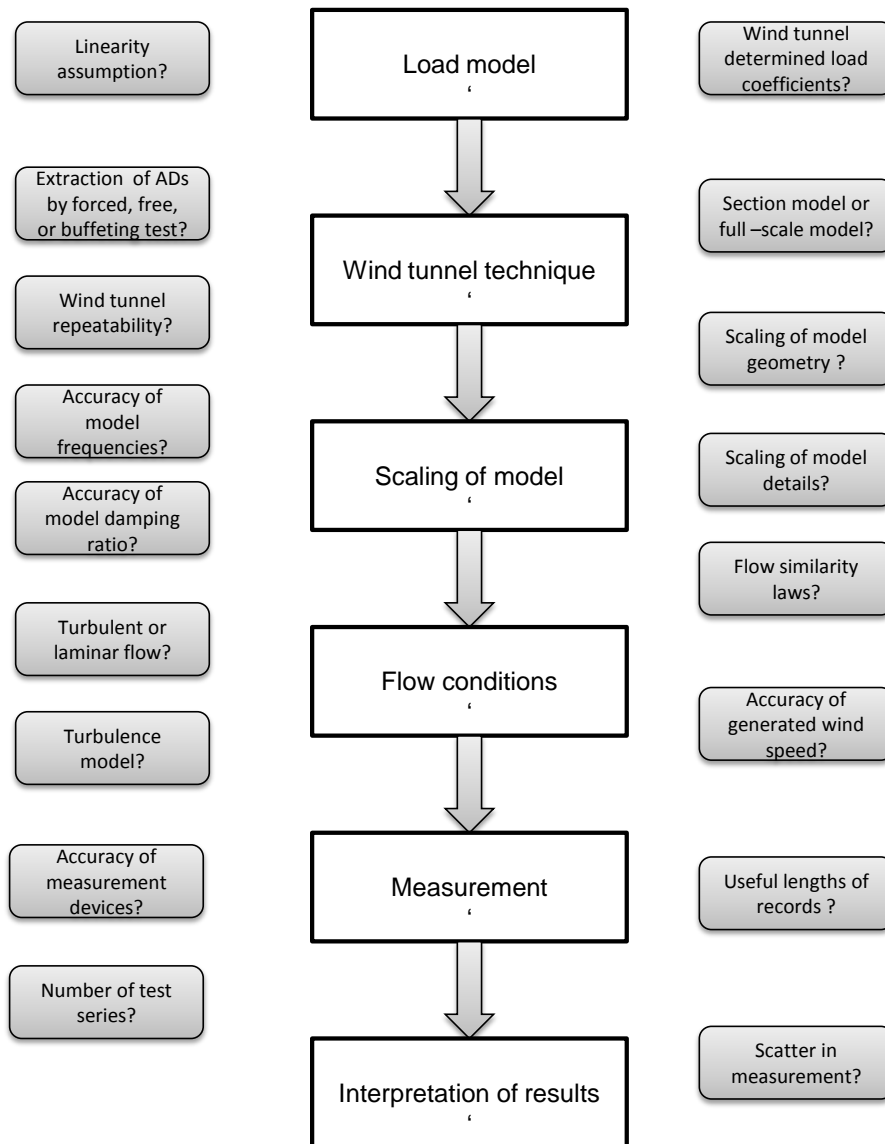
Figure 5.1: Some uncertainties connected to modelling of self-excited forces

The square boxes in the center of Figure 5.1 represent the different stages in the modeling of self-exited loads where uncertainties occur. The surrounding boxes represent sources of uncertainty in the resulting flutter limit. The process markers should not be interpreted as a hierarchic list of importance of uncertainties. They are merely an indication of the order in which the uncertainties occur.

As indicated by the top center box in Figure 5.1, uncertainty arises due to the fundamental assumptions of the load model. Is it a valid assumption to approximate self-excited forces as linearly dependent of structural motion? They are not for for vortex shedding excitation [28]. Is it possible to describe fluctuating forces on a bridge deck by wind tunnel extracted aerodynamic derivatives? On a second level, uncertainty arises due to choice of wind tunnel technique. For instance, how will choice of wind tunnel model (section model or full aeroelastic model) affect the determined flutter derivatives? How will different methods of extracting flutter derivatives yield different results? Further, scaling of the bridge model induces uncertainties. Are all important details reproduced correctly? Is the model tuned with reasonable accuracy? The flow conditions in the wind tunnel lead to another source of uncertainty in the modeling. The true random nature of turbulent wind can never be reproduced to the correct scale. Finally, accuracy of measurement methods and interpretation of test results affect the final description of the self-excited loads.

These sources of uncertainty and others are illustrated in the figure. There are no lines between the levels and the surrounding boxes, as each statement may yield uncertainty in several levels. However, their order of appearance is taken into account by the location in the figure. Possible uncertainties are positioned near the level where they are likely to occur.

Some work of implementing probabilistic flutter analysis has been reported in literature. These works are often conducted in connection with bridges of record breaking span-lengths, see e.g. the reliability analysis on probability of failure for the Great Belt bridge by Ostenfeld-Rosenthal et al. [21]. Ge et al. [10] proposed a reliability analysis of bridge flutter by expressing the limit state function explicitly in terms of random variables, utilizing the first order reliability method. Pourzeynali and Datta [22] presented a reliability analysis based on basic reliability theory, by also considering sensitivity to variation of model parameters. Cheng et al. [4] performed a flutter reliability analysis based on a combination of four different probabilistic methods.

These studies of flutter of long-span bridges focus on reliability analysis. Few studies investigate the statistical properties of flutter response due to parametric uncertainties. The input parameters in the load model are not deterministic, and should be treated as probabilistic variables. This results in a probabilistic flutter analysis, where the flutter limit is described as a function of parameter variation. A probabilistic free vibration and flutter analysis is presented in Cheng and Xiao [5]. In this work, the sensitivity of the flutter limit is determined based on the influence of parameter uncertainty related to structural parameters. Other properties, such as flutter derivatives and structural damping, were assumed deterministic values.

The relative importance of different parameters should be included in the probabilistic flutter analysis. If some parameters may be considered deterministic, it

reduces the required amount of statistical modeling. As a part of the proposed reliability analysis in Cheng et al. [4], the sensitivity of the different reliability indices was also evaluated. The results of the study indicated that the following input parameters had more effect on the flutter reliability than others:

- Basic wind velocity

- Gust speed factor

- Modal damping

- Flutter derivatives

The results indicated further that random variables of cross-sectional properties had little influence, and could be treated as deterministic. With reference to these results, it is desireable to establish a probabilistic analysis where the effect of uncertainties related to the modal damping ratio and flutter derivatives are investigated. The basic wind velocity and gust speed factor does not provide uncertainties directly related to the modeling of self-excited forces. Uncertainties in these parameters are not considered further in the following analysis.

In Kwon [16], the author evaluates the uncertainties that arise during wind tunnel model design and tests. The flutter prediction is based on wind tunnel measurements. The presented probability models of parameters are however based on approximations on a limited number of data, providing an unreasonable high uncertainty of 15 % in the resulting flutter limit.

The bridge designer has little influence on the parametric uncertainties that arise in the wind tunnel. The flutter prediction in the design must be based on parameters extracted from accepted test results. Some of these parameters are subjected to large scatter. Hence, uncertainties arise due to different interpretation of the wind tunnel observations. These uncertainties are represented in the last center box in Figure 5.1.

The sensitivity of the stability limit with respect to scatter of measured flutter derivatives is investigated. The still-air damping ratio is also taken into account as a parameter uncertainty. A probabilistic flutter analysis is established by considering the distribution of critical mean wind velocity due to variation of the considered input parameters. This requires a statistical modeling of the flutter derivatives and still-air structural damping.

5.2 Proposed probabilistic approach

To investigate the sensitivity of the flutter limit due to uncertainties in the input parameters, establishment of a probabilistic flutter analysis is required. A Monte Carlo simulation based procedure is chosen as a proposed probabilistic approach. Monte Carlo simulation (MCS) methods use randomly generated samples of the input variables to access the distribution of the output variable of a process. The method can be summarized in four steps:

1. Define distribution models of the input data

2. Generate random input variables that satisfies the modeled distributions

3. Perform a deterministic analysis based on the generated input variables

4. Aggregate the results

Basically, the method performs a large number of deterministic flutter analyses, so that statistics can be performed on the resulting distribution of output variables describing the flutter limit. The parametric uncertainty of flutter derivatives and structural damping ratio are included by modeling these as probabilistic input variables. The modeling uncertainty is assumed to be represented by a normal distribution. It is further assumed that the uncertainty of structural damping and flutter derivatives are independent. All other input variables are assumed deterministic.

Monte Carlo simulations will only yield valuable results if the number of simulations is sufficiently high so that convergence is reached. Convergence studies are thus a vital part of the proposed probabilistic analysis. In addition, the generated input parameters must indeed be random, to provide valuable results. This is important so that the input variables represent the underlying distribution with reasonable accuracy.

The MCS method provides high accuracy results, but requires a large number of simulations. The efficiency of the method is thus determined by the amount of computation time needed for one simulation. A crucial aspect is whether the output variable is a result of a series system or parallel system. An engineering comparison of these is a statically determinant and indeterminate structural system, respectively. If one member fails in a statically determinant system, the structure will go to failure. However, if the same member fails in a statically indeterminate system, the system will relocate the forces to other parts of the structure. It is thus not evident that the structure will collapse, and several possible failure mechanisms must be considered. Hence, a MCS evaluation of a parallel system would demand an enormous amount of computational effort, as several parallel failure options must be considered in each simulation. Evaluation of aeroelastic stability represents a series system; either the flutter limit of the bridge is reached, or it is not. Hence, the MCS method is found suitable to perform a probabilistic flutter analysis.

5.3 Probability density distributions

The proposed probabilistic flutter calculation will result in a data set of critical mean wind velocities and critical oscillation frequencies with a sample size corresponding to the chosen number of simulations. To achieve an extended understanding, it is desirable to compare the simulated data with established theoretical probability density distribution (PDF). By determining the shape of the assumed underlying distribution of the generated results, it is possible to predict tendencies of the physical phenomenon. Confidence intervals based on the fitted theoretical distributions is an effective tool when assessing the sensitivity of the flutter limit with respect to the modeled parameter uncertainty.

Theory concerning probability density distributions and distribution fitting is found in Benjamin and Cornell [1] and Nishijima [20].

A statistical fit is obtained by comparing the frequencies observed in the data to the expected frequencies of a theoretical distribution. There are a large number of established theoretical probability distributions available. Each is based on a fundamental physical assumption. Probability distributions are classified by a set of parameters. For instance, the well known Normal distribution is classified by a mean value and a standard deviation, which are the statistical moments of the distribution.

Fitting a distribution to a data set is often a problem of choosing among a collection of established statistical models, and then estimating its parameters. Two commonly used methods of estimating parameters are the methods of maximum likelihood and method of moments. To describe all aspects of the distribution of critical mean wind velocity obtained in the MCS, an infinite number of estimators are acquired. Hence, the theoretical distributions will never fully reflect the distribution of empirical data. Confidence intervals of the estimators and P-P and Q-Q plots will describe the accuracy of the fit.

A proposed theoretical model may be verified by comparing the predictions with the observed data. Such model verification is in general based on two methods: (1) graphical tests by assessment of the shape of the distribution or (2) analytical goodness-of-fit hypothesis testing. Only the first of these two methods are described here.

One graphical model verification method is performed by comparing a histogram plot of the empirical data with the shape of a theoretical PDF. How well the critical velocity distribution is described by the model is determined by visual comparison of the similarity of the two shapes. A second graphical assessment is the probability plot, where the cumulative histogram of the data is compared with a theoretical cumulative density distribution (CFD). The scale of the axes is adjusted so that the theoretical CDF attains a straight line. An example is the normal probability plot. If the data is normal distributed, the plot of the data values will be linear. Curvature in the sample plot implies that the data is better described by another distribution.

The scope of this project is not to develop a statistical model, but rather to indicate whether the output variables from the probabilistic flutter analysis can be approximated by a probability distribution. Hence, only graphical considerations on possible fit to models are elaborated on, to suggest a distribution family of the data. The choice of distribution type is fundamental for an accurate representation of the physical phenomenon. It is thus important to gain some basic knowledge of their underlying assumptions. For simplicity, three families of theoretical distributions are investigated. These are the normal distribution, the lognormal distribution and types of extreme value distributions. Their main characteristics are outlined in the following.

Normal probability distribution

The normal distribution, also known as a Gaussian distribution, is the single most used statistical model in probability theory [1]. It is based on the central

limit theorem which states that under general conditions, the sum of a large number of random variables is distributed normally. The bell-shaped form of the distribution is characterized by a mean value μ and a standard deviation σ (or variance σ^2). The probability density function of a normal distribution is given by

$$f_X(x) = \frac{1}{\sigma\sqrt{2\pi}} \exp -\frac{1}{2}\left(\frac{x-\mu}{\sigma}\right)^2$$

The area under the curve of the probability density function may be divided in three areas, as shown in Figure 5.2. About 68 % of the values generated by a normal distribution will lie one standard deviation away from the mean, about 95 % will lie within two standard deviations and 99.7 % will lie within three standard deviations. This property is used to evaluate confidence intervals of the distribution.

Due to the central limit theorem, a sum of two normal distributed variables will also be normal distributed, if the variables are independent. The sum of two normal distributions is described by a mean equal to the sum of their means and variance equal to a sum of their variances.

The normal distribution is often chosen when no physical character imply that other distributions are more adequate. It is widely applied when the data sample is roughly bell-shaped and symmetric. Examples of physical distributions that frequently are modeled as normal distributed are errors in measurements, representing deviations of specified values.
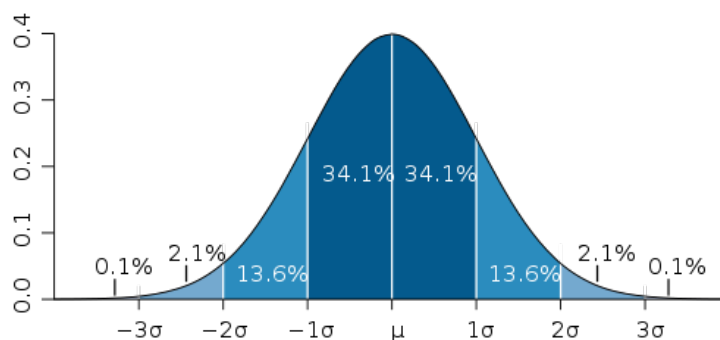

Figure 5.2: Normal probability distribution. The dark, medium and light blue area marks the area covered by values 1, 2 and 3 standard deviations away from the mean, respectively.

Lognormal probability distribution

Where normal distribution arises when the parameters are a sum of random effects, the lognormal probability distribution describes a phenomenon that occurs due to multiplicative nature of random variables. A lognormal distribution

describes random variables whose logarithm is normally distributed. The lognormal probability density distribution is given by

$$f_X(x) = \frac{1}{x\sigma\sqrt{2\pi}} \exp\left[-\frac{1}{2}\left(\frac{\ln x - \mu}{\sigma}\right)^2\right], \quad x > 0 \qquad (5.1)$$

Here, the parameters μ and σ are the mean and standard deviation of the variables logarithm. μ and σ is also referred to as a location and scale parameter, respectively. Note that the values of x must be larger than zero. Compared to a normal distribution, the most significant difference is the skewed shape, as illustrated in Figure 5.3.
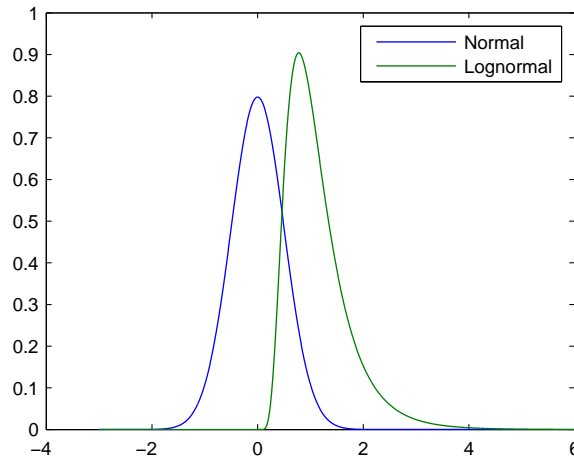
Figure 5.3: Example of normal (blue) and lognormal (green) probability density distribution with μ=0 and $\sigma = 0.5$.

Like the normal distribution, the lognormal distribution is widely used for civil engineering applications. It is often chosen to model phenomena that can be described by multiplication of several random distributed factors. In the proposed probabilistic flutter analysis, the outcome critical mean wind velocity depends in a complicated way on the normal distributed input parameters. This relation involves both summary and multiplicative nature. Hence, a lognormal distribution might provide a better fit to the output data.

Generalized extreme value probability distributions

Extreme value distributions describe the limiting distribution of the minimum or maximum of very large collections of independent random variables. They are often chosen when modeling extreme events. An example is extreme mean wind velocity events, measured over several years based on annual maxima. The distribution of annual maxima is then expected to follow an extreme value distribution. An extreme value distributions is classified by a location factor μ,

describing the location of the cluster of values, a scale factor σ, and a shape factor k. The shape parameter k describes the tail behavior of the distribution. A distribution is classified as right-skewed or left-skewed depending on the tail behavior. Elongation of the tail on the right side represents a right-skewed distribution, where the mean value is located to the right of the peak of the distribution.

There are several types of extreme value distributions. The choice of distribution depend on whether the limiting distribution of smallest or largest values are of interest. They are classified by their tail behavior. If $k = 0$ the tail of the distribution decrease exponentially, and the distribution is classified as a Gumbel distribution. If $k > 0$, the tail will decrease with a polynomial form, resulting in a Frechet distribution. Finally, if the tail is finite, the distribution is known as a Weibill distribution, where $k < 0$. These three distributions are also known as type I, II and III extreme value distributions, respectively. The three types are illustrated in Figure 5.4.
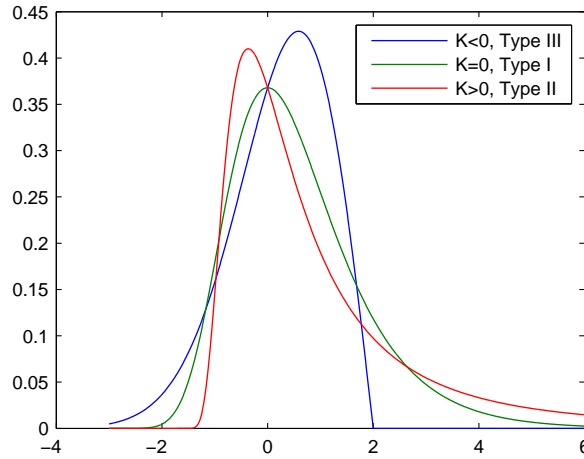

Figure 5.4: Generalized extreme value distribution of type I, II and III, k equal to 0, 0.5 and -0.5 respectively. The shape factor is 1 and location factor 0.

The generalized extreme value distribution combines these three simpler distributions into a single form. Hence, fitting a generalized extreme value distribution to observed data evaluates all three types, and among these chooses the best fit according to the nature of the data. The probability density function of a generalized extreme value distribution is given by

$$f_X(x) = \left(\frac{1}{\sigma}\right) \exp\left[-\left(1 + k\frac{(x-\mu)}{\sigma}\right)^{-\frac{1}{k}}\left(1 + k\frac{(x-\mu)}{\sigma}\right)^{-1-\frac{1}{k}}\right] \qquad (5.2)$$

Eq. 5.2 describes a maximum extreme value distribution, hence a right-skewed distribution. The mirrored, left-skewed, Gumbel distribution is generally denoted an extreme value (EV) distribution, yielding a minimum extreme value distribution.

5.4 Proposed modeling of parameter uncertainty

The uncertainty in the input variables of the probabilistic flutter analysis is assumed to be modeled by a normal distribution. Only uncertainties related to aerodynamic derivatives and structural damping ratio is considered. All other input parameters are assumed deterministic. The suggested probabilistic modeling of the probabilistic input paramaters is explained in the following.

5.4.1 Parameter uncertainty related to aerodynamic derivatives

Aerodynamic derivatives measured in wind tunnels often provide test results subjected to large scatter. In general, the flutter limit is predicted based on constraint curves fitted to the observed data. Hence, different interpretations and choice of constraint curves provides sources of uncertainty in the flutter analysis. It is desirable to investigate to which extent this uncertainty affects the accuracy of the established flutter limit. Different interpretations and a suggested modeling of uncertainties are presented.

Interpretation of flutter derivatives from wind tunnel tests

Interpretation of experimental data by constraint curves from linear regression models is briefly discussed in Section 3.3. There are several ways of interpreting the scatter in wind tunnel test results, depending on the scope of the calculation and the nature of the scatter. It is imported to secure that the constraint curves chosen renders the observed aerodynamic behavior with good accuracy. Four possible interpretation cases for choosing constraint curves to data of the Hålogaland Bridge are suggested in Table 5.1.

Case 1	Choose constraint curves that provide a good behavior of the curves also outside the range of the experimental data
Case 2	Choose constraint curves with high polynomial degrees to improve the statistical fit in the regression model.
Case 3	Choose constraint curves based on the six first observations in the data set
Case 4	Choose constraints curves based on the best fit to the observations around the flutter limit

Table 5.1: Different interpretations of experimental data

Case 1 corresponds to the curve approximation utilized in the deterministic analysis in Chapter 4. In the bimodal analysis, several combinations of still-air vibration modes were investigated to determine possible contributions to multimodal flutter instability. Beacause of this, effort was given to secure a good high-velocity behavior of the constraint curves, to seclude possible false

instability limits outside the velocity regime of the experimental data. A linear approximation was chosen for the damping derivatives, while second degree polynomials were chosen for derivatives related to stiffness.

In the following probabilistic flutter analysis, only the reference case of three-mode flutter is considered. As seen in Table 4.6, multimodal effects have decreased the critical reduced velocity within the range of the experimental data $((V/B\omega_\theta)_{max} = 1.95)$. Due to multimodal coupling, the estimated critical mean wind velocity is lower than the critical velocity of the section model in the wind tunnel test. Hence, the choice of curve approximation is more flexible, allowing higher order degrees of polynomials. Case 2 fits second degree polynomials to all flutter derivatives. Hence, it provides a better overall fit to the data.

The wind tunnel report indicates that the stability limit of the section model is reached in the observations at the three highest reduced velocities. Hence, the aerodynamic derivatives extracted from these test series provided large scatter [8]. For this reason, Case 3 represents curve approximations based on the six first observations of the experimental data sets. In this way, the interpretation in Case 3 supports the assumption that the development of the physical model is better represented in the low velocity regime. A disadvantage of this interpretation is that the aerodynamic derivatives at the flutter limit will be based on extrapolated data, rather than observations.

The constraint curves in Case 4 are based on the five observations closest to the flutter limit, and neglects the other observations. This provides the most accurate flutter velocity with respect to the experimental data. However, one could argue that this interpretation is wrong, as it does not acknowledge the underlying physical model.

The different curve approximations are shown in Figure 5.5. The respective coefficients of the regression models are given in Appendix B, in Table B.1 to B.4. To illustrate how the interpretations of the flutter derivatives affect the flutter limit, a deterministic flutter analysis of the suggested cases is evaluated. The results are presented in Table 5.2.

Constraint curve of aerodynamic derivatives	Critical velocity V_{cr} (m/s)	Critical frequency ω_{cr} (rad/s)	Reduced critical velocity $V_{cr}/(B\omega_{cr})$
Case 1	68.1	2.03	1.80
Case 2	68.7	2.03	1.82
Case 3	67.7	2.04	1.78
Case 4	69.2	2.00	1.86

Table 5.2: Deterministic flutter limit of the Hålogaland Bridge based on different interpretation of measured aerodynamic derivatives.
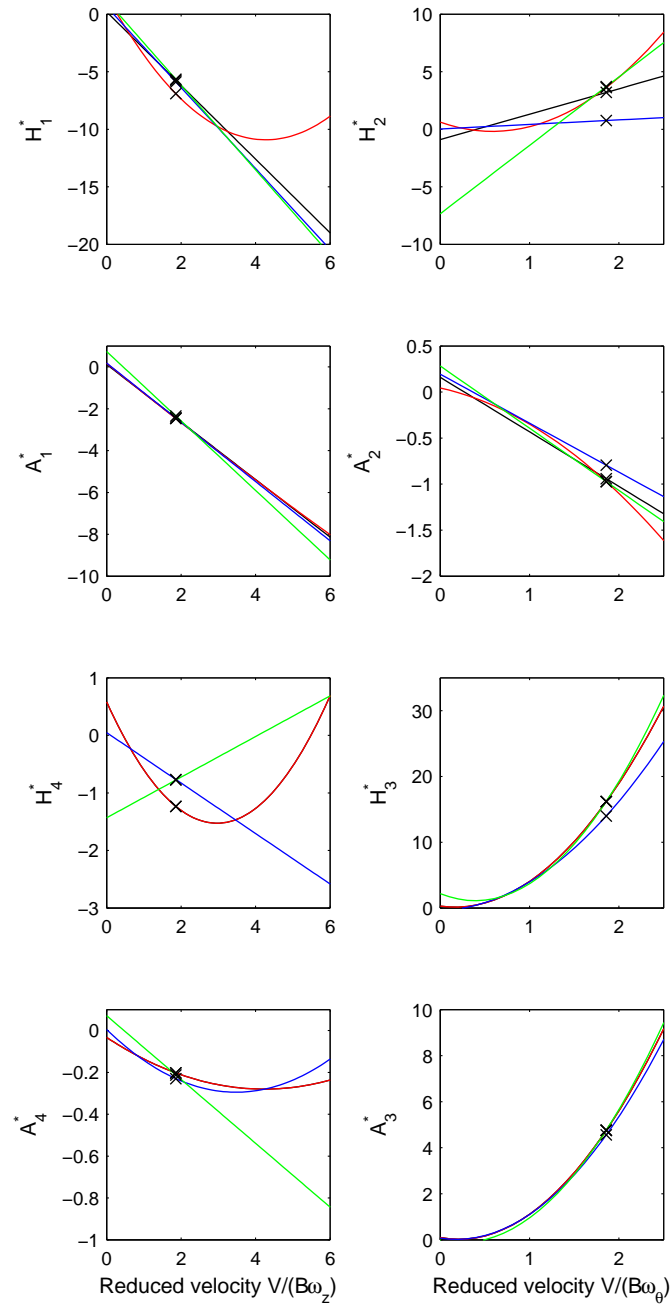
Figure 5.5: Examples of constraint curves fitted to wind tunnel test results of the Hålogaland Bridge by Case 1 (black), Case 2 (red), Case 3 (blue) and Case 4 (green). The cross marks the value at the flutter limit in the deterministic analysis.

62

The results in Table 5.2 show that the different interpretations of aerodynamic derivatives yield rather insignificant differences in terms of critical mean wind velocity. It is only the magnitude of the flutter derivatives at the flutter limit that affects the final predicted critical velocity. Regarding Figure 5.5, the black crosses indicate the point on the curves corresponding to the flutter limit of the deterministic analysis in Chapter 4. The vertical spacing between the crosses indicates what effect the different approximations will have on the predicted flutter limit. As seen in the Figure, the curves are relatively closely spaced near the flutter point. The aerodynamic derivatives which are recognized as the most influential, A_1^*, A_2^*, A_3^* and H_3^*, show only small deviations [7]. Hence, a deterministic analysis of these curves yield similar results, as shown in Table 5.2. Another combination of still-air vibration modes, yielding a different point along the flutter curves, could provide a larger deviation of the predicted critical mean wind velocity for the considered cases.

Modeling of uncertainties in the probabilistic flutter analysis

Investigating the effect of scatter in regression analysis is in statistical terms known as hypothesis testing. Literature regarding this subject is found in Benjamin and Cornell [1]. If a regression analysis is performed on a set of observations to construct a regression model, then the deviation between the modeled value $\bar{X}$ and an observed vale X_i is known as a residual $\hat{\epsilon}$. The residual represents the "fitting error".

The uncertainties in the constraint curves with respect to scatter in the wind tunnel observations are reflected in the magnitude of the respective residuals. Hence, scatter of the aerodynamic derivatives may be modeled by including the residuals in the flutter analysis.

In a regression analysis, the fit of the data is determined by minimizing the sum of least squares. Due to the assumption of statistical best fits, the residuals should in theory be represented by a normal distribution around zero. The better the fit of the data, the more random is the distribution of residuals. Hence, for the assumption of normal distributed residuals, it is vital to secure that the regression models given by the constraint curves provides a good fit to the data. Poor statistical fit leads to high residuals, which in terms could introduce false effects in the described aerodynamic behavior.

For this reason, the probabilistic flutter analysis should be based on curve approximation of Case 2 in Table 5.1, as this regression model provides the overall best fit to the data. As seen in Table 5.2, Case 2 is not the most conservative approach as it yields a slightly higher flutter limit than Case 1. However, as the difference in critical mean wind velocity is of size 0.5 m/s, this effect is neglected.

In the deterministic flutter analysis in Chapter 4, the last observations of H_1^* were neglected when determining the constraint curve. This was an engineering decision due to the unreasonable development of H_1^* towards positive values at high velocities, as seen in Figure 3.8. A regression model based on the 6 first data points does however provide high residuals. Figure 5.5 shows that the polynomial approximation of H_1^* by Case 2 yields a reasonable approximation

to the data in the velocity regime around the flutter limit. As only the three-mode flutter reference case is considered, the unreasonable development of H_1^* at high reduced velocities is insignificant.

Plots of the constraint curves and corresponding residuals are shown in Figure 5.6. The blue and red lines represent the bounds of the residuals, by marking the maximum and minimum value of the residual for the given derivative, respectively. The size of the residual bounds of the different aerodynamic derivatives in Figure 5.6 differs severely. This reflects the amount of scatter in the wind tunnel observation. While H_3^* and A_3^* show clear trends, aerodynamic derivatives H_4^* and A_4^* are subjected to large scatter.

A probabilistic modeling of the aerodynamic derivatives is suggested by choosing different curves from adding or subtracting a shift value to the constraint curves for each simulation in the probabilistic flutter analysis. This shift value should be based on the residuals of the respective constraint curve. The blue and red lines in Figure 5.6 represent the upper and lower bound of the interval where the curve is chosen.

The probabilistic input variable in the Monte Carlo simulation is the shift values. The shift values are generated from assuming normal distributed residuals. Due to the assumption of statistical best fit, the mean values of the normal distributions are zero. The variance of each of the observation series is given by

$$\sigma^2 = \frac{1}{N} \sum_{i=1}^{N} (x_i - \hat{x}_i)$$

Where x_i is the observed value and $\hat{x}_i$ is the predicted value, and $i = 1..N$ is the number of observations. As the aerodynamic derivatives are extracted in the same wind tunnel experiment, it is unreasonable to assume that the individual measurements are independent. Hence, modeling of uncertainty should include effect of dependence between the flutter derivatives. This is achieved by generating random variables from a normal distribution of residuals, including the sample covariance of the residuals from the different derivatives, given by

$$Cov_{ij} = \frac{1}{N} \sum_{k=1}^{N} (x_{i,k} - \hat{x}_i)(x_{j,k} - \hat{x}_j) \tag{5.3}$$

If aerodynamic derivatives H_1^* and H_2^* are considered, the covariance of the residuals of H_1^* and H_2^* indicates how much information a measurement of one variable, H_1^*, will provide of the measurement of the other variable, H_2^*. The covariance matrix is calculated based on the variables and their respective observations as given in Eq. 5.3. For the given wind tunnel experiment, there are 8 variables, the flutter derivatives. Each variable is described by 10 observations; the magnitude of the respective residuals. Note that the observation at zero velocity is included. The covariance matrix is given by the 8×8 matrix in Table 5.3.

64

$COV(i,j)$	H_1^*	H_2^*	H_3^*	H_4^*	A_1^*	A_2^*	A_3^*	A_4^*
H_1^*	3.55	1.25	0.48	3.21	0.03	0.08	0.09	-0.28
H_2^*	1.25	0.49	0.15	0.80	0.06	0.03	0.04	-0.06
H_3^*	0.48	0.15	0.08	0.38	0.01	0.01	0.01	-0.03
H_4^*	3.21	0.80	0.38	9.71	-0.87	-0.02	-0.12	-1.11
A_1^*	0.03	0.06	0.01	-0.87	0.13	0.01	0.03	0.11
A_2^*	0.08	0.03	0.01	-0.02	0.01	0.00	0.00	0.00
A_3^*	0.09	0.04	0.01	-0.12	0.03	0.00	0.01	0.02
A_4^*	-0.28	-0.06	-0.03	-1.11	0.11	0.00	0.02	0.13

Table 5.3: Covariance matrix of residuals

The dependence between the derivatives is described by the off-diagonal terms in Table 5.3. To evaluate the amount of dependence, the respective correlation coefficients are evaluated, given by

$$\rho_{ij} = \frac{Cov_{ij}}{\sigma_i^2} \tag{5.4}$$

The correlation coefficient is a non-dimensional indicator of variable dependence. Values of ρ_{ij} equal to 0 describe two independent variables X and Y. Values of ρ_{ij} close to 1 indicate full dependence. A change in variable X results in a corresponding change of variable Y. Negative covariance describes negative dependence. The correlation coefficient matrix is given in Table 5.4. Obviously, the correlation coefficient matrix will be symmetric and have 1 along its diagonal.

$\rho(i,j)$	H_1^*	H_2^*	H_3^*	H_4^*	A_1^*	A_2^*	A_3^*	A_4^*
H_1^*	1.00	0.95	0.89	0.55	0.05	0.73	0.53	-0.41
H_2^*	0.95	1.00	0.75	0.37	0.22	0.85	0.64	-0.23
H_3^*	0.89	0.75	1.00	0.42	0.10	0.60	0.53	-0.28
H_4^*	0.55	0.37	0.42	1.00	-0.78	-0.08	-0.40	-0.98
A_1^*	0.05	0.22	0.10	-0.78	1.00	0.61	0.85	0.86
A_2^*	0.73	0.85	0.60	-0.08	0.61	1.00	0.89	0.21
A_3^*	0.53	0.64	0.53	-0.40	0.85	0.89	1.00	0.53
A_4^*	-0.41	-0.23	-0.28	-0.98	0.86	0.21	0.53	1.00

Table 5.4: Correlation coefficient matrix of residuals

In the wind tunnel test, the flutter derivatives are extracted based on recorded time series of vertical and torsional motion of the section model. These time series are used to extract the aerodynamic derivatives related to vertical motion (H_i^*, A_i^*, $i = 1, 4$), and torsional motion (H_i^*, A_i^*, $i = 2, 3$), respectively. Hence the covariance matrix should indicate that the observations of torsional derivatives are from one time series, while the vertical derivatives are from another. This statement is investigated in a no-correlation hypothesis test, by calculating the matrix of P-values of the correlation matrix in Table 5.4. Each P-value is the probability of getting correlation as large as an observed random variable by

random chance. This is performed by the built-in function `corrcoef` in Matlab [19]. If $P(i,j)$ is small, e.g. less than 0.05, the correlation of the two variables at position (i,j) in the correlation matrix is significant. The P-value matrix is given in Appendix B, Table B.6. The following pairs yield P-values lower than 0.05:

- H_2^* with H_3^* or A_2^*

- A_1^* with A_4

- A_2^* with A_3^*

This indicates that the extraction method applied in the wind tunnel leads to dependent observations between aerodynamic derivatives of vertical motion and of aerodynamic derivatives of torsional motion. However, the P-values of the following pairs indicate that the dependence is independent of vertical or torsional motion:

- H_1^* with H_2^*, H_3 or A_2^*

- A_1^* with A_3^*

The result of the P-value test verifies the assumption of dependence between the uncertainties of the flutter derivatives. Hence, the assumed normal distribution of residuals should be characterized by zero mean values and the covariance matrix in Table 5.3. Uncertainties due to scatter in the experimental data describing aerodynamic derivatives are included in a probabilistic flutter analysis by adding a random normal distributed residual for each curve in the Monte Carlo Simulation.
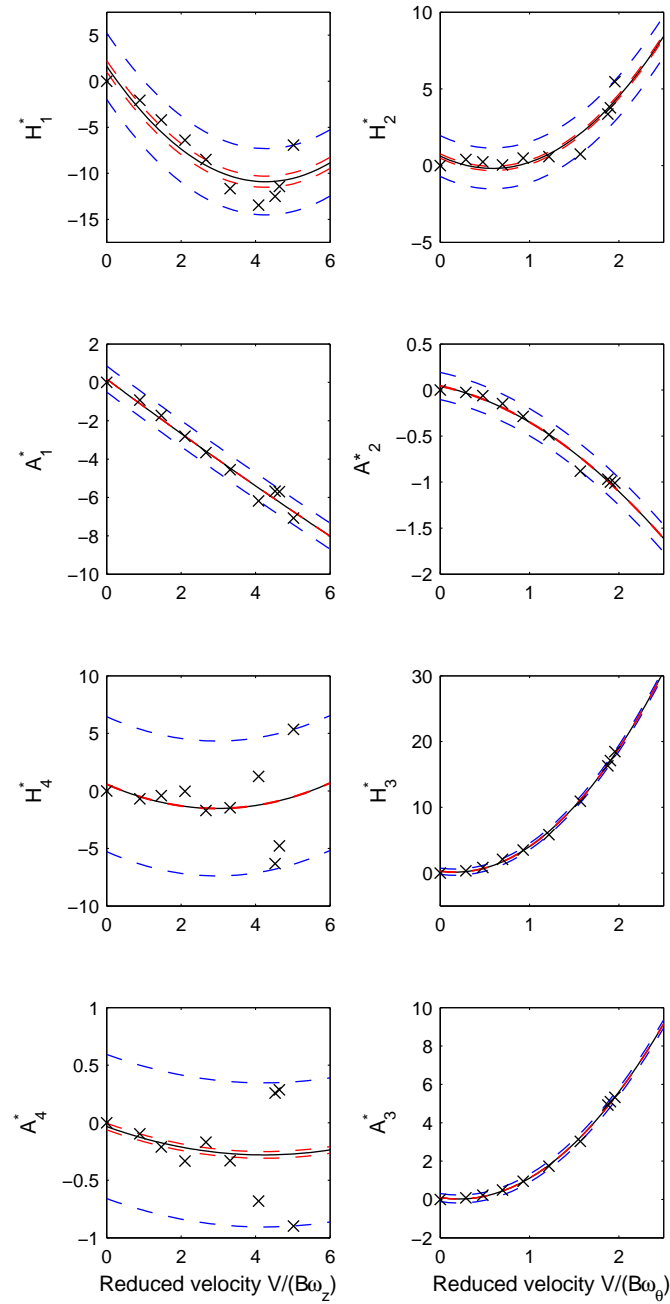
Figure 5.6: Uncertainties in aerodynamic derivatives of the Hålogaland Bridge. Black curve represents the constraint curve fitted to the experimental data, the crosses are the residuals. Red and blue curve marks minimum and maximum value of residuals, respectively.

5.4.2 Parameter uncertainty related to structural damping

The sensitivity analysis performed by Cheng et al. [4] suggests that choice of structural damping ratio has a significant effect on the flutter limit. The structural damping ratio is often a parameter evaluated based on little analytical foundation. Instead, it relies on measurements on prototype structures. For this reason, it is chosen to investigate the sensitivity of the calculated flutter limit of the Hålogaland Bridge with regards to choice of structural damping ratio.

Some structural damping mechanisms of a long-spanned suspension bridge are friction effects at bearings and expansion joints, friction at bolted or riveted construction joints, hysteresis in hangers, material damping and damping provided by the foundation [2]. One of the essential requirements in the design of a suspension bridge is to obtain sufficient flexibility to allow the structure to deform. Hence, structural damping is low, as all joints and bearings are fine-tuned to tolerate a certain amount of bridge movement. For bridges of long spans, structural damping is governed by damping in the material.

The best information of the actual damping ratio is obtained by full-scale measurement on real-life bridges. However, such measurements are difficult and costly. The reliability of the results depends on the accuracy of the measurement method applied. In design of new bridges, generalizations based on available full-scale experimental data should be drawn with caution. Damping is a complex mechanism, and properties such as material, deck type and eigenfrequencies must be taken into account. In Brownjohn [2], the author attempts to rationalize the choice of damping ratio in the design, based on experimental data from real-life suspension bridges. Davenport and Larose [6] suggests a lognormal damping distribution with mean value of 0.40 % of critical. The investigation on structural damping performed in this paper is often referred to in flutter reliability analysis of modern suspension bridges, see e.g. Pourzeynali and Datta [22]. It should be noted that both of the surveys mentioned were performed more or less two decades ago. Thus, the validity of the results in modern bridge design is questionable. Improved construction methods and slender design efficiently reduces the natural damping in the construction. Modern suspension bridges are expected to have far less damping.

More recently, Larsen [17] proposed a linear relationship between the eigenfrequency and damping ratio based on experimental data from the Great Belt Bridge and the Bosporus Bridges. These bridges are stream-lined box section bridges, and can to an extent be expected to have similar properties as the considered Hålogaland Bridge. The proposed empirical relation is given in Eq. 5.5. Inserting the frequency of the fundamental symmetric torsional mode in Hz yields a damping ratio of 0.3 % of critical.

$$\zeta = 0.001 f^{-0.955} \tag{5.5}$$

The design requirements in Handbook 185 specify that the damping ratio should either be measured or supported by acknowledged literature. Further, a damping ratio in the range of 0.5-0.8 % of critical is proposed for steel bridge [26].

To determine the sensitivity of the flutter limit with respect to structural damping, a sufficient wide regime of structural damping ratios should be investigated. This range is not primarily chosen based on direct scientific data. Emphasis is instead made in covering an expected regime of values whereas one could say with a certain degree of confidence that the actual damping ratio will occur. The variation of still-air structural modal damping ratio of the Hålogaland Bridge is modeled as normal distributed, by a mean value and standard deviation. For simplicity, it is assumed that the structural modal damping ratio is equal for all modes. Only linear elastic viscous damping is considered.

Two possible distributions of modal damping ratios are suggested, referred to as Case A and B. Case A is chosen based on the result of Eq. 5.5. A resulting mean value of 0.3 % and standard deviation of 0.07 % of critical is chosen. This represents a normal distribution where a 99.7 % confidence interval covers a range of damping ratios from approximately 0.09 % to 0.51 % of critical.

The damping ratio 0.5 % is often accounted for in literature [2]. Hence, this value is chosen as the mean value of the distribution in Case B. The standard deviation is assumed to 0.1 % of critical. The resulting 99.7 % confidence interval covers a range from 0.2 % to 0.8 % of critical. This represents a wider variation compared to case A, but is a less conservative approach. However, it may be argued that Case B better reflects the amount of uncertainties related to the determination of structural damping.

Chapter 6

Probabilistic flutter analysis

A probabilistic flutter analysis of the Hålogaland Bridge is performed. The proposed probabilistic method in Section 5.2 is implemented in MatLab. Uncertainties of damping and residuals of aerodynamic derivatives, assumed to follow a normal distribution, are obtained by the built-in function `mvnrnd` in Matlab. Based on a given mean value and covariance, presented in Chapter 5, the function generates random variables that follows the respective normal distribution [19].

The simulation of the corresponding flutter limit is obtained by running the function `aerostab.m` in a loop N_{sim} times. For each simulation, the still-air damping matrix $\tilde{\mathbf{C}}_0$ in Eq. 2.22 is built based on the random generated damping ratio. The uncertainties due to scatter in the flutter derivatives is included by generating a new constraint curve to the measurement data for each simulation. This is obtained by adding a random generated residuals to each of the constraint curves of the flutter derivatives.

6.1   Convergence of probabilistic analysis

The number of simulations required for the generated random variables to attain a normal distribution is investigated. In addition to convergence of the input variables, it is important to secure that a sufficient number of simulations N_{sim} is performed to render the correct distribution of the results. Hence, convergence of the proposed probabilistic approach should be verified.

Control of distribution of random generated input variables

The accuracy of the generated variables are tested by computing the mean value and standard deviation of the generated sample of 100, 1000, 10000 and 100000 simulations. The results for damping Case B, is shown in Table 6.1. A second test is performed by plotting generated random variables of damping in a normal probability plot. The result is presented in Figure 6.1.

Number of simulations	Generated mean	Generated standard dev.
$N_{sim} = 100$	0.0051	0.0011
$N_{sim} = 1000$	0.0050	$9.8200 \cdot 10^{-4}$
$N_{sim} = 10000$	0.0050	0.0010
$N_{sim} = 100000$	0.0050	0.0010

Table 6.1: Control of generated random variables from normal distribution of damping with μ=0.5 % and $\sigma = 0.1\%$ of critical.
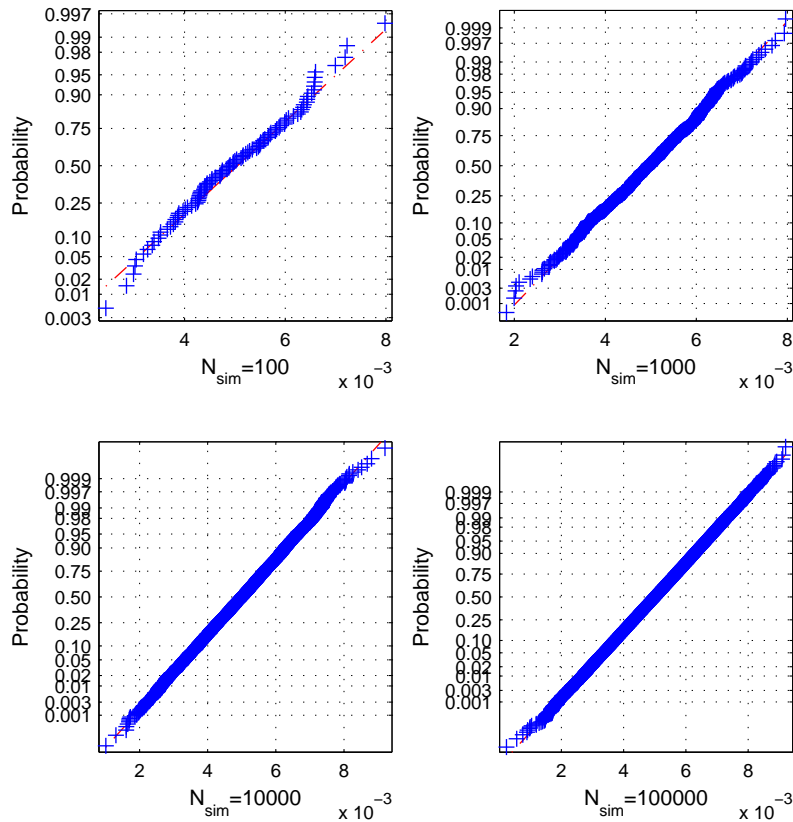

Figure 6.1: Normal probability of generated random variables of normal distributed damping for N_{sim} equal to 100, 1000, 10 000 and 100 000 simulations.

As seen in Table 6.1, the sample mean and sample standard deviation of 1000 represent the mean of 0.5% and standard deviation 0.1% of the assumed normal distribution with good accuracy. A total of 1000 simulations are needed to predict these parameters with four decimals accuracy.

The purpose of the plot in 6.1 is to graphically assess whether the simulated

data follows a normal distribution as assumed. The normal probability plots in Figure 6.1 show that 100 generated variables are insufficient for the data to attain a straight line. The corresponding plot of 1000 generated variables shows higher accuracy, while some disturbance is found in the tails of the distribution. The normal probability plot of 10 000 simulations resembles a straight line with good accuracy. Only insignificant differences are found between the plot of 10 000 and 100 000 generated samples. Hence it is concluded that 10 000 generated variables is sufficient. The same result is found for generation of random variables of damping Case A and residuals of flutter derivatives.

Control of convergence of MCS method.

Control of convergence of the proposed probabilistic approach is performed by evaluating histogram plots of the output variables of the simulations. The distribution of critical mean wind velocity for 1000, 10 000 and 100 000 simulations are presented in Figure 6.2. The choice of a decent bar size of the histogram is vital to correctly represent the data. An adequate number of simulations should be represented in each bar. After some testing, it is found that the round-off number of the square root of number of simulations provides a good number of bars. For 1000, 10 000 and 100 000, the number of bars where chosen to 32, 100 and 316, respectively.

The histogram plot should resemble a clear tendency in the distribution of the results, so that the bar heights can be modeled as a general probability distribution. It is important that the histogram plot is not dominated by individual peaks. As seen in Figure 6.2, N_{sim} equal to 1000 is not sufficient to render a smooth distribution. The result of 10 000 simulations is relatively smooth, with some distinct peaks in the area around the cluster of the simulation results. The distribution of V_{cr} with 100 000 simulations renders a smooth histogram plot.

A second convergence test is performed by evaluating the mean value and standard deviation of the distribution of 1000, 10 000 and 100 000 simulations. The results for the critical mean wind velocity are presented in Table 6.2. The table also indicates the amount of computation time of the MCS.

Number of simulations (N_{sim})	Mean value of V_{cr} (m/s)	Standard dev. of V_{cr} (m/s)	Duration of simulations (h)
1000	69.34	3.36	0.25
10 000	69.24	3.20	3
100 000	69.23	3.21	30

Table 6.2: Convergence of distribution of critical mean wind velocity V_{cr} with number of simulations

As seen in Table 6.2, the analysis with 1000 simulations provides a reasonable accuracy of the mean and standard deviation of the critical mean wind velocity, compared the analysis with higher N_{sim}. The error of the mean and standard deviation of V_{cr} of 10 000 compared to 100 000 simulation is of size 0.01 m/s.

This is an insignificant difference. The same test is performed for the critical oscillation frequency. The results are presented in Table 6.3. The results shows that ω_{cr} may be described with two decimals accuracy for all cases, which is sufficient.

Number of simulations (N_{sim})	Mean value of ω_{cr} (rad/s)	Standard dev. of ω_{cr} (rad/s)	Duration of simulations (h)
1000	2.0191	0.0575	0.25
10 000	2.0204	0.0557	3
100 000	2.0205	0.0552	30

Table 6.3: Convergence of distribution of critical mean wind velocity ω_{cr} with number of simulations

One flutter prediction in the probabilistic analysis took more or less 1 second. Hence, 100 000 simulations needed a simulation time of almost 30 hours. This is undesirable, and it is instead chosen to adapt N_{sim} equal to 10 000 in the proceeding probabilistic flutter analysis, as this renders an adequate smooth distribution of realizations. Hence the resulting critical mean wind velocity can be established with one decimals accuracy, which is deemed sufficient for the considered case.
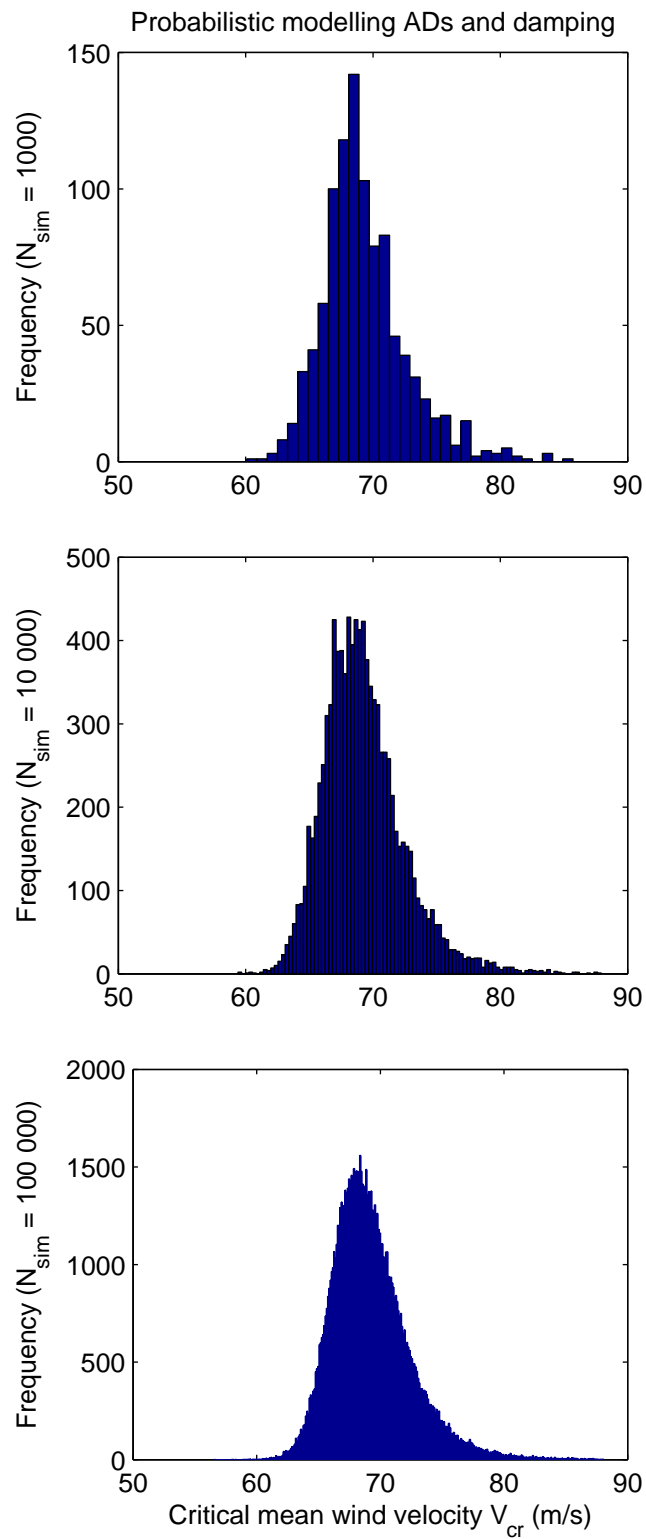
Figure 6.2: Critical mean wind velocity from a probabilistic analysis of 1000, 10 000 and 100 000 simulations.

6.2 Probability distributions of flutter limit

Probabilistic flutter analyses are conducted based on the proposed method and modeling of uncertainties described in Chapter 5. The number of Monte Carlo simulations is 10 000. Histogram plots of the distributions of output variables are presented, where the number of bars is set to 100. Theoretical probability distributions are fitted to the obtained data by utilizing the function `histfit` in the statistical toolbox in Matlab . Further description of this function and other functions applied to generate distribution parameters are found in [19].

The flutter calculation refers to the reference three-mode flutter case, with deterministic critical mean wind velocity of 68.7 m/s and critical oscillation frequency 2.03 rad/s. The constraint curves and residuals of the aerodynamic derivatives refer to Case 2 in Table 5.1. If nothing else is mentioned, all other values are assumed deterministic with a modal damping ratio of 0.5 % of critical. Note that the scale of the axes must be considered to evaluate the output distributions of the probabilistic analyses.

The Monte Carlo simulations yields distribution of critical velocities, critical oscillation frequency and reduced critical velocities. As the design requirement is given in terms of a mean wind velocity of 60.2 m/s, the main focus is given on evaluating the distribution of critical velocities.

6.2.1 Flutter limit sensitivity to uncertainties of flutter derivatives

The sensitivity of the flutter limit due to uncertainties in interpretation of aerodynamic derivatives (ADs) is investigated. The still-air damping ratio is considered deterministic. Uncertainties are modeled as described in Section 5.4.1. The resulting distribution of 10 000 MCS is presented in histogram plots in Figure 6.3, showing distribution of critical mean wind velocity and critical oscillation frequency.

The output distribution of the critical frequencies provided 27 incidents where $\omega_{cr} = 0$. The corresponding critical velocity of these incidents yielded approximately 88 m/s. The probabilistic approach does not take into account other stability limits than flutter; hence, these results do not correspond to any physical stability limit. It is thus suggested that these false instabilities stem from unreasonable modeling of flutter derivatives, resulting in wrong iterations in one of the frequency branches. This assumption is verified by the high values of the residual of H_1^* generated in these incidents. The false instability limits are removed from the sample, as they do not describe a flutter limit. As 27 out of 10 000 is a small number, removing these is not assumed to affect the statistics of the distribution.
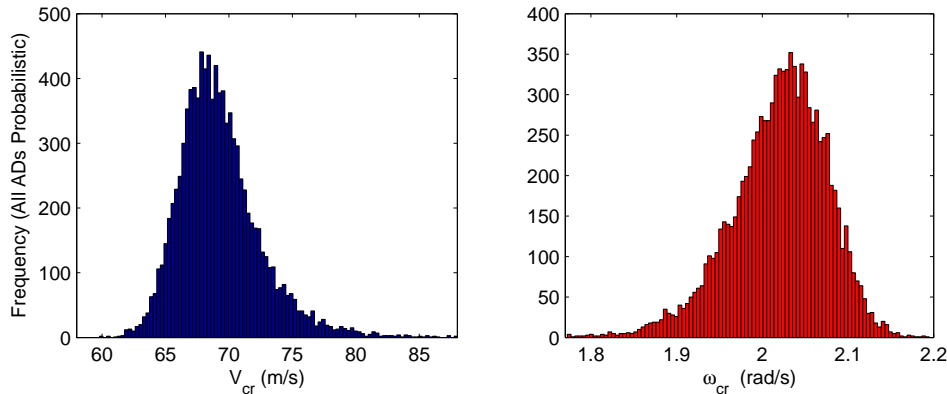
Figure 6.3: Distribution of critical velocity and critical oscillation frequency from probabilistic flutter analysis including parameter uncertainty of aerodynamic derivatives

Figure 6.3 shows that both the histogram of critical velocities and critical frequency have distinctive skew shapes. The distribution of critical mean wind velocities is skewed to the right, while the corresponding distribution of critical oscillation frequency is skewed to the left. This is as expected, as high values of V_{cr} correspond to low values of ω_{cr}.

The cluster of the critical mean wind velocities is located at lower velocities than the mean, skewed to the right. This is not conservative, as the cluster of V_{cr} approaches the design limit of 60.2 m/s. Further, the plot reveals a significant tail behavior on the right side towards high critical velocities. Numerical values describing the tail behavior are found by comparing the maximum and minimum values to the mean of the sample. The mean value of the simulation output of V_{cr} is found to 69.3 m/s, while corresponding simulation output maximum and minimum are found to 88.0 m/s and 59.8 m/s, respectively. The skewness and tail behavior indicates that the distribution of critical mean wind velocity, due to the modeled parameter uncertainty of flutter derivatives, may stem from a type of generalized extreme value (GEV) distribution. Corresponding behavior is observed for ω_{cr}.

To check the validity of the results, it is vital to secure that the obtained flutter limits are in the range of reduced velocities covered by the experimental data from the wind tunnel test. The plots of flutter derivatives measured in the wind tunnel reveal that the highest reduced velocity is $V/B\omega_\theta = 1.95$. A histogram plot of the distribution of critical mean wind velocities is presented in Figure 6.4. The histogram indicates that the majority of the reduced critical velocities are within the range of experimental data, which verifies the obtained results. The plot also indicates that the right tail of the distribution of V_{cr} in Figure 6.3 yields reduced velocities above the experimental data. Hence, the validity of these results are less trustworthy.
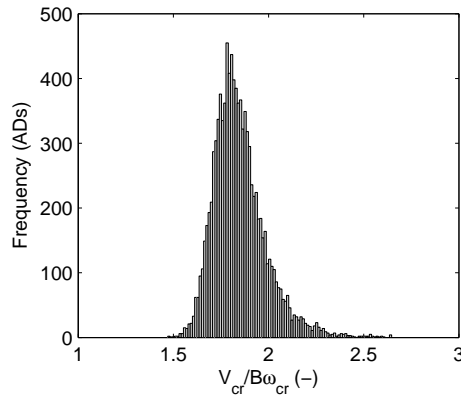
Figure 6.4: Distribution of critical reduced velocity from probabilistic flutter analysis including parameter uncertainty of aerodynamic derivatives

A normal probability plot of the obtained distribution of V_{cr} is given in Figure 6.5a. The cumulative probability distribution (CFD) of a normal distribution attains a straight line, as indicated by the dashed black line. The CFD of a GEV distribution and lognormal (LOGN) distribution fitted to the data are also included as the red and black line, respectively.

(a) Normal probability plot of V_{cr}

(b) PDF fitted to histogram of V_{cr}
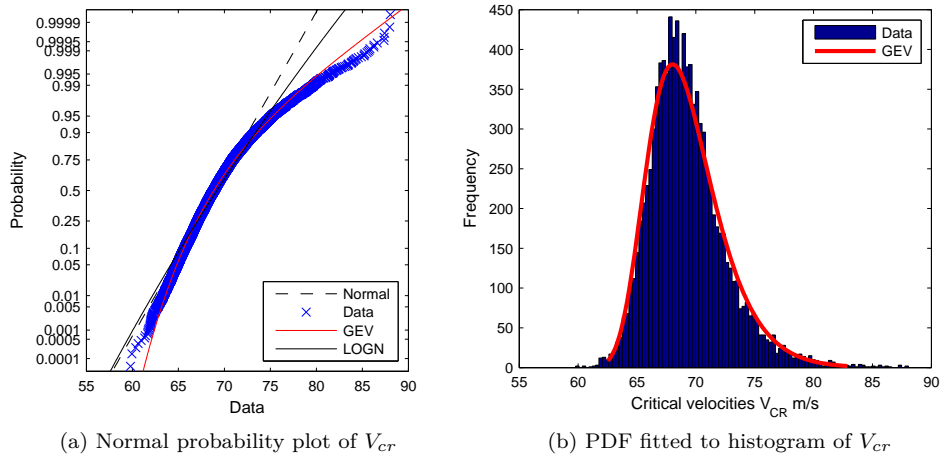
Figure 6.5: Theoretical probability distribution fitted to the distribution of V_{cr} from probabilistic flutter analysis including parameter uncertainties of flutter derivatives shown by a a) normal probability plot and b) histogram plot of the data.

Figure 6.5a verifies that of the three considered distribution families, the GEV distribution gives the best description of the data. A theoretical GEV distribution is fitted to the histogram plot of critical velocities in Figure 6.5b. The parameters of the fitted GEV distribution are obtained by the function `gevfit`

78

in Matlab [19]. The function uses maximum likelihood to estimate the parameters, resulting in

$$k = -0.0539 \;\; \sigma = 2.6934 \;\; \mu = 67.8735$$

The GEV distribution describes a right skewed distribution as the location parameter μ is lower than the estimated mean value of the sample. The shape factor k is negative, yet close to zero, indicating a Gumbel distribution of the data.

The sensitivity of the flutter limit with respect to parameter uncertainty of flutter derivatives may be evaluated by a considering confidence interval of the GEV distribution. This is obtained by the function `gevinv` in Matlab, see [19]. The range of the confidence interval determines the accuracy of established flutter limit. A 95 % confidence interval covers a range of critical velocities from 64.2 m/s to 76.7 m/s. Hence the bound of the confidence interval is relatively close to the design requirement of 60.2 m/s. Obviously, the confidence interval is not symmetric around the mean, as it is based on a skew GEV distribution. However, the probabilistic flutter analysis provides more information of the nature of the flutter limit, than a corresponding deterministic analysis. The large width of the confidence interval indicates that the flutter limit is sensitive to choice of curve approximation of the observed wind tunnel flutter derivatives.

Flutter limit sensitivity to uncertainties of each of the aerodynamic derivatives

It is desirable to gain information about the sensitivity of the flutter limit with respect to parameter uncertainty of each of the respective flutter derivatives. Eight probabilistic analyses are performed, where each of the flutter derivatives in terms are modeled as probabilistic. All other flutter derivatives are assumed deterministic. The resulting distribution of critical velocities and critical oscillation frequencies are presented in Figure 6.6 to 6.8.

It should be noted that the scale of the axes must be taken into account when comparing output sample distributions. A uniform choice of axes would provide an easier comparison. However, probabilistic modeling of each of the flutter derivatives yielded significant differences of scale and width of the output distributions. Hence, the scale of the axes is adjusted to fit each of the output samples, to better evaluate properties such as skewness and tail behavior.

One false stability limit occurred in the simulation with H_1^* as probabilistic variable, where the critical frequency $\omega_{cr} = 0$. Further investigation showed that this incident was a result of a simulation with a high value of the added residual. Hence, a large amount of damping is induced in the system. It is however emphasized that this instability not physically corresponds to static divergence, as only flutter is evaluated. This incident is removed from the output sample. The distribution of ω_{cr} is also seen to have a distinct cut-off tail behavior on the right side..
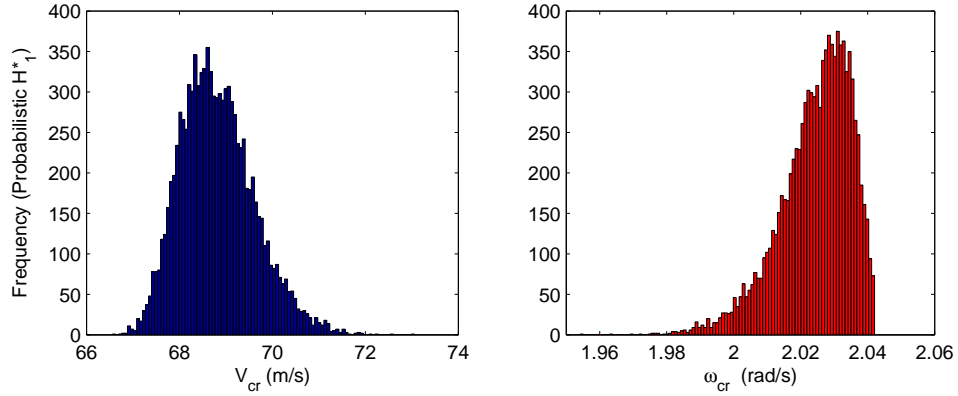
(a) Sensitivity of flutter limit due to parameter uncertainty of H_1^*
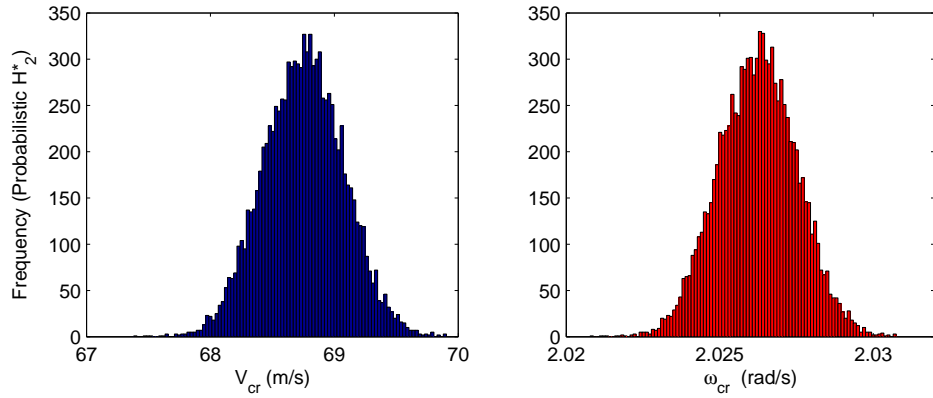
(b) Sensitivity of flutter limit due to parameter uncertainty of H_2^*
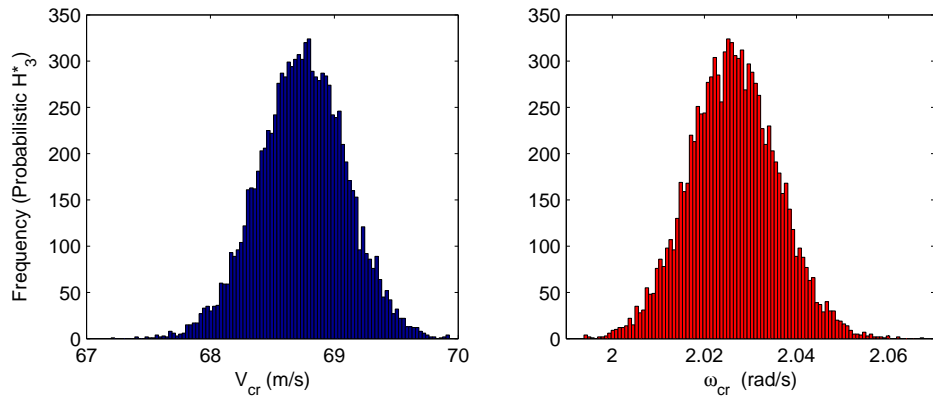
(c) Sensitivity of flutter limit due to parameter uncertainty of H_3^*
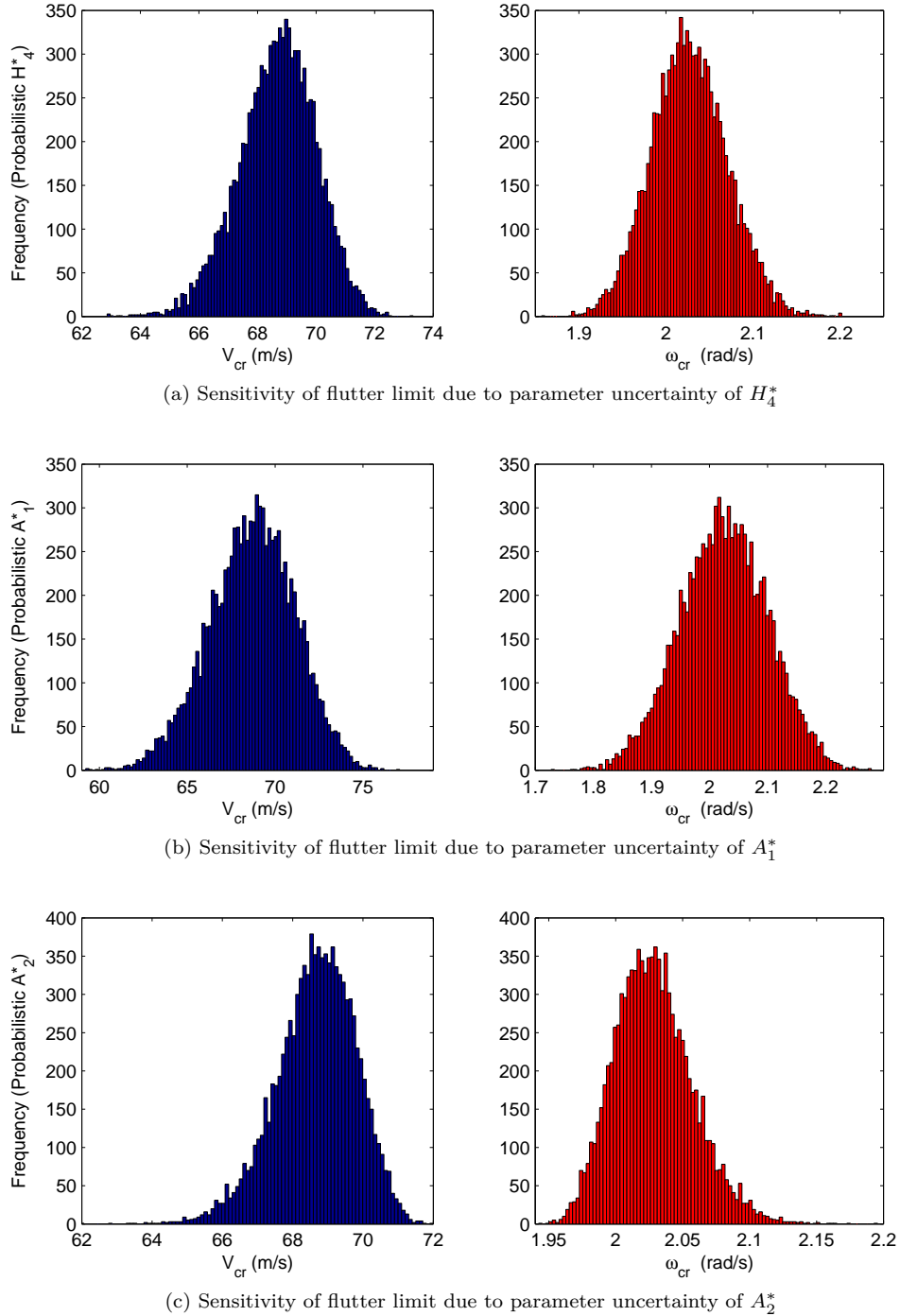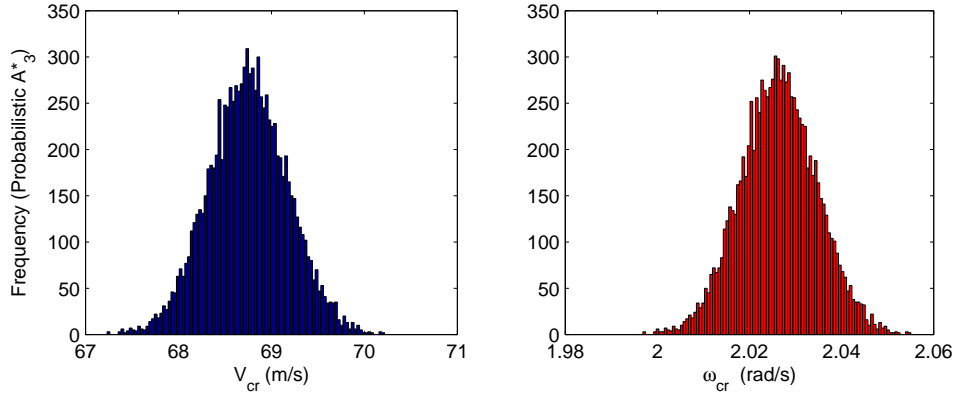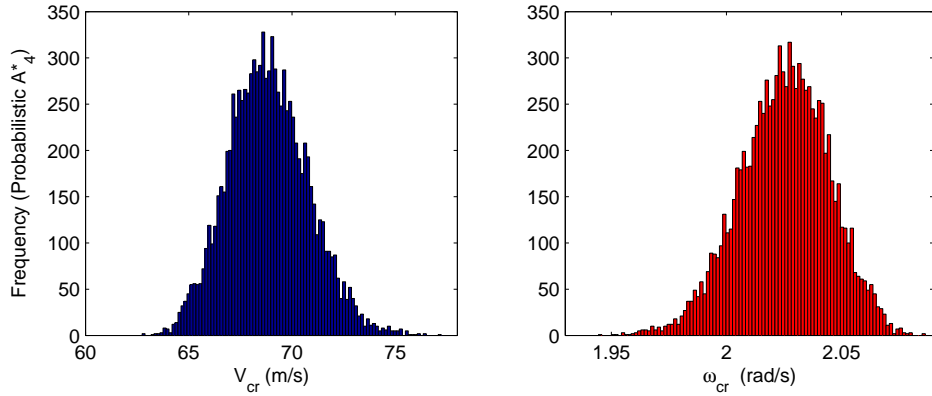
Figure 6.6: Distribution of critical velocity and critical oscillation frequency from probabilistic flutter analysis including parameter uncertainty of aerodynamic derivative a) H_1^*, b) H_2^* and c) H_3^*.

(a) Sensitivity of flutter limit due to parameter uncertainty of H_4^*

(b) Sensitivity of flutter limit due to parameter uncertainty of A_1^*

(c) Sensitivity of flutter limit due to parameter uncertainty of A_2^*

Figure 6.7: Distribution of critical velocity and critical oscillation frequency from probabilistic flutter analysis including parameter uncertainty of aerodynamic derivative a) H_4^*, b) A_1^* and c) A_2^*.

(a) Sensitivity of flutter limit due to parameter uncertainty of A_3^*

(b) Sensitivity of flutter limit due to parameter uncertainty of A_4^*

Figure 6.8: Distribution of critical velocity and critical oscillation frequency from probabilistic flutter analysis including parameter uncertainty of aerodynamic derivative a) A_3^* and b) A_4^*.

The histogram plots in Figure 6.6 to 6.8 show that including uncertainties of each flutter derivative individually provides significant variations in the output distributions, in terms of width, skewness and tail behavior. Figure show that including uncertainty in modelling of flutter derivatives H_1^* or A_4^* yields distinctive right skewed distributions of V_{cr}. These may best be represented by a type of GEV distribution, as suggested in Figure 6.9a. Probabilistic analyses including parameter uncertainty of H_2^*, H_3^* or A_3^* result in narrow distributions, which is seen to resemble a symmetric shape around the mean value of V_{cr}. These distributions may be described by a normal distribution, as suggested in Figure 6.9b.
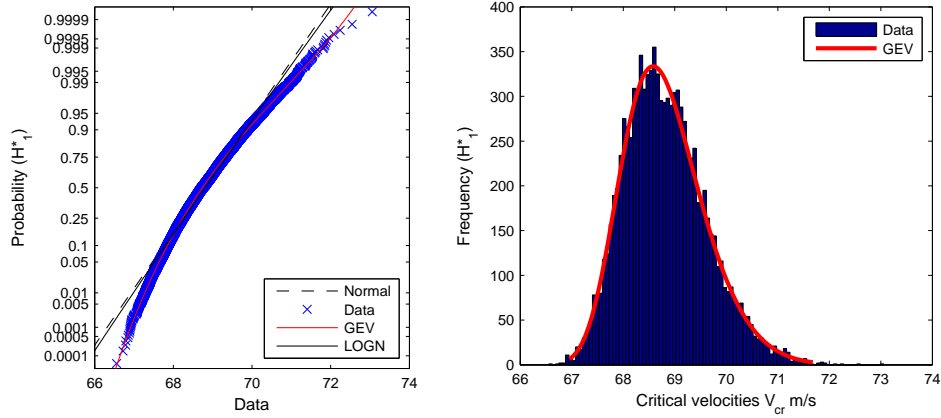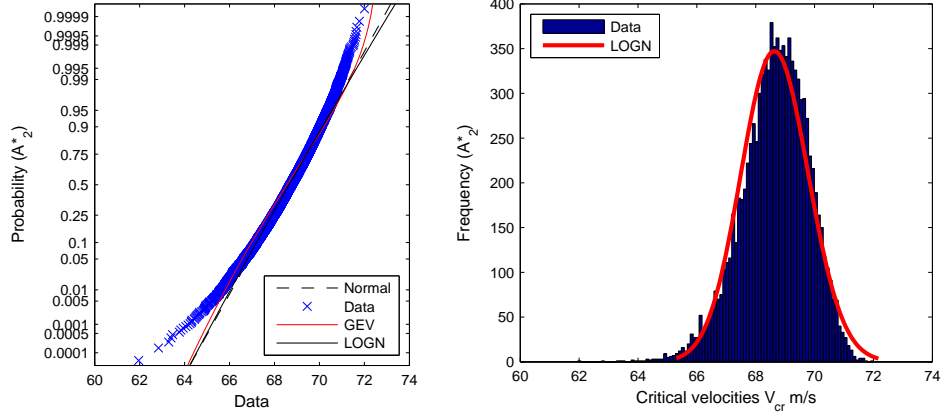
(a) Distribution of V_{cr} due to uncertainty of H_1^*, fitted to GEV distribution
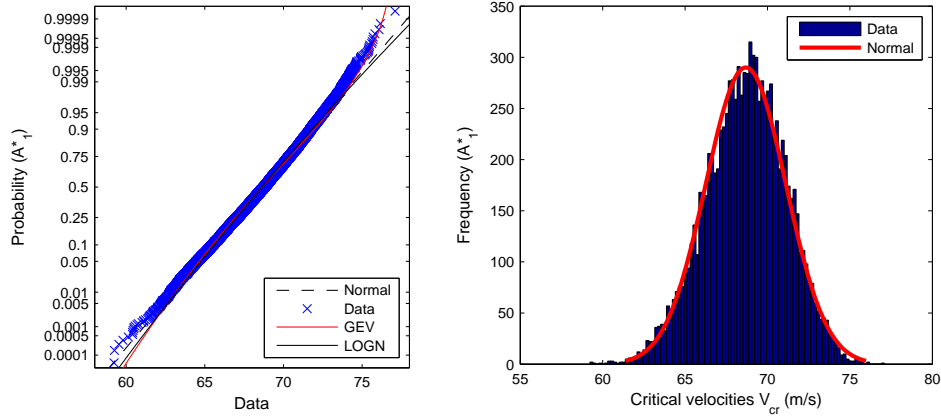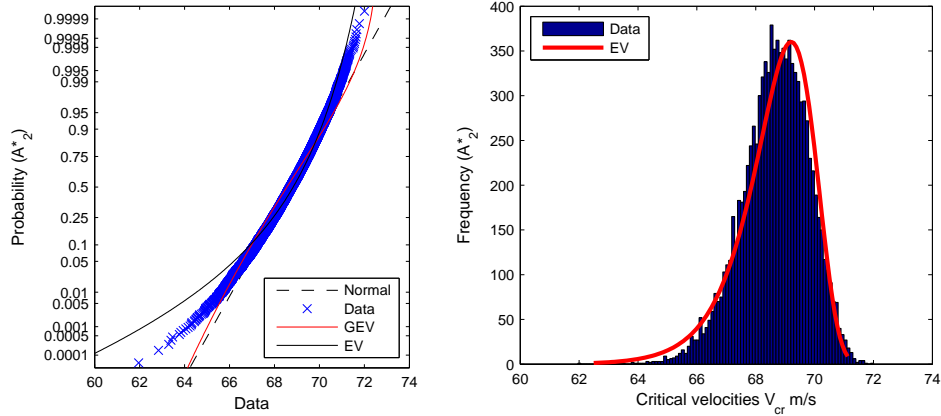

(b) Distribution of V_{cr} due to uncertainty of A_1^*, fitted to normal distribution

Figure 6.9: Theoretical probability distribution fitted to the distribution of V_{cr} from a probabilistic flutter analysis including parameter uncertainties of a) H_1^* and b) A_1^* shown by a normal probability plot and histogram plot of the data.

Including uncertainty of flutter derivatives H_4^* and A_2^* indicates left skewed distributions of V_{cr}. It should however be emphasized that the suggested theoretical distributions do not describe the underlying distribution fully. This is illustrated in Figure 6.10, where neither a normal distribution, nor an extreme value distribution (EV) provides an accurate fit in all regions. The normal distribution underestimate the bars in the left tail, while the EV distribution overestimate these. The histogram plots in Figure 6.6 to 6.8 further suggest that the amount of skewness in the output variable is related to the width of the distribution, hence the amount of uncertainty related to the respective flutter derivative. Simliar conclusions can be drawn with regards to distributions of critical frequency.

(a) Distribution of V_{cr} due to uncertainty of A_2^*, fitted to lognormal distribution

(b) Distribution of V_{cr} due to uncertainty of A_2^*, fitted to EV distribution

Figure 6.10: Theoretical probability distribution fitted to the distribution of V_{cr} from a probabilistic flutter analysis including parameter uncertainties of A_2^* shown by a normal probability plot and histogram plot of the data fitted to a a) Lognormal distribution b) EV distribution.

As illustrated in Figure 6.9 and 6.10, the distribution of output variables are not necessarily normal distributed. Hence, only considering the mean values and standard deviations do not fully describe the distributions. However, these parameters provide an important tool for assessing the sensitivity of the flutter limit due to uncertainties provided by each flutter derivative, by comparing the output samples width and location. The mean value and standard deviation corresponding to an assumed normal distribution of the different output samples are presented in Figure 6.11. The numerical values of the bar diagram and corresponding values for the critical oscillation frequency are given in Appendix C, Table C.1 and C.2, respectively. Figure 6.11a shows that the mean values of the obtained distributions of V_{cr} are close to the deterministic value of 68.7 m/s. The same results are found for ω_{cr}. This indicates that the mean value is

not sensitive to uncertainties due to scatter of wind tunnel measurements.

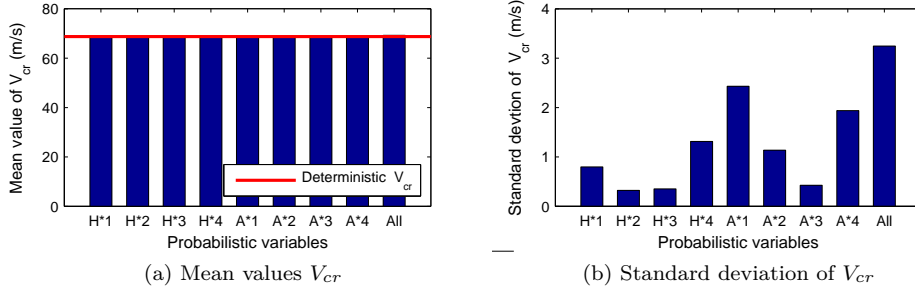(a) Mean values V_{cr} (b) Standard deviation of V_{cr}

Figure 6.11: Distribution of V_{cr} from probabilistic analysis by including parameter uncertainty of each aerodynamic derivative, given by the a) mean value and b) standrad deviation of an assumed normal distribution of the results. The red line in a) marks the deterministic value of the flutter limit.

The standard deviations presented in Figure 6.11b indicate the flutter limit sensitivity to the modeled uncertainty if the output samples were normal distributed. From the central difference theorem, it is stated that the variance of the sum of two normal distributions are given by the sum of the respective variance of each distribution. Hence, if the output samples in Figure 6.6 to 6.8 indeed were normal distributed, the variance of the probabilistic analysis with all derivatives as probabilistic variables would be given by the sum of the variance from the probabilistic analysis of each flutter derivative, individually. Adding the variances represented in each bar in Figure 6.11b, yields a resulting total standard deviation of 3.7 m/s. This is a relatively good estimate of the standard deviation of 3.2 m/s found by including uncertainties of all ADs, shown by the right bar in Figure 6.11b. Hence, it may be suggested that the relative bar sizes provides an estimate of the amount of uncertainty related to the respective derivative. However, when evaluating uncertainties induced by each flutter derivative, it is important to consider that their relative magnitude is a function of two factors, namely

- The importance of the respective flutter derivative
- Scatter in measurement of the respective flutter derivative, represented by the magnitude of its residuals

The bar diagram in Figure 6.11b indicates that the largest standard deviation is obtained when including parameter uncertainty of A_1^*. Hence, the flutter limit is sensitive to scatter in the measured data set of A_1^*. Regarding the plot of the wind tunnel data and residuals in Figure 5.6, the residual band of A_1^* is seen to be relatively narrow. The development of flutter instability is dominated by the behavior of aerodynamic derivatives A_1^*, A_2^*, A_3^*, H_3^* and to some extent H_1^* [7]. The results of the probabilistic analysis reveal that accurate modeling of these derivatives is vital for the accuracy of the results.

Flutter derivatives H_4^* and A_4^* describe aerodynamic stiffness induced by the vertical position of the deck, and are considered to have little impact on the

flutter limit. However, the bar diagram in Figure 6.11b show that both H_4^* and A_4^* provide high standard deviations, and thus significant contributions to the overall uncertainty of the flutter limit. This is a result of the high amount of scatter in the measurement of these derivatives, as indicated by the large area covered by the residuals bounds in Figure 5.6.

The high standard deviations of H_4^* and A_4^* indicate that the large scatter in the measurement of these has an undesirable effect in the probabilistic flutter predictions. It should thus be questioned whether including this scatter as an uncertainty provides a wrong modeling of the physical problem. A second probabilistic analysis is conducted by excluding the effect of scatter in H_4^* and A_4^*. These are modeled as deterministic variables, while uncertainties of all other flutter derivatives are included. The resulting distributions of critical mean wind velocity and critical frequency are shown in Figure 6.12.
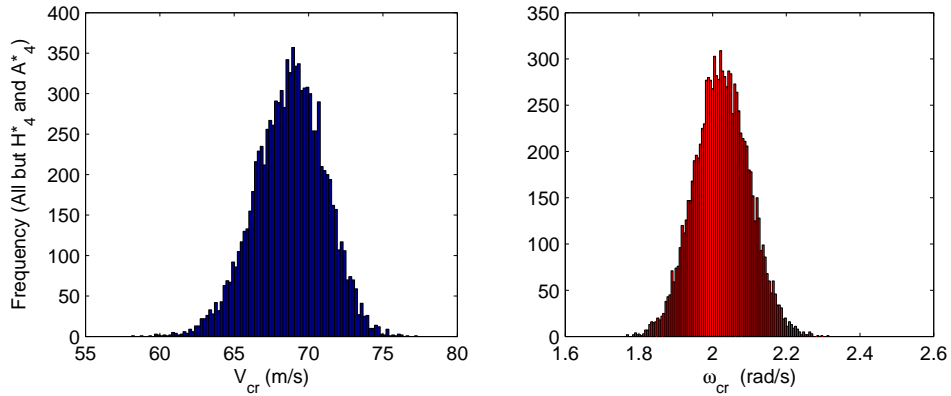

Figure 6.12: Distribution of critical velocity and critical oscillation frequency from probabilistic flutter analysis including parameter uncertainty of all aerodynamic derivatives except from H_4^* and A_4^*, which are modeled as deterministic.

Figure 6.12 shows that excluding parameter uncertainty of H_4^* and A_4^* reduce the width of the distribution of critical velocity considerably, compared to the when they are included (Figure 6.3). The histogram plots in Figure 6.12 further indicate that the amount of skewness is reduced. By plotting the distribution of V_{cr} in a normal probability plot, it is seen that a normal distribution may be used to describe the data. This is illustrated in Figure 6.13a. The effect of excluding the uncertainty due to large scatter in measurement of H_4^* and A_4^* is seen in Figure 6.13b, where a normal distribution is fitted to the data. The theoretical distributions of the probabilistic analysis including scatter of all flutter derivatives is indicated as the black dashed line. To compare the results, the suggested normal distribution of V_{cr} when excluding uncertainties of H_4^* and A_4^* provides a standard deviation of 2.3 m/s, resulting in a 95 % confidence interval spanning from 63.1 m/s to 72.3 m/s. This indicates that the scatter in the measurement of H_4^* and A_4^* has a significant influence on the amount of uncertainty in the prediction of the flutter limit.

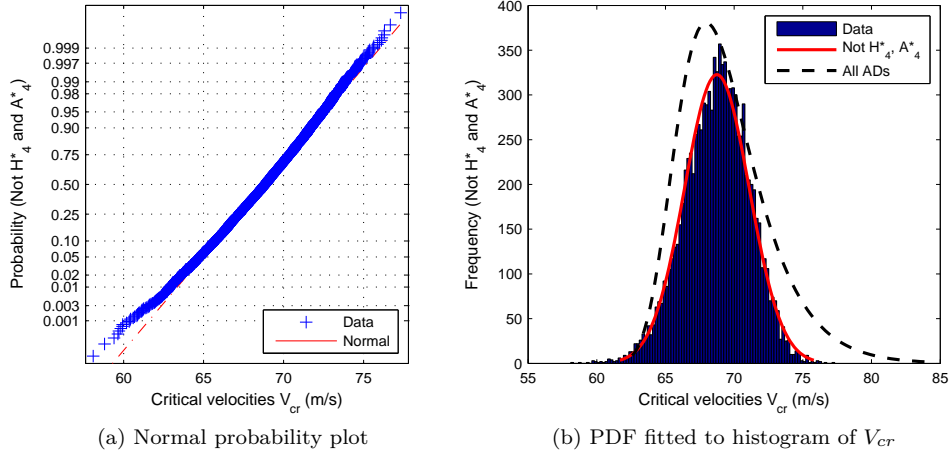(a) Normal probability plot

(b) PDF fitted to histogram of V_{cr}

Figure 6.13: Theoretical probability distribution fitted to the distribution of V_{cr} from probabilistic flutter analysis including parameter uncertainties of all flutter derivatives except from H_4^* and A_4^* presented in a) Normal probability plot and b) Histogram plot of the data. The dashed black line in b) indicate the PDF fitted to the data from the flutter analysis where uncertainty of all ADs are included.

Effect of large scatter at high reduced velocities in the wind tunnel

As seen in the plot of constraint curves and residuals in Figure 5.6, it is in general the last three observations that provide the upper limits of the residuals, indicated by the blue lines. The wind tunnel report shows that the system damping approaches zero for the reduced velocities of the last three observations, and hence the accuracy of these data points are questionable [8]. A disadvantage of the proposed probabilistic modeling of aerodynamic derivative is that the large uncertainties with respect to the three last observations, are introduced at all velocities. This is the case as the normal distributions of the residuals is given by the covariance calculated based on all ten observations, as shown by the covariance matrix in Table 5.3.

To evaluate the effect of the uncertainty provided by the three last observations, a new probabilistic flutter analysis is performed based on aerodynamic derivatives of "Case 3" in Section 5.4.1. The Case 3 constraint curves are fitted to the 6 first observations in the wind tunnel, where the wind tunnel model is assumed stable. The residuals of the Case 3 constraint curves and corresponding covariance matrix are given in Appendix B, Table B.7 and B.8, respectively. A plot of the constraint curves of Case 3 with residuals are given in Appendix B Figure B.1. The upper and lower bounds of residuals are seen to provide significantly narrower areas than the corresponding modeling when considering all data points, in Figure 5.6. Hence, this modelling of flutter derivatives includes less uncertainty in the flutter prediction. The obtained output samples from a probabilistic flutter analysis applying the Case 3 modelling of uncertainties of flutter derivatives are given in Figure 6.14.
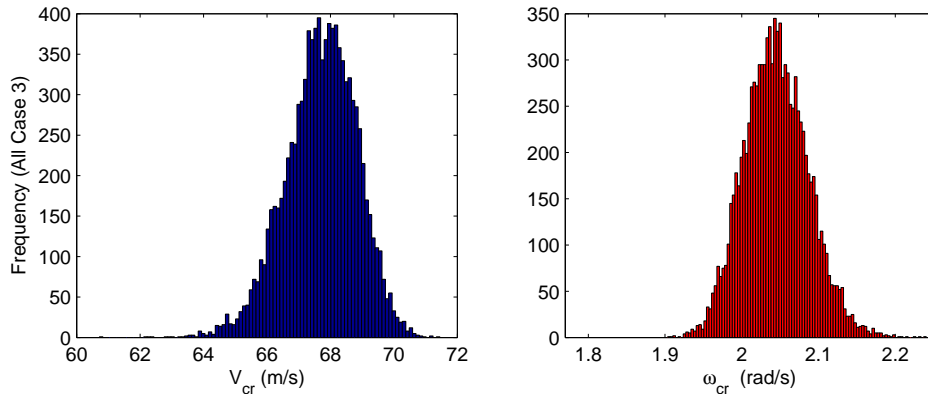
Figure 6.14: Distribution of critical velocity and critical oscillation frequency from probabilistic flutter analysis including parameter uncertainty of aerodynamic derivatives described by Case 3 of Table 5.1

Comparing the result of Figure 6.14 with the distributions based on all wind tunnel observations in 6.3, it is important to remember that the two analyses are based on different initial constraint curves. These provide different deterministic flutter limits, as indicated in Table 5.2. The probabilistic flutter analysis including parameter uncertainty of all observations of aerodynamic derivatives should be compared to "Case 2" in Table 5.2. Hence, the magnitude of the mean values of the distributions cannot be compared directly.

The width of the distributions in Figure 6.14 are severely reduced compared to Figure 6.3, indicating that the uncertainty of the established flutter limit is decreased. The distributions in Figure 6.14, are also seen to be less skew. The obtained distribution of V_{cr} of Case 3 is plotted in a probability plot in Figure 6.15a. The plot indicates that the data may be described by a normal probability distribution. This is verified by fitting a normal PDF to the histogram of V_{cr} in Figure 6.15b. A 95 % confidence interval of the suggested normal distribution covers a range of critical velocities from 65.5 m/s to 70.0 m/s.

The dashed black line in in Figure 6.15 indicate the GEV distribution describing the results of the probabilistic analysis when all wind tunnel observations are included (Case 2). The comparisons of the two ways of modeling aerodynamic derivatives shown indicate that the uncertainty is severely reduced by excluding the three last measurements in the wind tunnel. However, it should be noted that when excluding the three last observations in the wind tunnel, the range of reduced velocities of the experimental data series is limited to a maximum value of $(V/B\omega_\theta)_{max} = 1.57$. A plot of the obtained critical reduced velocities of the distribution reveals that the main part of the simulations yields flutter limits outside the range of the experimental data. The values of the flutter derivatives are instead based on extrapolated behavior. This reduces the validity of the obtained distributions.
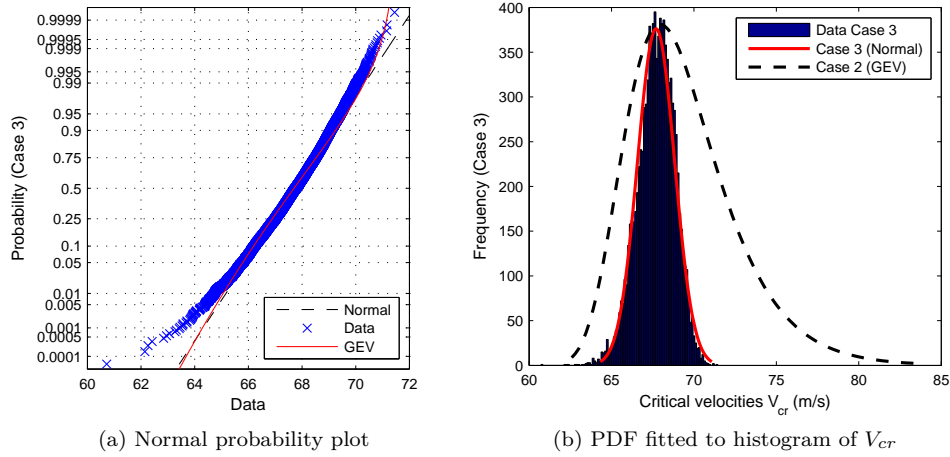
(a) Normal probability plot   (b) PDF fitted to histogram of V_{cr}

Figure 6.15: Theoretical probability distribution fitted to the distribution of V_{cr} from probabilistic flutter analysis including parameter uncertainties of flutter derivatives modeled by Case 3, presented in a a) Normal probability plot and b) Histogram plot of the data. The dashed black line in b) indicate the PDF fitted to the data from the flutter analysis based on Case 2.
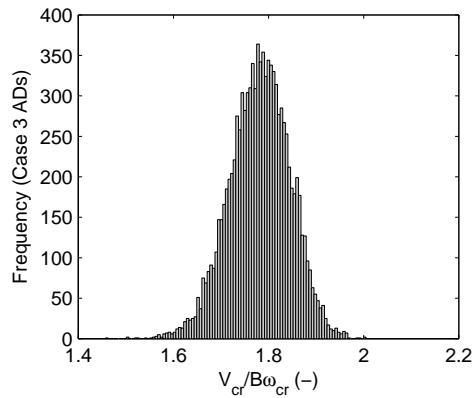

Figure 6.16: Distribution of reduced critical velocities from probabilistic flutter analysis by including parameter uncertainty of aerodynamic derivatives of Case 3.

These results show the importance of covering a sufficiently large reduced velocity regime in the wind tunnel experiment. Again, it is emphasized that having the stability limit of the wind tunnel model in the range of the experimental data is unfortunate, as it severely increases the amount of scatter in the data series of aerodynamic derivatives. This increases the uncertainties arising due to different interpretations of the wind tunnel results. Hence, the accuracy of which the flutter limit may be determined is reduced.

The two cases of interpreting wind tunnel data, by including all observations in Case 2 or excluding the three last in Case 3, provides a good example of the value of a probabilistic analysis. The accuracy of the determined limit of Case 2 is severely reduced compared to Case 3, as Case 3 assumes less uncertainties. This is reflected by the increased width of the 95 % confidence intervals, given by [64.2 m/s, 76.7 m/s] for Case 2 and [65.5 m/s, 70.0 m/s] for Case 3. The corresponding deterministic flutter analysis of these two cases yields insignificant differences in critical velocity, by 68.7 m/s and 67.7 m/s, respectively. These results illustrate how much more information a probabilistic flutter analysis provides, compared to a corresponding deterministic analysis.

Effect of covariance

The effect of the modeled dependence between the uncertainty of the flutter derivatives is investigated. This is performed by evaluating the effect of the covariance of the residuals. A probabilistic analysis is performed by excluding the covariance of the residuals, by setting the off-diagonal terms equal to zero in the covariance matrix in Table 5.3. Hence, the uncertainties in the experimental series of one flutter derivative are assumed independent of the other series. The resulting distribution of critical mean wind velocity and critical oscillation frequency is shown in Figure 6.17.
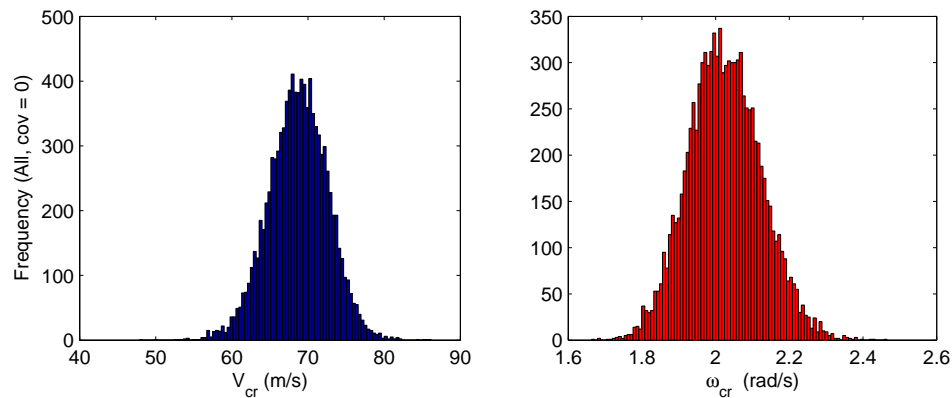

Figure 6.17: Distribution of critical velocity and critical oscillation frequency from probabilistic flutter analysis by modeling the parameter uncertainty of the aerodynamic derivatives as independent. (COV=0) .

Figure 6.18 shows that the tail behavior and skewness of the distribution of critical velocities when the uncertainties are assumed independent are considerably reduced, compared to the results where the covariance is included, given in Figure 6.3. The histogram plot of V_{cr} in Figure 6.17 are instead seen to yield a symmetric shape around the mean value, indicating that the data may be described by a normal distribution. Further, the distribution of V_{cr} provides a wider distribution when excluding the covariance, indicating decreased accuracy of the established flutter limit.

A probability plot of the data in Figure 6.18a shows that the distribution of V_{cr} may be fitted to a normal distribution, with mean value 68.7 m/s and standard deviation 3.9 m/s. This distribution is plotted together with the histogram of V_{cr} in Figure 6.18b, and yields a 95 % confidence interval gives a critical velocities from 60.9 m/s to 76.5 m/s. The standard deviation obtained when modeling each of the aerodynamic derivatives independently and adding the variances, was found to found to 3.7 m/s. This indicates that the individual distributions in Figure 6.6 to 6.8 are approximately normal distributed.

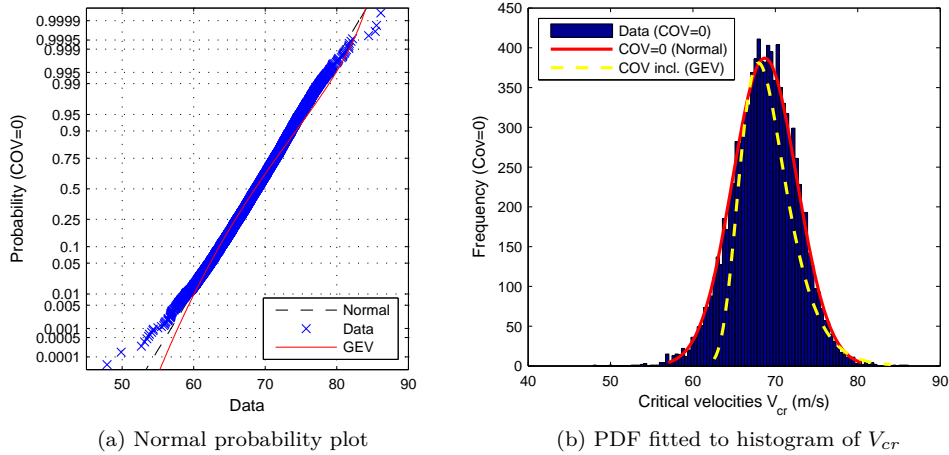(a) Normal probability plot   (b) PDF fitted to histogram of V_{cr}

Figure 6.18: Theoretical probability distribution fitted to the distribution of V_{cr} from probabilistic flutter analysis by modeling the parameter uncertainty of the aerodynamic derivatives as independent. (COV=0) presented in a a) Normal probability plot and b) Histogram plot of the data. The dashed yellow line in b) indicate the PDF fitted to the data from the flutter including covariance..

Including dependence between the measured aerodynamic derivatives reduces the output standard deviation to 3.2 m/s. The theoretical GEV distribution fitted to the distribution of V_{cr} where the covariance is included is indicated by the dashed yellow line in Figure 6.18b. Modelling uncertainties related to each of the flutter derivatives as dependent of the others is seen to decrease the confidence interval of critical velocities.

6.2.2 Flutter limit sensitivity to uncertainties in structural damping

Probabilistic flutter analyses including parameter uncertainty of structural damping ratio are performed. Two proposed damping models, Case A and Case B, are considered, as described in Section 5.4.2. All other parameters are assumed deterministic. Histogram plots of the resulting distributions of critical velocities and critical oscillation frequencies are given in Figure 6.19. The mean value and standard deviation of the assumed normal distributions of structural damping ratio of Case A and Case B are indicated as μ and σ, respectively.

(a) Case A (μ=0.3 % and $\sigma = 0.07\%$ of critical)

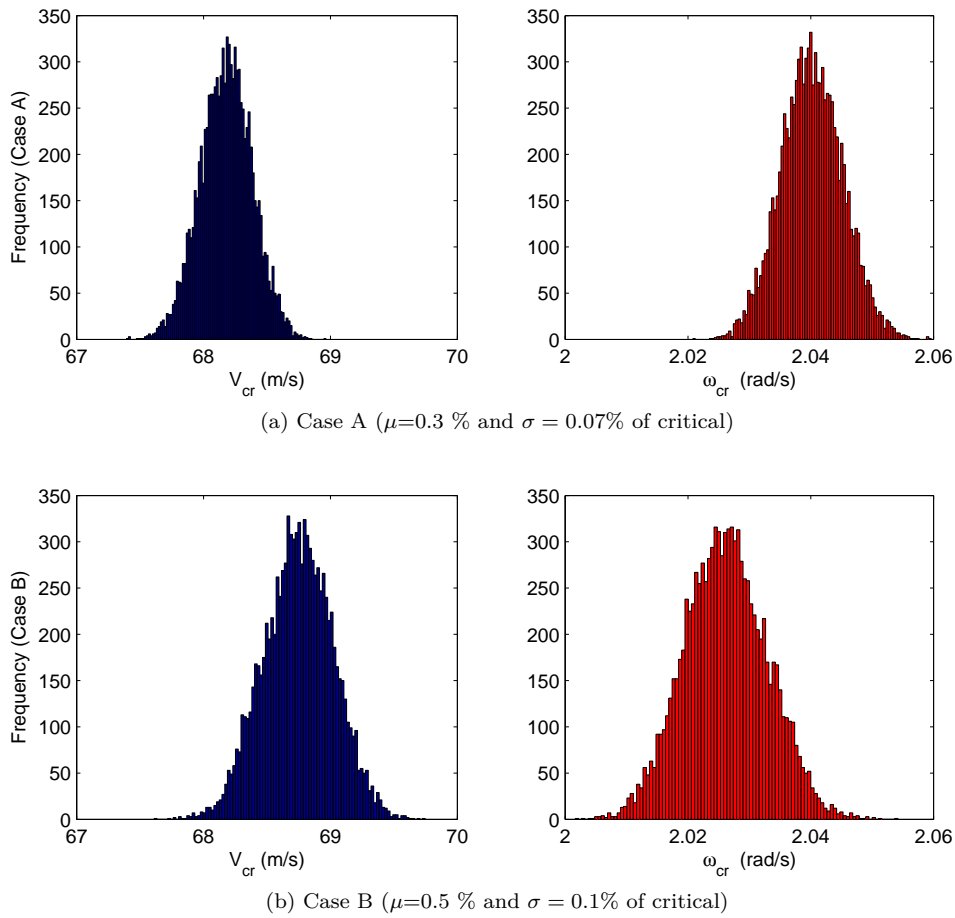(b) Case B (μ=0.5 % and $\sigma = 0.1\%$ of critical)

Figure 6.19: Distribution of critical velocity and critical oscillation frequency from probabilistic flutter analysis including parameter uncertainty of damping by a) Case A and b) Case B

As expected, Case A provides a more conservative distribution of V_{cr} than Case B, as structural damping is lower. The mean and standard deviations of the distributions of critical velocity are presented in Figure 6.20. The numerical values and corresponding results for the critical oscillation frequency are given

in Appendix C, in Table C.4 and C.5. When comparing the probabilistic and deterministic flutter analysis it should be noted that the deterministic flutter analysis assumed a damping ratio of 0.5 % of critical, corresponding to the mean value of the modeled damping ratio in Case B. The bar diagram in Figure 6.20a show that the mean values of the distribution of V_{cr} are not affected by uncertainties of structural damping ratio. Similar results are found for the mean values of the critical oscillation frequency.
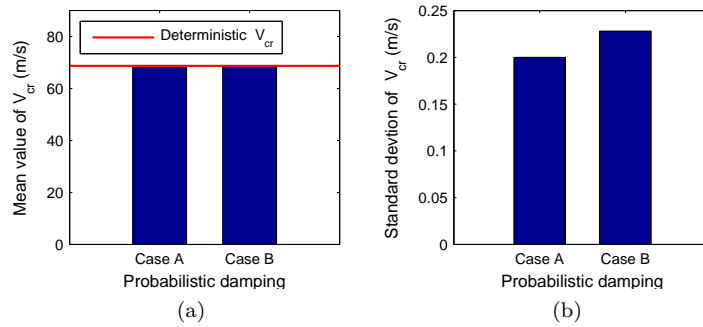

Figure 6.20: Sensitivity of critical mean wind velocity to damping by modeled uncertainty of Case A and B, evaluated by the a) mean value and b) standard deviation of the simulations.

The magnitude of the standard deviation, as given in Figure 6.20b, indicates that the sensitivity of the flutter limit with regards to structural damping is low. As expected, the Case B damping provides a wider distribution of critical mean wind velocity than Case A. The shape of the histograms also indicate that the probability distribution of V_{cr} and ω_{cr} shown in Figure 6.19 is normal distributed. This is verified by plotting the distribution of critical velocities in normal probability plot, as shown for Case B in Figure 6.21a.

Regarding the plot of the development of in-wind damping ratio in Figure 4.3 in Chapter 4, it is seen that the slope of the damping curve on the torsional branch decrease approximately linearly near the flutter limit. An increase in structural damping ratio of 0.1 % constitutes of moving the x-axis downwards with same magnitude. This provides a linear relation between the output variable, the flutter limit, and the input variable, the structural damping ratio. Hence, the central limit theorem states that the output distribution also will follow a normal distribution. This is verified in Figure 6.21, where a normal probability distribution is fitted to the distribution of V_{cr} of damping Case B. The same results are found for the critical oscillation frequency.

By modeling uncertainties in damping according to Case B, a 95 % confidence interval of the normal distribution of V_{cr} span velocities from 68.2 m/s to 69.4 m/s. This is an insignificant variation. Hence, it can be concluded that the sensitivity of the flutter limit with respect to choice of structural damping ratio is low.
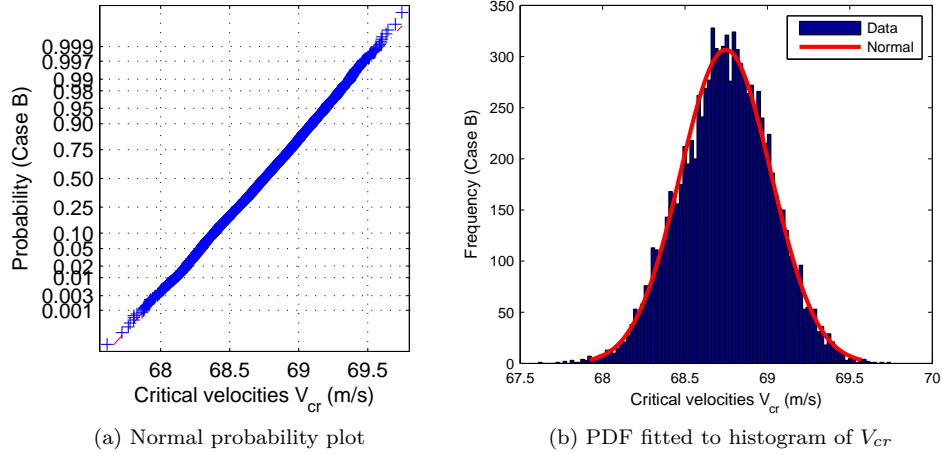
(a) Normal probability plot

(b) PDF fitted to histogram of V_{cr}

Figure 6.21: Theoretical probability distribution fitted to the distribution of V_{cr} from probabilistic flutter analysis including parameter uncertainties of damping Case B presented by a a) Normal probability plot and b) Histogram plot of the data.

6.2.3 Flutter limit sensitivity to parameter uncertainty of flutter derivatives and damping

Finally, a probabilistic flutter analysis including parameter uncertainty of both flutter derivatives and damping ratio is considered. The parameter uncertainty of damping is modeled according to Case B in Section 5.4.2. The resulting distributions of V_{cr} and ω_{cr} are shown in Figure 6.22.
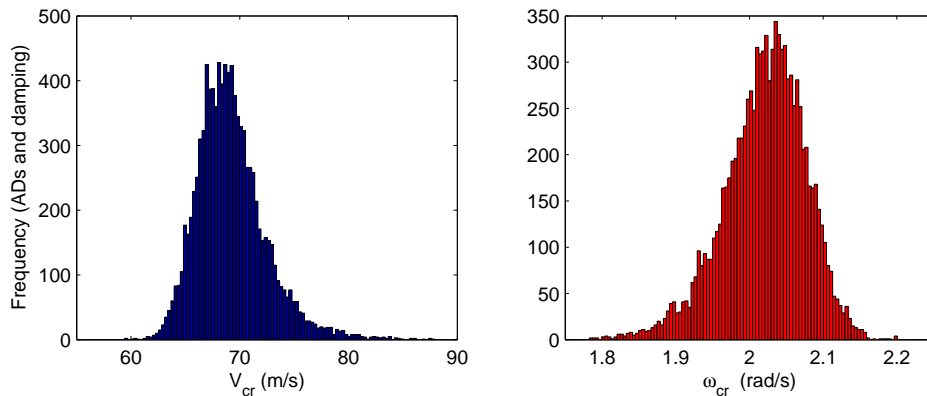

Figure 6.22: Distribution of critical velocity and critical oscillation frequency from probabilistic flutter analysis including parameter uncertainty of aerodynamic derivatives and structural damping ratio.

Considering the result of Section 6.2.2, the sensitivity of the flutter limit with

respect to parameter uncertainty of damping is low. The histogram plots resembles the shapes of the distributions in Figure 6.3, when only parameter uncertainty of the flutter derivatives are considered. Hence, the distributions may be described by types of extreme value distributions. The distribution of V_{cr} is described by GEV distribution with shape parameter μ of 67.9 m/s, scale parameter σ of 2.7 m/s and shape parameter k of -0.06. The distribution of ω_{cr} is left-skewed, and is described by an extreme value distribution with location parameter μ of 2.05 rad/s and scale parameter σ of 0.05 rad/s. The suggested distributions are illustrated in Figure 6.23.
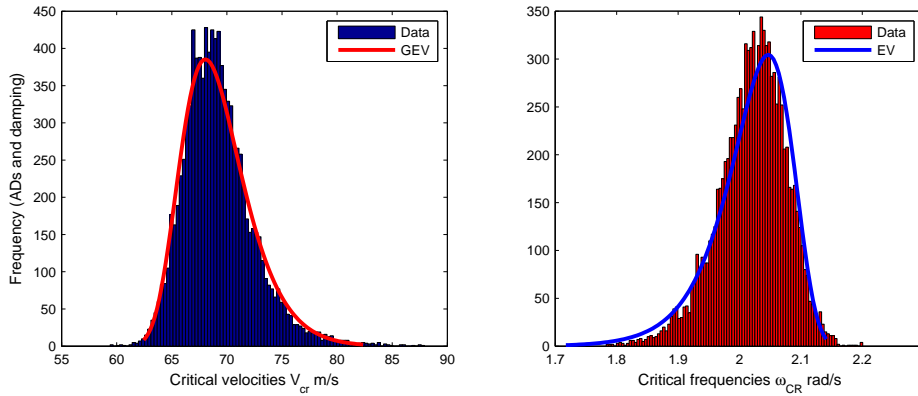

Figure 6.23: Theoretical probability distributions fitted to the distributions of V_{cr} and ω_{cr} from probabilistic flutter analysis including parameter uncertainty of flutter derivatives and structural damping ratio.

Based on the suggested GEV distribution, confidence intervals of V_{cr} may be established. A 95 % confidence interval ranges from 64.2 m/s to 77.7 m/s. The corresponding 99 % confidence interval ranges from 63.5 m/s to 78.6 m/s. Hence, the width of the confidence intervals are 12.3 m/s and 15.1 m/s, respectively. Obviously, the confidence intervals are not symmetric around the mean values of the distributions. Still, their width indicate the level of accuracy of which the flutter limit may be determined. The results show that the flutter limit is sensitive with respect to the modeled parameter uncertainty.

Chapter 7

Conclusion

The work presented in this report is a study of the aeroelastic stability of the Hålogaland Bridge. The state-of-the-art theory concerning determining flutter limits in modern bridge design is presented. The flutter equations are implemented in Matlab in the code `aerostab.m` developed at NTNU.

The bimodal flutter limits for all relevant combinations of still-air vibration modes are evaluated based on mode shape similarity and frequency separation. Coupling of the fundamental symmetric torsional mode and fundamental symmetric vertical mode yielded a flutter limit of 77.9 m/s, while coupling with the second symmetric vertical mode yielded 73.8 m/s. The second symmetric mode showed higher mode shape similarity with the torsion mode than the fundamental. In addition, their frequency ratios are 1/2 and 1/3, respectively. Hence, the second mode is most likely to couple in bimodal flutter. The dynamic test rig in the wind tunnel is adjusted to reproduce the frequency of the first symmetric vertical mode. To obtain a more conservative measurement of the stability limit of the section model, the dynamic rig should instead be tuned to resemble the second vertical mode.

Several of the mode pairs considered yielded reduced critical velocities outside the range of the experimental data in the wind tunnel test. This reduces the validity of these flutter predictions, as the aerodynamic derivatives at the flutter limit must be based on extrapolated behavior. The short range of reduced velocities is a result of using the same dynamic test rig to measure the stability limit of the section model. Having the stability limit at the end of the data series of aerodynamic derivatives is unfortunate as it reduced the reliability of these measurements. Instead, the dynamic test rig should be tuned to yield a higher flutter limit than the prototype bridge, e.g. by readjusting the tuned stiffness to increase the frequency separation of the considered modes. This may be performed due to the non-dimensional properties of the aerodynamic derivatives, and would provide a larger range of reduced velocities in the experimental data.

The mode shape similarity matrix proved a useful tool for evaluating whether multimodal coupling effects should be considered. Both the first and second vertical modes provided high similarities with the fundamental torsional mode, hence these where likely to contribute to multimodal flutter. The similarity

matrix further indicated that the multimodal flutter of the Hålogaland Bridge is restricted to coupling with the fundamental symmetric torsion mode.

The results of the multimodal flutter analysis show that the stability limit of the Hålogaland Bridge may be classified as three-mode flutter. The critical mean wind velocity and critical oscillation frequency were found to 68.1 m/s and 2.03 rad/s, respectively. The critical limit is above the design requirement of 60.2 m/s. The critical reduced velocity is found to 1.80. Multimodal effects have decreased the reduced critical velocity within the range of the experimental data. This validates the obtained results.

It should be concluded that when the eigenfrequencies are closely spaced, as is the case of the Hålogaland Bridge, it is not sufficient to only consider the bi-modal flutter limit. This may severely underestimate the actual stability limit. The results further indicate that the aerodynamic behavior of the cross-section of the Hålogaland Bridge is affected by its slender nature. This is seen by comparing obtained flutter derivatives with corresponding wind tunnel tests of other bridges. The high B/H ratio yields a relatively bluff shape. The aerodynamic derivatives show severe difference from those of a flat plate. As a consequence, Selberg's formula overestimates the flutter limit with 16 %.

Based on the new design requirement of the Norwegian Road Directory, possible horizontal mode contributions to flutter is investigated. As only vertical and torsional motion were simulated in the wind tunnel, the flutter derivatives related to horizontal motions and loads are described based on quasi-static theory and derivatives extracted by the discrete vortex program DVMFLOW. The results indicate that inclusion of horizontal modes does not affect the governing flutter limit. It should however be noted that wind tunnel tests should be provided to verify the results. To the best of the author's knowledge, results where the horizontal modes had a significant effect in development of flutter are limited to the experience with the Akashi-Kaikyo Bridge in Japan. As simulating horizontal flutter derivatives is difficult and expensive, it should be discussed whether the new design requirement should specify further which types of bridge decks that are susceptive to horizontal mode influence.

The three-mode flutter limit of 68.1 m/s is based on complete determinacy of all input parameters, in a deterministic flutter analysis. However, a number of uncertainties are related to the prediction of flutter. Hence, there is a need for establishing a probabilistic flutter analysis, where the sensitivity of the flutter limit with respect to parameter uncertainty is evaluated.

The uncertainty arising due to large scatter in the wind tunnel test series of aerodynamic derivatives is considered. It is investigated how different choice of curve approximation affects the flutter limit. Constraint curves are fitted to the data series of aerodynamic derivatives, and the fitting error, residuals, are included as a parameter uncertainty in the probabilistic flutter analysis.

The uncertainty related to determining the modal structural damping ratios is included in the probabilistic analysis as a parameter uncertainty. Two approaches, Case A and Case B, of modeling the structural damping ratio are suggested. Case A provides a conservative estimate of the damping ratio, with low uncertainty. Case B is less conservative, but subjected to higher uncertainty.

The proposed probabilistic approach involving a Monte Carlo Simulation analysis was found to work well for the purpose of considering effects of parameter uncertainty. By performing a large number of deterministic flutter analyses with random generated input variables, the resulting distribution of the flutter limit is obtained. Uncertainties in input variables were assumed to follow a normal distribution. An adequate number of simulations were conducted, so that statistics could be performed on the output variables. Convergence studies of the results showed that 10 000 simulations provides an accuracy of 1 decimal of the critical mean wind velocity, which is deemed sufficient. The sensitivity of the flutter limit with respect to the considered parameter uncertainty is evaluated in terms of width, mean value, and possible skewness and tail behavior of the output distributions.

The distribution of critical mean wind velocity due to the modeled uncertainty of flutter derivatives is seen to have right skewed shape with distinctive tail behavior. Investigations show that it can be described by a generalized extreme value (GEV) distribution. The mean value of the distribution of V_{cr} is close to the corresponding critical velocity of a deterministic analysis. Hence, the mean value is not sensitive to parameter uncertainty. The fitted GEV distribution provides a 95 % confidence interval ranging from 64.2 m/s to 76.9 m/s. The large width of the confidence interval indicates the accuracy of which the flutter limit may be determined. Hence it may be concluded that the flutter limit is sensitive to the modeled parameter uncertainty of the flutter derivatives.

The scatter in the wind tunnel test of aerodynamic derivatives does to a large extent stem from the observations at the three highest reduced velocities. These are assumed less accurate, as the flutter limit of the section model is reached. A second flutter analysis where the three last observations were excluded is conducted. The results show that this exclusion severely reduced the width of the distribution of critical velocities, by yielding a 95 % confidence interval spanning from 65.5 m/s to 70.0 m/s. A corresponding deterministic analysis excluding these observations resulted in an insignificant difference in critical mean wind velocity. This illustrates the value of the probabilistic analysis. By excluding the three last observations in the data series, the aerodynamic derivatives at the flutter limit are to a large extent based on extrapolated behavior. Hence the validity of the results is questionable.

A disadvantage of the proposed modeling of uncertainties of aerodynamic derivatives is that the model is based on few observation points. A larger data set would increase the reliability of the probabilistic flutter limit. Due to the proposed modeling based on standard error of residuals, the large uncertainty related to the observation in the end of the test series are introduced at all velocities. These uncertainties would have less influence in a larger data set, as the magnitude of the respective residuals would relatively have less importance.

The distribution of critical velocities due to parameter uncertainty of structural damping ratio was found to follow a normal distribution. Both the considered models yielded narrow distributions with insignificant variation of critical velocities. A 95 % confidence interval of Case B ranges critical velocities from 68.2 m/s to 69.4 m/s. From this it is concluded that the sensitivity of the flutter limit of the Hålogaland Bridge to variations in structural damping ratio is low.

Including parameter uncertainty of flutter derivatives and damping ratio pro-

vided a 99 % confidence interval ranging critical velocities from 63.5 m/s to 78.6 m/s. The lower limit of the interval is higher than the design requirement of 60.2 m/s. Hence, a sufficient safety against flutter failure is secured. Still, the output distributions of critical velocity and critical oscillation frequency indicated the accuracy of which the flutter limit could be evaluated. Hence, it is concluded that a probabilistic flutter analysis provides an extended understanding of the nature of the flutter limit, compared to a corresponding deterministic analysis.

Limitations and future work:

The probabilistic analysis is limited to considering the suggested probabilistic modeling of parameter uncertainty of flutter derivatives and structural damping ratio. Whether the other input parameters indeed can be considered deterministic should be investigated. Further, it should be emphasized that there are no evidence that the parameter uncertainty indeed do follow a normal distribution. In addition to scatter in the measurement of aerodynamic derivatives, there are a lot of other uncertainties related to modeling of self-excited forces. The relative importance of the different uncertainties and their effect should be given focus in an extended study.

Bibliography

[1] Benjamin, J. R. and C. A. Cornell (1970). *Probability, statistics, and decision for civil engineers.* New York: McGraw-Hill.

[2] Brownjohn, J. (1994). Estimation of damping in suspension bridges. *Proc. Instn Civ. Engrs Structs & Bldgs 104*, 401–415.

[3] Chen, X. and A. Kareem (2008). Identification of critical structural modes and flutter derivatives for predicting coupled bridge flutter. *Journal of Wind Engineering and Industrial Aerodynamics 96*(10-11), 1856 – 1870.

[4] Cheng, J., C. Cai, R. Xiao, and S. Chen (2005). Flutter reliability analysis of suspension bridges. *Journal of wind engineering and industrial aerodynamics 93*(10), 757–775.

[5] Cheng, J. and R. Xiao (2005). Probabilistic free vibration and flutter analyses of suspension bridges. *Engineering Structures 27*(10), 1509–1518.

[6] Davenport, A. and G. Larose (1989). The structural damping of long span bridges: an interpretation of observations. In *Canada-Japan Workshop on Aerodynamics*, Ottawa.

[7] Dyrbye, C. and S. O. Hansen (1997). *Wind loads on structures.* Chichester: Wiley.

[8] FORCE Technology (2010). Section model tests for the Hålogalandsbrua, Rev 1/2010-09-03. Technical report, Lyngby, Denmark.

[9] Fung, Y. (1969). *An introduction to the theory of aeroelasticity.* New York: Dover Publications.

[10] Ge, Y., H. Xiang, and H. Tanaka (2000). Application of a reliability analysis model to bridge flutter under extreme winds. *Journal of Wind Engineering and Industrial Aerodynamics 86*(2-3), 155–167.

[11] Øiseth, O., A. Rønnquist, and R. Sigbjørnsson (2010). Simplified prediction of wind-induced response and stability limit of slender long-span suspension bridges, based on modified quasi-steady theory: A case study. *Journal of wind engineering and industrial aerodynamics 98*(12), 730–741.

[12] Øiseth, O. and R. Sigbjörnsson (2011). An alternative analytical approach to prediction of flutter stability limits of cable supported bridges. *Journal of Sound and Vibration 330*(12), 2784–2800.

[13] Jakobsen, J. and E. Hjort-Hansen (2007). Arne selberg's formula for flutter speed in light of multimodal flutter analysis. In *ICWE Australia 2007*.

[14] Jakobsen, J. and H. Tanaka (2003). Modeling uncertainties in prediction of wind aeroelastic bridge behaviour. *Journal of Wind Engineering and Industrial Aerodynamics 91*, 1485–1498.

[15] Katsuchi, H., N. P. Jones, and R. H. Scanlan (1999). Multimode coupled flutter and buffeting analysis of the akashi-kaikyo bridge. *Journal of Structural Engineering 125*(1), 60–70.

[16] Kwon, S. (2010). Uncertainty of bridge flutter velocity measured at wind tunnel tests. In *The Fifth International Symposium on Computational Wind Engineering (CWE2010)*.

[17] Larsen, A. (1999). A 1999 view on aeroelastic stability - a driving force in bridge aerodynamics. In A. Larsen, G. Larose, and F. Livesey (Eds.), *Wind engineering into the 21st century: Proceedings of of the 10th International Conference on Wind Engineering*.

[18] Larsen, A. and J. Walther (1997). Two dimensional discrete vortex method for application to bluff body aerodynamics. *Journal of Wind Engineering and Industrial Aerodynamics 67-68*, 183 – 193. Computational Wind Engineering.

[19] Mathworks (2011). Matlab product documentation www.mathworks.com.

[20] Nishijima, K. (2011). Lecture 5 - model verification. 2011 Phd seminar on Probabilsitic Modelling in Civil Engineering. DTU, Department of Civil Engineering, Section of Structural Engineering, BYG.

[21] Ostenfeld-Rosenthal, P., H. Madsen, and A. Larsen (1992). Probabilistic flutter criteria for long span bridges. *Journal of Wind Engineering and Industrial Aerodynamics 42*(1-3), 1265–1276.

[22] Pourzeynali, S. and T. K. Datta (2002). Reliability analysis of suspension bridges against flutter. *Journal of Sound and Vibration 254*(1), 143–162.

[23] Scanlan, R. H. and J. J. Tomko (1971). Airfoil and bridge deck flutter derivatives. *Engineering Mechanics Division ASCE 97*, 1717–1737.

[24] Selberg, A. (1961). *Oscillation and aerodynamic stability of suspension bridges*, Volume no. 13. Helsinki: Finnish Academy of Technical Sciences.

[25] Simiu, E. and T. Miyata (2006). *Design of buildings and bridges for wind: a practical guide for ASCE-7 standard users and designersof special structures*. Hoboken, N.J.: Wiley.

[26] Statens Vegvesen (2009). *Håndbok 185: Bruprosjektering*. Oslo.

[27] Statens Vegvesen (2011). www.vegvesen.no.

[28] Strømmen, E. N. (2010). *Theory of bridge aerodynamics* (2nd ed.). Berlin: Springer.

[29] Sven Ole Hansen ApS (2006). The Hardanger Bridge: Static and dynamic wind tunnel tests with a section model, Rev 1/2006-12. Technical report, Copenhagen, Denmark.

Appendix A

Aerodynamic derivatives

The Hålogaland Bridge

Measured aerodynamic derivatives of the Hålogaland Bridge. Coefficients of the constraint curves fitted to the data applied in the deterministic analysis are given in Table B.1. The sign convention is as given in Section 2.1.3.

Observation	Velocity	Aerodynamic derivatives			
	$(V/B\omega_z)$	H_1^*	H_4^*	A_1^*	A_4^*
1	0.000	0.000	0.000	0.000	0.000
2	0.893	-2.068	-0.690	-0.927	-0.097
3	1.468	-4.217	-0.404	-1.730	-0.210
4	2.102	-6.393	-0.030	-2.811	-0.333
5	2.665	-8.495	-1.707	-3.663	-0.169
6	3.316	-11.663	-1.461	-4.555	-0.330
7	4.080	-13.462	1.255	-6.181	-0.681
8	4.525	-12.508	-6.320	-5.671	0.257
9	4.642	-11.424	-4.781	-5.701	0.286
10	5.018	-6.931	5.348	-7.072	-0.898

Table A.1: Measured ADs related to vertical motion[8]

Observation	Velocity	Aerodynamic derivatives			
(no.)	$(V/B\omega_\theta)$	H_2^*	H_3^*	A_2^*	A_3^*
1	0.000	0.000	0.000	0.000	0.000
2	0.288	0.402	0.335	-0.026	-0.086
3	0.477	0.247	0.853	-0.061	0.226
4	0.698	0.042	2.086	-0.147	0.487
5	0.928	0.489	3.513	-0.287	0.954
6	1.216	0.591	5.848	-0.487	1.731
7	1.568	0.755	10.931	-0.881	3.028
8	1.876	3.357	16.305	-0.968	4.926
9	1.904	3.762	17.017	-1.000	5.101
10	1.955	5.465	18.470	-1.009	5.323

Table A.2: Measured ADs related to torsional motion[8]

The Hardanger Bridge

Measured aerodynamic derivatives from the wind tunnel report, see [29]. Note that the measured aerodynamic derivatives are described in terms of velocities reduced by the natural frequencies n_z and n_θ in Hz. Otherwise, the sign convention is as given in Section 2.1.3. Coefficients of constraint curves fitted to the data are indicated in Table A.5, as provided by Ole Øiseth at NTNU.

Observation	Velocity	Aerodynamic derivatives			
(no.)	(V/Bn_z)	H_1^*	H_4^*	A_1^*	A_4^*
1	8.18	-4.12	-2.22	-0.88	-0.40
2	10.01	-4.21	-4.69	-1.02	-0.77
3	12.04	-6.22	-3.90	-1.39	-0.67
4	13.62	-6.89	-5.92	-1.31	-1.09
5	16.40	-6.68	-1.86	-1.43	-0.46
6	17.42	-12.16	-6.58	-2.33	-1.65
7	19.33	-13.00	-5.24	-2.86	-1.67
8	20.69	-9.46	-9.64	-2.79	-1.01
9	22.29	-9.03	-9.46	-3.64	-0.59

Table A.3: Measured ADs related to vertical motion

Observation	Velocity	Aerodynamic derivatives			
(no.)	(V/Bn_θ)	H_2^*	H_3^*	A_2^*	A_3^*
1	3.36	-0.08	0.70	-0.05	0.07
2	4.23	0.23	0.90	-0.02	0.17
3	5.12	0.07	1.61	-0.04	0.33
4	6.03	-0.11	2.55	-0.17	0.58
5	7.07	0.12	3.12	-0.13	0.74
6	8.23	-0.30	5.25	-0.24	1.29
7	9.16	-0.22	5.84	-0.23	1.48
8	10.59	-0.59	8.06	-0.39	2.09
9	11.57	-1.23	9.40	-0.59	2.39

Table A.4: Measured ADs related torsional motion [8]

$AD_i = p_2\hat{V}^2 + p_1\hat{V} + p_0$								
	H_1^*	H_2^*	H_3^*	H_4^*	A_1^*	A_2^*	A_3^*	A_4^*
p_2	0.12	-0.34	2.37	-0.17	-0.08	-0.14	0.88	0.06
p_1	3.16	0.82	-0.19	-0.13	-0.54	-0.54	-0.29	-0.36
p_0	0.00	0.00	0.00	0.00	0.00	0.00	0.00	0.00

Table A.5: Coefficients of constraint curves for the wind tunnel data of the Hardanger Bridge

The Great Belt Bridge

The measured aerodynamic derivatives of the Great Belt Bridge are provided by COWI. Note that A_4^* was not extracted. Coefficients of constraint curves fitted to the data are indicated in Table A.7. The sign convention is as given in Section 2.1.3.

	Velocity	Aerodynamic derivatives						
(no.)	$(V/B\omega)$	H_1^*	H_2^*	H_3^*	H_4^*	A_1^*	A_2^*	A_3^*
1	0.80	-1.40	0.48	1.86	-0.96	-0.60	-0.10	0.48
2	0.95	-2.00	0.46	2.90	-1.24	-0.72	-0.16	0.74
3	1.11	-2.70	0.32	4.16	-1.50	-0.86	-0.23	1.06
4	1.27	-3.30	0.08	5.56	-1.82	-1.01	-0.30	1.42
5	1.43	-4.10	-0.32	7.20	-2.20	-1.13	-0.38	1.82
6	1.57	-5.00	-0.82	8.90	-2.50	-1.28	-0.46	2.26
7	1.75	-6.10	-1.50	10.74	-2.86	-1.44	-0.56	2.72
8	1.91	-7.10	-2.30	12.66	-3.30	-1.58	-0.66	3.18
9	2.07	-8.10	-3.30	14.74	-3.64	-1.76	-0.75	3.74
10	2.23	-9.20	-4.40	16.96	-4.10	-1.90	-0.85	4.26
11	2.39	-10.30	-5.68	19.36	-4.50	-2.06	-0.96	4.82

Table A.6: Measured ADs of the Great Belt Bridge

$AD_i = p_2\hat{V}^2 + p_1\hat{V} + p_0$								
	H_1^*	H_2^*	H_3^*	H_4^*	A_1^*	A_2^*	A_3^*	A_4^*
p_2	0.00	-2.80	2.70	0.00	0.00	0.00	0.63	0.00
p_1	-5.66	5.07	2.43	-5.66	-0.92	-0.54	0.76	0.00
p_0	3.62	-1.82	-1.85	3.62	0.17	0.37	-0.55	0.00

Table A.7: Coefficients of constraint curves for the wind tunnel data of the Great Belt Bridge

Quasi-static ADs of the Hålogaland Bridge

Static aerodynamic force coefficients for the Hålogaland Bridge refers to a section model subjected to smooth western wind, without traffic. For further details see the wind tunnel report in [8]. The equivalent quasi-static aerodynamic derivatives according to Eq. 2.30 are given in Table A.9. Note that all other derivatives than the horizontal are based on wind tunnel data, as given in Table B.1.

C_D (0°)	C_L (0°)	C_M (0°)	C_D' ($-1°$ to $1°$)	C_L' ($-1°$ to $1°$)	C_M' ($-1°$ to $1°$)
0.126	-0.539	-0.054	-0.17	4.04	1.25

Table A.8: Static aerodynamic force coefficients of the Hålogaland Bridge and their slopes

$AD_i = p_2 \hat{V}^2 + p_1 \hat{V} + p_0$					
	H_5^*	A_5^*	P_1^*	P_3^*	P_5^*
p_2	0.00	0.00	0.00	-0.04	0.00
p_1	1.08	0.11	-0.04	0.00	-0.50
p_0	0.00	0.00	0.00	0.00	0.00

Table A.9: Coefficients of constraint curves of DVMFLOW5.1

DVMFLOW simulations of the Hålogaland Bridge

Aerodynamic derivatives extracted by the discrete vortex code DVMFLOW. All 18 aerodynamic derivatives are extracted. The sign convention is as given in Section 2.1.3. Constraint curves fitted to the data is indicated in Table A.13 to A.15.

Observation (no.)	Velocity $(V/B\omega)$	Aerodynamic derivatives					
		H_1^*	H_4^*	A_1^*	A_4^*	P_5^*	P_6^*
1	0.32	-0.57	1.10	-0.24	0.00	0.03	0.00
2	0.64	-1.24	0.03	-0.47	0.04	0.08	-0.01
3	0.95	-1.34	0.45	-0.79	-0.06	0.11	-0.01
4	1.27	-2.50	0.44	-0.97	-0.21	0.26	0.03
5	1.59	-7.12	1.41	-1.19	-0.33	0.l7	-0.03
6	1.91	-1.91	-1.61	-1.29	0.23	0.23	-0.04
7	2.23	-10.05	-0.31	-1.57	-0.67	0.70	0.18
8	2.55	-5.94	-5.02	-1.68	-0.12	0.20	-0.43
9	2.86	-12.20	-1.90	-2.15	-0.64	0.26	-0.01

Table A.10: ADs elated to vertical motion extracted from forced oscillation simulation in DVMFLOW,

Observation (no.)	Velocity $(V/B\omega)$	Aerodynamic derivatives					
		H_2^*	H_3^*	A_2^*	A_3^*	P_2^*	P_3^*
1	0.32	0.47	-0.03	0.09	0.09	0.00	0.01
2	0.64	0.56	0.02	0.37	0.37	0.04	0.04
3	0.95	3.03	-0.03	0.75	0.75	-0.03	0.04
4	1.27	4.87	-0.12	1.43	1.43	0.00	0.18
5	1.59	7.61	-0.42	2.09	2.09	0.22	0.00
6	1.91	11.94	-0.39	3.07	3.07	0.10	0.49
7	2.23	18.6	-0.48	-1.06	-1.06	0.36	0.12
8	2.55	32.49	-0.20	5.90	5.90	-0.15	0.30
9	2.86	24.72	-1.27	6.95	6.95	0.46	0.48

Table A.11: ADs elated to torsional motion extracted from forced oscillation simulation in DVMFLOW

Observation	Velocity	Aerodynamic derivatives					
(no.)	$(V/B\omega)$	H_5^*	H_6^*	A_5^*	A_6^*	P_1^*	P_4^*
1	0.95	-0.39	-0.01	0.04	-0.03	-0.06	0.05
2	1.27	-0.44	0.51	0.06	-0.05	0.11	0.01
3	1.59	-1.01	-0.37	0.18	0.01	-0.10	0.07
4	1.91	-1.06	-0.53	0.18	-0.11	-0.22	0.11
5	2.23	-0.01	1.87	0.05	-0.06	-0.13	0.04
6	2.55	1.45	-11.88	0.41	0.05	-0.12	0.88
7	2.86	-9.22	-7.94	0.52	-0.83	0.07	0.28

Table A.12: ADs elated to horizontal motion extracted from forced oscillation simulation in DVMFLOW

$AD_i = p_2\hat{V}^2 + p_1\hat{V} + p_0$						
	H_1^*	H_2^*	H_3^*	H_4^*	H_5^*	H_6^*
p_2	0.00	0.00	0.035	0.00	0.00	0.00
p_1	-0.008	0.113	0.053	0.269	0.125	-0.054
p_0	-0.050	-0.067	-0.015	-0.306	0.030	0.051

Table A.13: Coefficients of constraint curves of DVMFLOW5.1

$AD_i = p_2\hat{V}^2 + p_1\hat{V} + p_0$						
	A_1^*	A_2^*	A_3^*	A_4^*	A_5^*	A_6^*
p_2	0.00	0.00	2.703	0.00	0.00	0.00
p_1	-4.054	0.700	1.684	-1.608	0.937	-5.200
p_0	1.691	0.000	-1.037	1.959	-1.884	7.309

Table A.14: Coefficients of constraint curves of DVMFLOW5.1

$AD_i = p_2\hat{V}^2 + p_1\hat{V} + p_0$						
	P_1^*	P_2^*	P_3^*	P_4^*	P_5^*	P_6^*
p_2	0.000	0.000	0.903	0.000	0.000	0.000
p_1	-0.688	-0.355	-0.135	-0.201	0.229	-0.050
p_0	0.056	0.242	0.066	0.123	-0.232	0.000

Table A.15: Coefficients of constraint curves of DVMFLOW5.1

Appendix B

Modeling uncertainties

Different interpretations of aerodynamic derivatives of the Håloga-land Bridge

$AD_i = p_2\hat{V}^2 + p_1\hat{V} + p_0$								
	H_1^*	H_2^*	H_3^*	H_4^*	A_1^*	A_2^*	A_3^*	A_4^*
p_2	0.00	0.00	5.59	0.24	0.00	0.00	1.74	0.01
p_1	-3.20	2.06	-1.83	-1.42	-1.38	-0.59	-0.73	-0.12
p_0	0.20	-0.90	0.28	0.58	0.12	0.16	0.10	-0.03

Table B.1: Coefficients of constraint curves corresponding to Case 1 in Table 5.1, these are also utilized in the deterministic flutter analysis in Chapter 4

$AD_i = p_2\hat{V}^2 + p_1\hat{V} + p_0$								
	H_1^*	H_2^*	H_3^*	H_4^*	A_1^*	A_2^*	A_3^*	A_4^*
p_2	0.69	2.35	5.59	024	0.01	-0.18	1.74	0.01
p_1	-5.87	-2.75	-1.83	-1.42	-1.45	-0.21	-0.73	-0.12
p_0	1.63	0.62	0.28	0.58	0.17	0.04	0.10	-0.03

Table B.2: Coefficients of constraint curves corresponding to Case 2 in Table 5.1

$AD_i = p_2\hat{V}^2 + p_1\hat{V} + p_0$								
	H_1^*	H_2^*	H_3^*	H_4^*	A_1^*	A_2^*	A_3^*	A_4^*
p_2	0.00	0.00	3.96	0.00	0.00	0.00	1.61	0.03
p_1	-3.52	0.39	0.36	-0.44	-1.42	-0.53	-0.58	-0.17
p_0	0.65	0.03	-0.36	0.05	0.18	0.19	0.07	0.01

Table B.3: Coefficients of constraint curves corresponding to Case 3 in Table 5.1

$AD_i = p_2\hat{V}^2 + p_1\hat{V} + p_0$								
	H_1^*	H_2^*	H_3^*	H_4^*	A_1^*	A_2^*	A_3^*	A_4^*
p_2	0.00	0.00	7.02	0.00	0.00	0.00	1.88	0.00
p_1	-3.68	5.95	-5.51	0.35	-1.66	-0.68	-0.93	-0.15
p_0	1.18	-7.34	2.19	-1.43	0.74	0.28	-0.93	0.07

Table B.4: Coefficients of constraint curves corresponding to Case 4 in Table 5.1

Residuals of Case 2

Observation	Residuals							
(no.)	H_1^*	H_2^*	H_3^*	H_4^*	A_1^*	A_2^*	A_3^*	A_4^*
1	-1.63	-0.62	-0.28	-0.58	-0.17	-0.04	-0.10	0.03
2	1.00	0.38	0.12	-0.19	0.18	0.01	0.05	0.03
3	1.29	0.40	0.17	0.59	0.19	0.04	0.08	-0.04
4	1.28	0.20	0.36	1.32	0.00	0.05	0.05	-0.12
5	0.65	0.40	0.11	-0.20	-0.08	0.02	0.03	0.08
6	-1.38	-0.16	-0.48	0.04	-0.08	-0.01	-0.05	-0.06
7	-2.57	-1.33	-0.23	2.48	-0.68	-0.15	-0.21	-0.40
8	-1.64	-0.37	-0.21	-5.38	0.42	0.02	0.07	0.54
9	-0.60	-0.14	0.04	-3.93	0.55	0.01	0.08	0.56
10	3.60	1.24	0.41	5.86	-0.33	0.05	0.00	-0.63

Table B.5: Residuals from curve approximation Case 2

$P(i,j)$	H_1^*	H_2^*	H_3^*	H_4^*	A_1^*	A_2^*	A_3^*	A_4^*
H_1^*	1.00	0.00	0.00	0.10	0.89	0.02	0.12	0.24
H_2^*	0.00	1.00	0.01	0.29	0.54	0.00	0.04	0.52
H_3^*	0.00	0.01	1.00	0.22	0.79	0.07	0.11	0.43
H_4^*	0.10	0.29	0.22	1.00	0.01	0.82	0.25	0.00
A_1^*	0.89	0.54	0.79	0.01	1.00	0.06	0.00	0.00
A_2^*	0.02	0.00	0.07	0.82	0.06	1.00	0.00	0.55
A_3^*	0.12	0.04	0.11	0.25	0.00	0.00	1.00	0.12
A_4^*	0.24	0.52	0.43	0.00	0.00	0.55	0.12	1.00

Table B.6: Matrix of p-values, where values lower than 0.05 indicate dependence

Residuals of Case 3

Observation	Residuals							
(no.)	H_1^*	H_2^*	H_3^*	H_4^*	A_1^*	A_2^*	A_3^*	A_4^*
1	-0.65	-0.22	-0.71	-0.05	-0.18	0.06	-0.16	-0.01
2	0.43	0.26	0.27	-0.35	0.15	-0.07	0.05	0.03
3	0.29	0.03	0.14	0.19	0.16	0.00	0.06	-0.02
4	0.35	-0.26	0.27	0.84	-0.02	0.03	0.04	-0.08
5	0.23	0.10	0.13	-0.59	-0.07	0.01	0.03	0.11
6	-0.65	0.09	-0.09	-0.06	-0.04	-0.03	-0.02	-0.04

Table B.7: Residuals from curve approximation Case 3

$COV(i,j)$	H_1^*	H_2^*	H_3^*	H_4^*	A_1^*	A_2^*	A_3^*	A_4^*
H_1^*	0.26	0.03	0.16	0.03	0.05	-0.01	0.04	0.01
H_2^*	0.03	0.04	0.03	-0.07	0.02	-0.01	0.01	0.01
H_3^*	0.16	0.03	0.14	0.03	0.04	-0.01	0.03	0.00
H_4^*	0.03	-0.07	0.03	0.24	0.00	0.01	0.00	-0.03
A_1^*	0.05	0.02	0.04	0.00	0.02	0.00	0.00	0.00
A_2^*	-0.01	-0.01	-0.01	0.01	0.00	0.00	0.00	0.00
A_3^*	0.04	0.03	0.03	0.00	0.01	0.00	0.01	0.00
A_4^*	0.01	0.00	0.00	-0.03	0.00	0.00	0.00	0.00

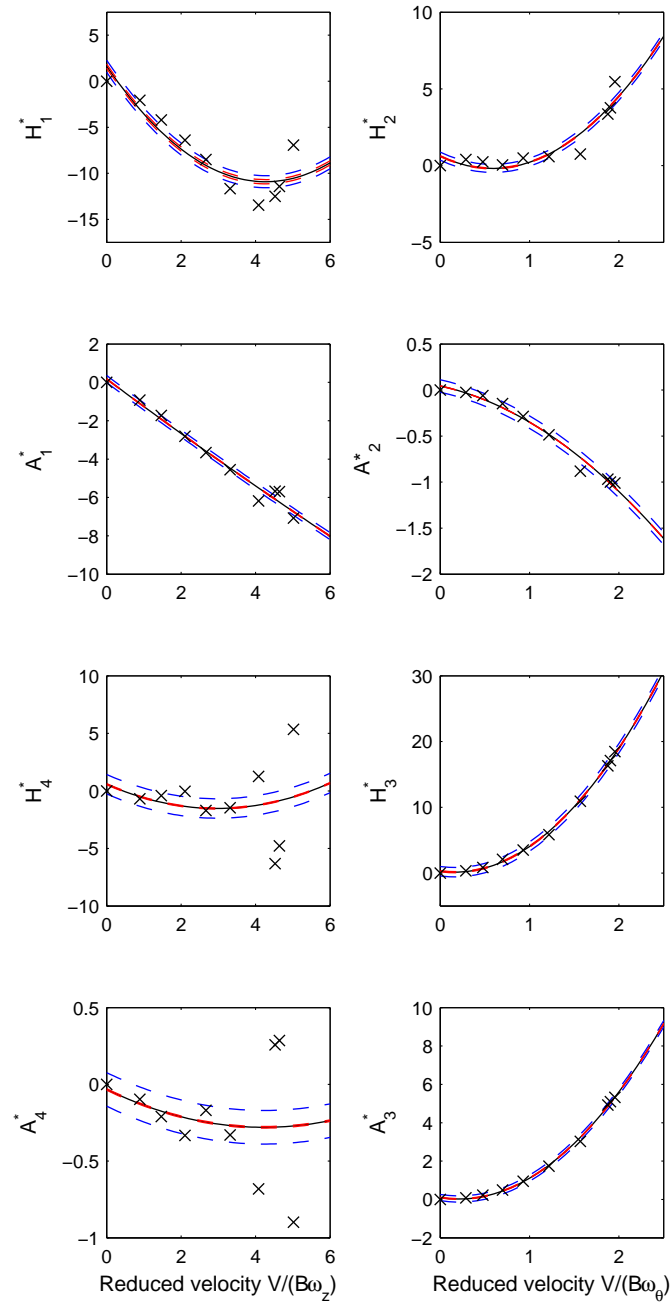Table B.8: Covariance matrix of residuals of Case 3 approximation curve

Figure B.1: Residual plot of case 3 ADs

Appendix C

Results of probabilistic flutter analysis

Flutter limit sensitivity to uncertainties of flutter derivatives

Probabilistic variable	Critical mean velocity V_{cr}			
	mean value (m/s)	standard dev. (m/s)	max. value (m/s)	min. value (m/s)
All derivatives	69.3	3.3	88.0	59.8
H_1^* only	68.8	0.8	73.1	66.6
H_2^* only	68.8	0.3	69.9	67.4
H_3^* only	68.7	0.4	69.9	67.2
H_4^* only	68.7	1.3	73.3	62.9
A_1^* only	68.7	2.4	77.1	59.2
A_2^* only	68.7	1.1	72.0	62.0
A_3^* only	68.8	0.4	70.2	67.2
A_4^* only	68.9	1.9	77.2	62.7

Table C.1: Critical mean wind velocity from probabilistic analysis with aerodynamic derivatives as probabilistic variables

Probabilistic variable	Critical mean velocity ω_{cr}			
	mean value (rad/s)	standard dev. (rad/s)	max. value (rad/s)	min. value (rad/s)
All derivatives	2.020	0.056	2.195	1.774
H_1^* only	2.024	0.012	2.042	1.954
H_2^* only	2.026	0.001	2.031	2.021
H_3^* only	2.026	0.010	2.068	1.994
H_4^* only	2.027	0.0436	2.202	1.857
A_1^* only	2.025	0.075	2.279	1.727
A_2^* only	2.028	0.0292	2.195	1.943
A_3^* only	2.026	0.008	2.055	1.997
A_4^* only	2.025	0.019	2.086	1.944

Table C.2: Critical oscillation frequency from probabilistic analysis with aerodynamic derivatives as probabilistic variables

Probabilistic variable	Critical mean velocity V_{cr}			
	mean value (m/s)	standard dev. (m/s)	max. value (m/s)	min. value (m/s)
All original	69.3	3.3	88.0	59.8
All (Case 3)	67.7	1.1	71.5	60.7
All but H_4^*,A_4^*	68.7	2.4	77.3	58.1
All (COV = 0)	68.7	3.9	86.2	47.9

Table C.3: Critical mean wind velocity from probabilistic analysis with aerodynamic derivatives as probabilistic variables

Flutter limit sensitivity to uncertainties of structural damping

Probabilistic Variable (Damping)	Critical mean velocity V_{cr}			
	mean value (m/s)	standard dev. (m/s)	max. value (m/s)	min. value (m/s)
Case A	68.2	0.2	69.0	67.4
Case B	68.8	0.2	69.8	69.6

Table C.4: Results from flutter analysis with damping as a probabilistic variable

Probabilistic variable (Damping)	Critical oscillation frequency ω_{cr}			
	mean value (rad/s)	standard dev. (rad/s)	max. value (rad/s)	min. value (rad/s)
Case A	2.040	0.005	2.060.	2.021
Case B	2.061	0.007	2.054	2.002

Table C.5: Results from flutter analysis with damping as a probabilistic variable